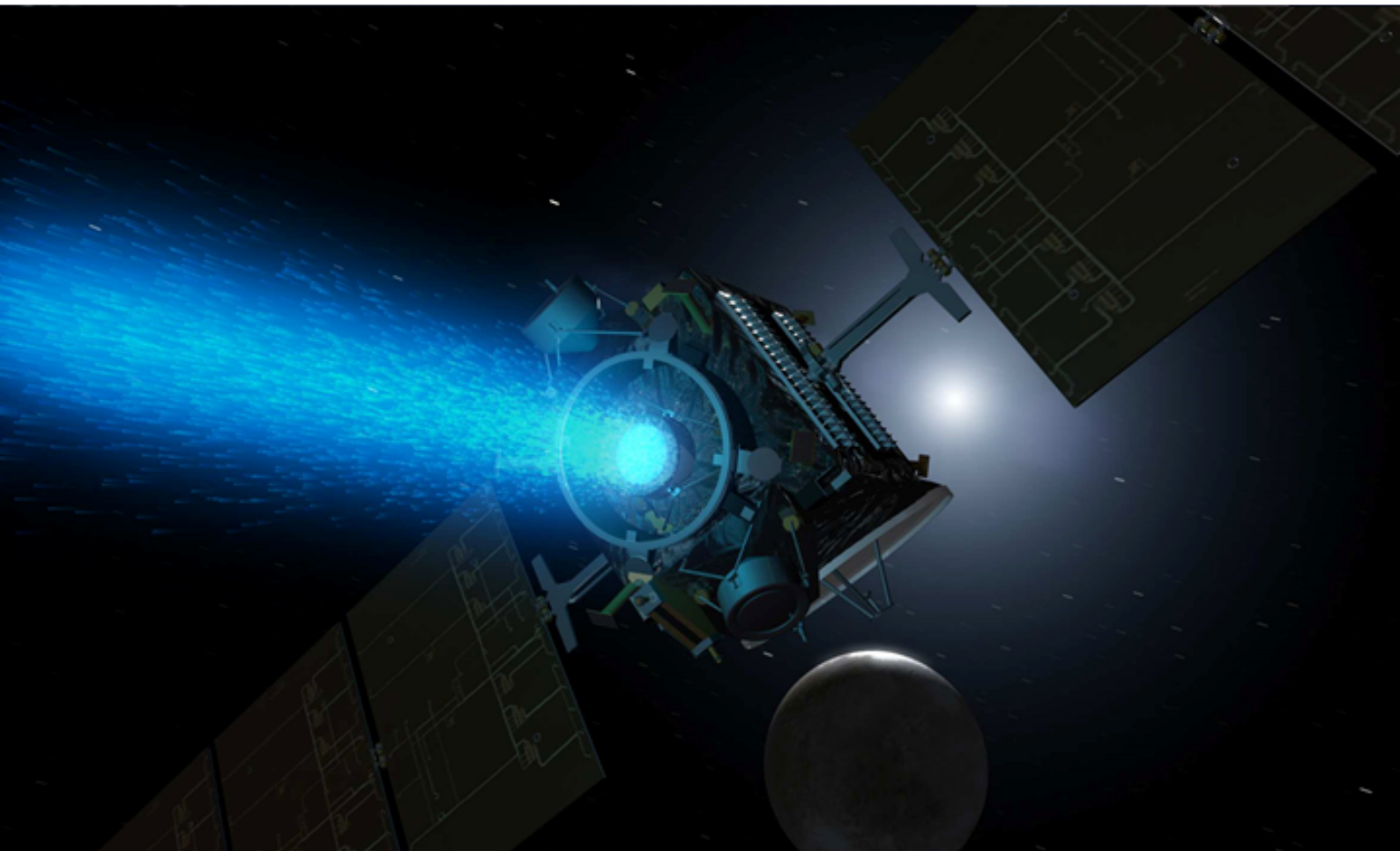# Hybrid Optimization of Low-Thrust Many-Revolution Trajectories with Coasting Arcs and Longitude Targeting for Propellant Minimization

Master of Science Thesis

July 13th, 2017

David Jimenez-Lluva

TU Delft

Delft
University of
Technology

Challenge the future

Hybrid Optimization of Low-Thrust Many-Revolution Trajectories with Coasting Arcs and Longitude Targeting for Propellant Minimization

MASTER OF SCIENCE THESIS
JULY 13TH, 2017

by

David Jimenez-Lluva

Faculty of Aerospace Engineering,
Delft University of Technology

Author:	D. Jimenez-Lluva	
Supervisors:	Ir. B.C. (Bart) Root	TU Delft
	Ir. A. (Antonio) Lozano	GMV
Thesis committee:	Prof. Dr. Ir. P.N.A.M. (Pieter) Visser	TU Delft
	Ir. K. (Kevin) Cowan	TU Delft
	Ir. B.C. (Bart) Root	TU Delft
	Ir. A. (Antonio) Lozano	GMV

PREFACE

This report finalizes the 42 ECTS thesis project that culminates the Master of Science (MSc) in Aerospace Engineering at Delft University of Technology (TU Delft). It was preceded by a detailed literature study aimed at identifying rooms for improvement in state-of-the-art techniques within the field of low-thrust many-revolution trajectory optimization. Some of the most relevant findings of this literature study are briefly mentioned again in this report. Readers of this thesis are expected to have a basic understanding of mathematics, astrodynamics, and optimal control theory. Thus, readers who seek a fundamental insight to these topics and readers who may be interested in further continuing this research are encouraged to request the literature study report from the author or one of the supervisors.

This MSc thesis project entails a cooperation between the author, TU Delft and GMV Innovating Solutions (GMV). As a technology business group with a strong leadership in space engineering, GMV has a profound interest in the continuous innovation of their software products and that is the nature of this thesis project. GMV sprouted in 1984 as a start-up led by the dean of the aerospace engineering faculty of the Madrid Polytechnical University (UPM). Its name originally stood for "Flight Mechanics Group" (in Spanish "Grupo Mecánica de Vuelo") and, as it may suggest, GMV's original activities revolved around satellite flight mechanics, mission analysis, as well as satellite navigation and simulation. In its early stages, GMV earned several contracts in international tenders held by the European Space Agency (ESA). In 1988, GMV received the ESA award for Excellence in Orbital Mechanics, which contributed to the international reputation for its high quality specialized services.

Nowadays, GMV Innovating Solutions has become a technology business group that maintains a strong leadership in space engineering and has diversified into eight additional markets. GMV partly attributes this competitive success to its personnel policy, and proactively aims to attract some of the most promising and passionate MSc students through its involvement in university teaching as well as internships and thesis research projects such as the project at hand. This has proven to be a unique opportunity that the author highly recommends to other students interested in these fields.

ACKNOWLEDGMENTS

This thesis project brings an end to my journey as a student at TU Delft. There have been many challenges and struggles along the way yet even more rewarding and fulfilling moments. This thrilling Odyssey has taught me many life lessons and was certainly possible only thanks to the help of several people.

First of all, I would like to thank Antonio Lozano and Javier Cuesta for giving me the chance to develop this MSc thesis at GMV's Flight Dynamics and Operations division in Madrid. GMV's efforts to involve students in real projects through sponsored internships and thesis projects has been an invaluable learning and inspiring experience that I would recommend to any fellow student. I am very grateful for the absolute flexibility they granted me throughout this project and for the inspiring supervision and support from Antonio. Furthermore, I would like to thank Pedro Julio Montealegre for his guidance and help with understanding the work carried out by my predecessors at GMV.

The sophisticated nature of this MSc thesis is the fruit of the high degree of organization and teaching quality of the department of Astrodynamics and Space Missions at TU Delft. Above all, I would like to thank Bart Root for his support and guidance throughout this thesis. He always knew the right questions to ask, taught me many effective research habits, and more importantly, persuaded me to perform my best. Moreover, I would like to thank our MSc coordinator, Ron Noomen, for sharing his passion for mission design with all of us, for his inspiring words, and for his career advice.

The help of Marco Gomez, who studied the hybrid methodology before me, also proved to be an essential catalyzer to the novel developments hereby presented. I am fondly grateful for his availability despite the eight-hour difference, for his constructive feedback on my early ideas, and his up-lifting moral support throughout the project.

Last but certainly not the least, I would like to thank my fellow students. Lukas, a brother from another mother who taught me the real meaning of punctuality. Constantin, who kept up my spirit during the endless study night-shifts throughout the bachelor. Chiwei, a board-mate and brother whom I could always reach out to in difficult times. My BSc thesis group, who restored my faith in teamwork and are 99% responsible for my insanity. Jordy, Ricardo, Agnes, Marius, Arwin, Felix, Manu, Oriol, Bastian, Chris, Corne, and countless other teammates and colleagues that have made this journey absolutely enjoyable.

To my parents who sparked the curiosity that has made of me an engineer; to my sister who was always there for me; and to Terrie, whose support was the catalyzer I needed to finish this thesis in time,

David Jiménez-Lluva

ABSTRACT

Electric Propulsion (EP) has become one of the most efficient technologies for spacecraft propulsion. In contrast to conventional chemical propulsion, the low thrust force generated by EP thrusters can deliver a momentum transfer to the spacecraft that is up to twenty times greater, for an equivalent propellant expenditure. Despite decades of heritage, the topic of low-thrust spacecraft trajectory optimization remains an active field of research, with many approaches available yet much room for improvement. This MSc thesis presents the development of a novel methodology for low-thrust many-revolution trajectory optimization. It employs the state-of-the-art hybrid technique to harness the strengths of both indirect and direct optimization methods. Its indirect nature efficiently reduces the number of optimization variables and its direct counterpart provides an unmatchable flexibility in terms of a configurable force and perturbation model as well as operational constraints handling. This methodology was already shown in literature to be highly reliable for minimum-time trajectories. The research hereby presented maintains these results while enabling it to optimize minimum-propellant trajectories through a mechanism that allows for coasting (non-thrusting) arcs. This approach is additionally combined with an orbital averaging scheme to reduce the propagation load at the expense of accuracy for the rapidly changing variables. Nonetheless, it retains the continuous integration scheme to enable final geodetic longitude targeting in combination with propellant-minimization, which the former hybrid methodologies were incapable of solving for. The trajectory simulator is coupled with an enhanced objective function that reduces the user fine-tuning effort, and with a differential evolution algorithm that leads to a flexible global optimization process with a practical computational effort.

This research is the outcome of the cooperation between the author, Delft University of Technology, and GMV Innovating Solutions, a technology business group with a strong leadership in space engineering. The specific interest of application of this research lies in many-revolution planetocentric trajectories, such as an orbital transfer to Geostationary Earth Orbit, where there are growing market opportunities for all-electric satellite platforms. The resulting software, integrated as part of GMV's Flight Dynamics solution, allows the user to include orbital perturbations and perform a multi-objective optimization with respect to time-of-flight, propellant expenditure, and final geodetic longitude. This research constitutes a quantum leap for the hybrid optimization method because it shows that its accuracy in propellant-minimization is comparable to the analytical global optima despite the simplified co-state dynamics. Furthermore, it is a significant advancement for space mission design and satellite operations because it demonstrates the superior convergence performance of the hybrid methodology relative to GMV's implementation of the indirect approach, particularly in complex problems that combine multiple optimization objectives with varied orbital perturbations and operational constraints fulfillment.

Contents

NOMENCLATURE

NOTATION

$\boldsymbol{x}$	Vector
$\|\boldsymbol{x}\|$	Magnitude of a vector
$\hat{\boldsymbol{x}}$	Unit vector
$\boldsymbol{A}$	Matrix
$\dot{x}$	Derivative of variable x with respect to time
$\overline{x}$	Average value of variable x
$\dot{\overline{x}}$	Averaged value of the derivative of variable x with respect to time
$\frac{d}{dt}$	Derivative of a variable with respect to time
$\odot$	Out-of-plane direction, indicates that a vector points outwards from the page

LATIN SYMBOLS

C_F	Scaling factor in the DE optimization process	-
C_R	Cross-over factor in the DE optimization process	-
D	Number of optimization parameters in the DE optimization process	-
E	Eccentric anomaly	rad
F	Objective function to be minimized in an optimal control problem	-
$\mathcal{H}$	Hamiltonian of the optimal control problem	-
I_{sp}	Specific impulse of the spacecraft engine	s
$\boldsymbol{a}_{J_2}$	Acceleration vector due to the J$_2$-perturbation	km·s^{-2}
J_2	Constant corresponding to the Earth J$_2$ perturbation	-
L	Modified equinoctial element L	rad
$\mathcal{L}$	Lagrange term in the Hamiltonian of an optimal control problem	-
N_P	Population size in the DE optimization process	-
N_{arcs}	Number of co-state arcs within the entire trajectory	-
OA_{step}	Propagation step in the orbital averaging process	days
P_{in}	Input power to the spacecraft engine	W
$\boldsymbol{Q}$	Matrix containing the unit vectors that define the RSW reference frame	-
R_E	Radius of Earth	km
S_t	Switching function in the bang-bang optimization problem	-
T	Thrust force of the spacecraft engine	mN
T_{orb}	Orbital period	s
ΔV	Velocity increment	km·s^{-1}
$\boldsymbol{W}$	Weight vector of the terms in the aggregate objective function	-

W_m	Weight of the propellant expenditure in the aggregate objective function	-
W_q	Weight of the qth state element in the aggregate objective function	-
W_r	Weight of the experienced radiation fluence in the aggregate objective function	-
W_t	Weight of the time-of-flight in the aggregate objective function	-
a	Semi-major axis	km
$\boldsymbol{a}_d$	Total disturbing acceleration vector	km·s^{-2}
$\boldsymbol{æ}$	Vector containing the first five Keplerian elements and the geodetic longitude	-
a_r	Component of the total disturbing acceleration along $\hat{\boldsymbol{q}}_r$	km·s^{-2}
a_s	Component of the total disturbing acceleration along $\hat{\boldsymbol{q}}_\gamma$	km·s^{-2}
$\boldsymbol{a}_T$	Acceleration vector due to the thrust force	km·s^{-2}
a_w	Component of the total disturbing acceleration along $\hat{\boldsymbol{q}}_h$	km·s^{-2}
$\boldsymbol{b}$	Vector containing the auxiliary offset factors in the scaling procedure	-
$\boldsymbol{d}$	Vector containing the auxiliary scaling factors in the scaling procedure	-
e	Eccentricity	-
f	Modified equinoctial element f	-
g_0	Earth's gravitational acceleration at sea level	km·s^{-2}
g	Modified equinoctial element g	-
h	Specific angular momentum	kg·km^2·s^{-1}
i	Inclination	rad
j	Modified equinoctial element j	-
k	Modified equinoctial element k	-
m	Instantaneous total mass of the spacecraft	kg
m_{prop}	Propellant mass consumed by the spacecraft throughout a trajectory	kg
n	Mean motion of the spacecraft	rev·s^{-1}
n_k	Number of integration steps per revolution	-
n_s	Number of co-state discretization nodes within the entire trajectory	-
$\boldsymbol{œ}$	Vector containing the classical Keplerian elements	-
p	Modified equinoctial element p, equivalent to the semi-latus rectum	km
$\hat{\boldsymbol{q}}_\gamma$	Unit vector defining the s-direction in RSW reference frame	-
$\hat{\boldsymbol{q}}_h$	Unit vector defining the w-direction in RSW reference frame	-
$\hat{\boldsymbol{q}}_r$	Unit vector defining the r-direction in RSW reference frame	-
r	Distance between the spacecraft and the central body	km
$\boldsymbol{r}$	Position vector	km
s	Auxiliary variable in the optimal control law derivation	-
t	Time	s
t_f	Transfer time	days
$\boldsymbol{u}$	Control vector containing the control parameters	-
$\boldsymbol{v}$	Velocity vector	km·s^{-1}
v_x	Component of the velocity vector in the x-direction of the ECG frame	km·s^{-1}

v_y	Component of the velocity vector in the y-direction of the ECG frame	km·s^{-1}
v_z	Component of the velocity vector in the z-direction of the ECG frame	km·s^{-1}
w	Auxiliary variable in the optimal control law derivation	-
x	Component of the position vector in the x-direction of the ECG frame	km
$\boldsymbol{x}$	State vector containing the modified equinoctial elements and the total mass	-
$\Delta\boldsymbol{x}$	Integral of the state vector approximated through numerical integration	
y	Component of the position vector in the y-direction of the ECG frame	km
$\boldsymbol{y}$	Design vector containing the optimization parameters	-
z	Component of the position vector in the z-direction of the ECG frame	km

GREEK SYMBOLS

α	Thrust in-plane (yaw) steering angle, measured w.r.t. $\hat{\boldsymbol{q}}_\gamma$	rad
β	Thrust out-plane (pitch) steering angle, measured w.r.t. the orbital plane	rad
γ	Flight-path angle	rad
$\boldsymbol{\epsilon}$	Vector containing the error between $\boldsymbol{x}^{target}$ and $\boldsymbol{x}^{final}$	-
η	Thruster efficiency	-
θ	True anomaly	rad
$\boldsymbol{\lambda}$	Co-state vector in the Hamiltonian of an optimal control problem	-
μ	Earth's gravitational parameter	km^3·s^{-2}
ϕ	Eclipse half-angle	rad
ω	Argument of pericenter	rad
Λ_q^α	Constant related to the qth element in the Hamiltonian derivative w.r.t. α	-
Λ_q^β	Constant related to the qth element in the Hamiltonian derivative w.r.t. β	-
Λ	Geodetic longitude	rad
Φ	Mayer term in the Hamiltonian of an optimal control problem	-
Φ'	Geodetic latitude	rad
Ψ	Radiation fluence	proton/cm^2
Ω	Right ascension of the ascending node	rad

SUBSCRIPTS & SUPERSCRIPTS

$\square^*$	Optimal value of a variable according to Pontryagin's minimum principle
$\square^T$	Transpose of a matrix or vector
$\square_0$	Initial value of a parameter
$\square_{lb}$	Lower bound(s) of variable or vector in the optimization process
$\square_{max}$	Maximum achievable value of a parameter
$\square_{ub}$	Upper bound(s) of variable or vector in the optimization process
$\square_f$	Final achieved value of a parameter at the terminal boundary condition
$\square_{sc}$	Scaled variable or vector
$\square_{simp}$	Integral of a variable approximated through Simpson's scheme

$\Box_t$ Desired target value of a parameter at the terminal boundary condition

$\Box_{trap}$ Integral of a variable approximated through the trapezoidal scheme

ACRONYMS

AOF	Aggregate Objective Function
BC	Boundary Condition
CI	Continuous Integration
DE	Differential Evolution algorithm
DV	Design Vector (contains the optimization parameters)
ECI	Earth-Centered Inertial reference frame
ECEF	Earth-Centered Earth-Fixed reference frame
EP	Electric Propulsion
EOM	Equations of Motion
EPTOS	Electric Propulsion Trajectory Optimization Software
EVENTS	GMV FDO's Events Analysis Tool Available within *focusleop* ®
ESA	European Space Agency
FDO	Flight Dynamics and Operations (division of GMV Space)
GA	Genetic Algorithm
focusleop ®	GMV's toolbox for Launch and Early Operations Phase
focussuite ®	GMV's Flight Dynamics and Operations software solution
GEO	Geostationary Earth Orbit
GMI	Generalized Island Model
GMV	GMV Innovating Solutions
GSG	Galileo Second Generation
GTO	Geostationary Transfer Orbit
GUI	Graphical User Interface
HOSTEP	Hybrid Optimization Software for Trajectories with Electric Propulsion
IGEOR	Initial Guess for Electric Orbit Raising
KKT	Karush-Kuhn-Tucher (optimality condition)
LC	Legendre-Clebsch (optimality condition)
LEO	Low Earth Orbit
LEOP	Launch and Early Operations Phase
MEE	Modified Equinoctial Elements
MEO	Medium-Earth-Orbit
MOO	Multiple Objective Optimization
MSc	Master of Science
NASA	National Aeronautics and Space Administration
NLP	Non-Linear Programming
OA	Orbital Averaging

OCP	Optimal Control Problem
PROPAG	GMV FDO's Propagation Tool Available within *focusleop* ®
PaGMO	Parallel Global Multi-Objective Optimizer
RAAN	Right Ascension of the Ascending Node
RK4	Runge-Kutta 4 fixed-step integration scheme
RK4(5)	Runge-Kutta 4(5) variable-step integration scheme
RKF7(8)	Runge-Kutta-Fehlberg 7(8) variable-step integration scheme
SB	Shape-Based optimization approach
RSW	Radial-Transverse-Normal reference frame
SEP	Solar Electric Propulsion
SEPSPOT	Solar Electric Propulsion Trajectory Optimization Program
SMART	Specific, Measurable, Achievable, Relevant, and Time-bound
SSTO	Super-Synchronous-Transfer-Orbit
SV	State Vector (contains the orbital elements and spacecraft mass)
TFC	Thrust Fourier Coefficients
TOF	Time-of-Flight
TPBVP	Two Point Boundary Value Problem
TU Delft	Delft University of Technology
UPM	Technical University of Madrid (Universidad Politecnica de Madrid)
V&V	Verification and Validation

1

INTRODUCTION

"Impossible today will be possible tomorrow." – Konstantin Tsiolkovski.

Electric Propulsion (EP) is among the most efficient technologies for spacecraft propulsion. It can reach a momentum transfer to the spacecraft that is up to twenty times greater than that of classical chemical propulsion, per kilogram of propellant [Sabbadini et al., 2002]. As compared to the high-thrust manoeuvres of conventional chemical engines, the low-thrust force generated by EP thrusters can be applied continuously and, over time, it can equally accelerate a spacecraft using considerably less propellant mass. Thanks to the technological advancements in the recent decades, EP has become a means for station keeping in Geostationary Earth Orbit (GEO) [Byers and Dankanich, 2008], altitude maintenance (such as the GOCE mission [Drinkwater et al., 2006]), and even interplanetary flight (such as Deep Space-1 [Rayman et al., 1999], SMART-1 [Koppel and Estublier, 2003], Hayabusa [Nishiyama and Kuninaka, 2012], and DAWN [NASA, 2015]). Therefore, private space entities are investing in similar concepts, and some companies such as Boeing have already developed fully electric platforms to deliver payloads from Geostationary Transfer Orbit (GTO) to GEO [Feuerborn et al., 2013].

The classical trade-off in mission planning is whether to aim for the fastest trajectory, and possibly increase the revenues that result from earlier operations, or to aim for the most propellant-efficient trajectory. Naturally, there have long existed many simulation and trajectory optimization tools for this purpose. However, this new era of fully electric satellites raises a need for new methodologies. In contrast to high-thrust chemical manoeuvres which can be modelled as impulsive, electric engines operate continuously and deliver low-thrust forces. Consequently, the equations of motion are different and, more importantly, there is a vast amount of optimization variables because the thrust vector can be adjusted at every second of a typically 200 day trajectory [Geffroy and Epenoy, 1997]. Since the profits to be gained with EP are significant (namely a lower launch mass, a higher payload capability or an extended lifetime), this raises the need for new generations of accurate and robust methodologies to simulate and optimize low-thrust electric propulsion trajectories.

1.1. LOW-THRUST TRAJECTORY OPTIMIZATION HERITAGE

With the development of EP technology over the recent decades, the field of low-thrust trajectory optimization has gained a lot of interest. In interplanetary applications, the use of Shape-Based (SB) approaches is predominant [Taheri and Abdelkhalik, 2016; Hoving, 2015; Roegiers, 2014; Gondelach and Noomen, 2015; Gil-Fernandez and Gomez-Tierno, 2010]. However, these usually perform worse in many-revolution trajectories [Wei and Changhou, 2011], i.e. those that exceed ten revolutions, which is the focus of this thesis.

In addition to SB approaches, there have been many other strategies developed to yield optimal and near optimal trajectories. These can generally be classified into direct methods, such as [Betts, 1994; Taheri and Abdelkhalik, 2016], or indirect methods, such as [Geffroy and Epenoy, 1997; Sanchez and Campa, 2014]. Indirect approaches employ calculus of variations to analytically derive the optimality conditions of the Optimal Control Problem (OCP), and thus solve the Two-Point-Boundary-Value-Problem (TPBVP) in an analytical way. From the optimization objective function and the known system Equations of Motion (EOM), one may set up the Hamiltonian. The first and second derivative of the Hamiltonian with respect to all control parameters allow to find the optimal control settings, whereas the derivatives with respect to the state variables yield the corresponding system co-state EOM. Readers who are not familiar with optimal control theory may find a use-

ful insight in well established sources such as [L. S. Pontryagin et al, 1964]. On the other hand, direct approaches transcribe the OCP to a parameter optimization problem that can be solved through Non-Linear Programming (NLP) by iteratively calculating sets of control parameters that satisfy the EOM and Boundary Conditions (BC), while minimizing the objective function.

Whether direct or indirect methods are better suited for low-thrust optimization problems is debatable. Thanks to the analytical formulation, indirect methods converge to global or near-global optima, whereas direct methods only converge to local optima [Geffroy and Epenoy, 1997]. Conversely, indirect methods are problem specific and a minor change in the formulation, such as incorporating an orbital perturbation or an operational constrain, requires deriving the entire TPBVP again [Geffroy and Epenoy, 1997]. This analytical TPBVP derivation not is a labour intensive task that requires a profound understanding, but also leads to assumptions that may be too significant for certain applications [Boudestijn, 2014]. On the other hand, direct methods offer an unmatchable flexibility in this respect as the inclusion of perturbations simply requires adding extra terms to the EOM, and the addition of operational constraints can be achieved through logical statements in the algorithm. Nonetheless, direct methods often yield inaccurate co-states or no co-state information at all [Benson et al., 2006]. Lastly, indirect methods are known to have a more limited radius of convergence that direct methods [Betts, 1998], and varied combinations of optimization objectives, perturbations and constraints may not be feasible in indirect methods due to the analytical formulation complexity. To this day, there are yet frequent advances and new techniques being developed [Taheri and Abdelkhalik, 2016], and there is still much room for improvement in this field of research due to the problem complexity.

Within GMV, the Flight Dynamics and Operations division (FDO) is currently in the later development stages of a commercial software toolbox to optimize low-thrust planetocentric trajectories, such as an orbital transfer to GEO, where there are growing market opportunities for all-electric satellites. Two core elements of this toolbox are a high-fidelity optimizer known as Electric Propulsion Trajectory Optimization Software (EPTOS) and an a priori optimizer labelled Initial Guess for Electric Orbit Raising (IGEOR). IGEOR employs an indirect optimization method [Montealegre-Avila, 2015] based on the work presented in [Geffroy and Epenoy, 1997; Sanchez and Campa, 2014]. It consists of a single shooting method where the optimization variables are the initial values of the system co-states, which are optimized using a differential evolution algorithm. A detailed insight about single shooting and further discretization schemes can be found in [Jimenez-Lluva, 2016]. The underlying mathematical formulation in IGEOR allows for coasting (non-thrusting) arcs and its indirect nature guarantees a globally optimal solution. However, the inherent limited convergence of the indirect method only allows for incorporating Earth-shadow regions and second-order Earth oblateness effects. Nonetheless, although it cannot incorporate operational constraints or further orbital perturbations, it serves as a near optimal a priori solution that can be accurately refined by EPTOS. EPTOS consists of a parallel shooting method that divides the entire trajectory into segments, each of which is solved through an indirect shooting approach similar to IGEOR [Corneliu et al., 2015]. Continuity constraints are implemented at the boundaries between the trajectory segments and the resulting problem is solved in a direct approach using an NLP optimizer suitable for very large and non-linear problems. This direct nature allows for a full near-Earth orbital perturbations model and is very successful in refining a near optimal trajectory. Conversely, it has the drawback that the solution may only be a global optimum if the initial guess is sufficiently close to it.

1.2. THE ROLE OF THE A PRIORI SOLUTION IN OPTIMIZATION

Complex optimization problems often exhibit large objective function fluctuations and it is important to distinguish between local and global optima, as illustrated in Figure 1.1. The former are points which are the most extreme within a limited domain of the design space, whereas the later are points that constitute the minimum or maximum value over the entire design space. Some algorithms, such as the gradient descent algorithm shown in Figure 1.2, are only capable of local optimization and therefore, require an a priori solution to initialize the search within the optimization process. Hence, the choice of the optimization algorithm is very important for both indirect and direct formulations as it determines is an initial guess is required and whether the resulting optimum is local or near global.

The sensitivity of an optimization algorithm to the a priori solution is referred to as robustness [Kluever, 2010]. The literature study preceding this thesis identified that metaheuristic optimization algorithms are most robust [Jimenez-Lluva, 2016], with the Differential Evolution (DE) algorithm [Storn and Price, 1997] being most suitable for complex problems such as that of low-thrust many-revolution trajectories. Nonetheless, it must be clarified that albeit capable of global optimization, the DE algorithm may not converge to the global optimum due to its randomized search technique. Additionally, the convergence performance depends on the DE

parameters specified by the user and the search stopping criteria. It should also be clarified that, despite this random nature, the DE implemented in this thesis can still benefit from an input a priori solution to limit the search space and thus lessen the computational load.
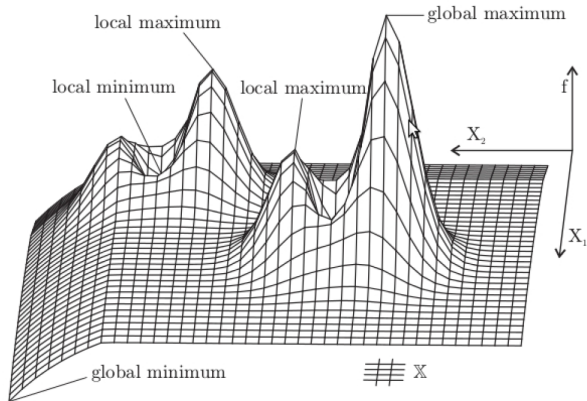
Figure 1.1: Illustration of local and global optima [Dunphy, 2014].
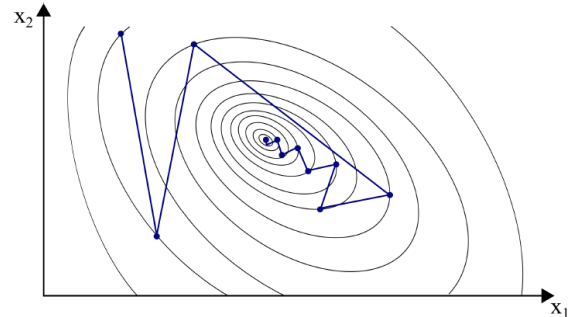
Figure 1.2: The gradient descent algorithm [Klukas, 2015].

Depending on the problem formulation and the design vector to be optimized, an a priori solution may consist of a thrust profile, such as the direct approach in [Betts, 2000], or the initial co-state values, such as the indirect shooting method in [Sanchez and Campa, 2014]. Nonetheless, the output solution can be modified to satisfy different input requirements. For example, IGEOR can intake the initial co-states from a previous optimization to simulate the trajectory, and the corresponding thrust profile can be stored to be later input in EPTOS. This allows the results of the methodology presented in this thesis to replace the a priori solution of IGEOR despite the different underlying formulation and design vector.

In the case of EPTOS, the a priori solution is of critical importance. This is because the underlying NLP optimizer may only yield a local optimum if this initial guess is far from the global optimal trajectory. Additionally, it may also drastically affect the convergence rate and whether it does converge to a feasible trajectory in the first place. For this reason, IGEOR was developed using an indirect formulation that satisfies the analytical optimal dynamics and was combined with a DE algorithm that yields near global optimum values of initial co-states. However, its indirect nature limits the amount of orbital perturbations and simultaneous optimization objectives that may be implemented. This does not constitute a significant weakness for simple problems such as a minimum Time-of-Flight (TOF) GTO-GEO trajectory because EPTOS can evaluate the full near-Earth perturbations model and refine the solution without difficulties. However, when the optimization of EPTOS further incorporates propellant-minimization, final geodetic longitude targeting, or intricate operational constraints such as a maximum slew-rate; the simplified a priori solution of IGEOR proves to be too far from a near global solution, and EPTOS has difficulties converging to a feasible trajectory that satisfies these needs. Nonetheless, the trade-off between TOF, propellant expenditure, and final geodetic longitude is of paramount importance to the positioning of GEO satellites as well as rendez-vous applications. Therefore, the recommendations of the GMV engineer who developed IGEOR [Montealegre-Avila, 2015] were to develop a method that can yield near optimal a priori trajectories that already satisfy such objectives and constraints. Since direct optimization methods are known to be most flexible in this regard, the author decided to investigate the extent to which a hybrid methodology may yield more suitable a priori solutions.

1.3. HERITAGE OF THE HYBRID OPTIMIZATION METHOD

The control parametrization method, often referred to as the "hybrid" approach, harnesses the benefits of both direct and indirect optimization methods, while avoiding their corresponding weaknesses. It was first presented in [Kluever and Pierson, 1995] and further developments are studied in [Kluever, 2010; Boudestijn, 2014; Gomez, 2015]. This methodology employs the first order optimality conditions of the OCP to analytically derive the optimal control parameters as function of the system states and co-states. Instead of further deriving the analytical EOM of the system co-states to complete the TPBVP like indirect methods, it implements the previous optimal control equations in a direct optimization approach. The resulting methodology is more efficient than a purely direct approach because it avoids solutions that do not satisfy the optimal control conditions. Additionally, the hybrid method retains the high flexibility of direct approaches such that additional

orbital perturbations or operational constraints can be readily added to the system dynamics without altering the mathematical foundation, which would need to be re-derived when using an indirect method.

In [Kluever and Pierson, 1995], the thrust magnitude was assumed constant and the control parameters were the two thrust steering angles. Through the first and second derivatives of the Hamiltonian with respect to these control angles, the optimal equations for each angle are derived as function of the system state and co-state at every epoch. Hence, the optimization variables become the system co-states instead of the original thrust control parameters. Whereas the thrust steering angles vary very irregularly at every second of the entire trajectory, the system co-states behave more smoothly and are linearly interpolated among a discrete set of nodes equally spaced in time. Therefore, this method considerably reduces the amount of optimization variables and hence the complexity of the NLP problem as well as the computational load. Additionally, it evaluates whether the spacecraft is within the Earth shadow region and automatically sets the thrust magnitude to zero.

In [Kluever, 2010], an Orbital Averaging (OA) technique is implemented to the original method in order to significantly reduce the computational propagation load. Instead of evaluating every propagation step within all revolutions of the trajectory, the OA approach employs an averaged state derivative to propagate the state directly over several revolutions at a time, with steps of up to five days. Because the state of low-thrust trajectories changes so smoothly and gradually, this method considerably reduces the propagation effort without a considerable loss of accuracy. Nonetheless, the variation becomes significant over five days so the averaged derivative needs to be updated regularly. In a test case for the minimum-time LEO-GEO transfer optimization, the resulting optimal TOF of 199.0 days is shown to be very accurate when compared to the 198.8 days solution from the Solar Electric Propulsion Trajectory Optimization Program (SEPSPOT) [Sackett et al., 1975], a widely used indirect approach developed by NASA.

In [Boudestijn, 2014], the previous method is re-derived using Modified Equinoctial Elements (MEE), which is superior to the classical Keplerian element state representation [Jimenez-Lluva, 2016]. Although Earth-shadow eclipses are incorporated, all other orbital perturbations are neglected. The results are validated with the minimum TOF test cases presented in [Kluever, 2010], and the new formulation is shown to have a broader scope of application as it does not suffer from the inherent discontinuities of the Keplerian state representation. This research is continued in Gomez [2015], where the force model is further refined by incorporating gravity gradient perturbations, an atmospheric model, third body perturbations, and a radiation fluence model. Additionally, a mechanism for multi-objective optimization is implemented to allow for trade-offs between different performance objectives. The results for minimum-TOF trajectories are validated with those of the previous hybrid studies and Pareto fronts are produced for the CleanSpace-One mission to illustrate the optimal combinations of TOF, propellant mass, and experienced radiation fluence.

The weakness of the hybrid methods developed in these studies is its limited applicability to minimum propellant optimization. Although every study investigated minimum propellant test cases, the final mass results deviated significantly from the optimal results indirect methods like SEPSPOT. Gomez [2015] acknowledged that these hybrid formulations are ill-conditioned for minimum propellant cases due to the constant thrust magnitude assumption. This is to be expected because continuous thrust is less efficient than variable thrust, since there are regions of the trajectory where the effect of the thrust input is less effective or undesirable. To further improve the hybrid methodology, it is clear that a mechanism must be implemented to allow for coasting (non-thrusting) arcs throughout the trajectory and therefore improve the accuracy of the minimum propellant solution.

In theory, the hybrid approach should be less accurate than indirect methods since the simplified co-state dynamics do not satisfy the analytical optimal EOM, but the previous studies showed that it yields high accuracy in minimum-TOF trajectory optimization when compared to the analytical global solution from indirect methods. Given the computational efficiency of the hybrid method, and more importantly due to the flexibility of its direct nature, the author decided to continue the research of Gomez [2015] and develop a novel hybrid methodology capable of evaluating coasting arcs beyond the Earth shadow regions and targeting the final geodetic longitude. The corresponding software prototype newly developed is referred to as Hybrid Optimization Software for Trajectories with Electric Propulsion (HOSTEP), and is incorporated within GMV's low-thrust optimization toolbox to evaluate the suitability of its solution as initial guess to GMV's high-fidelity optimizer.

1.4. LOW-THRUST COASTING ARCS HERITAGE

Several promising approaches to accomplish coasting arcs have been identified in literature. This section briefly describes how to model coasting arcs through Fourier series representations of the thrust control as

well as thrust or specific impulse modulation to implement .

1.4.1. THRUST MODELLING USING FOURIER SERIES

In [Hudson and Scheeres, 2009], a set of averaged Keplerian EOM is derived as functions of 14 Thrust Fourier Coefficients (TFC) based on eccentric anomaly. Moreover, the authors derived an offset correction for these EOM because some higher order effects of the Fourier series are not captured in the averaging process. These averaged secular EOM are then used to propagate a trajectory that is given a step input function for one of the thrust components, yielding very accurate results. In [Hudson and Scheeres, 2011], two methods are developed for low-thrust many-revolution optimization: an indirect approach that analytically solves the TPBVP and a least squares approach. The least squares approach is not deemed suitable for the scope of this thesis because it yields a single control law for the entire trajectory that does not allow for intermittent thrusting. The indirect method demonstrates the potential of the TFC concept as it allows thrust magnitude variations throughout the trajectory and hence coasting arcs. However, indirect methods were already deemed unsuitable due to their limited flexibility, requiring a new derivation for the inclusion of additional perturbations in the model. In [Ko and Scheeres, 2014], Ko and Scheeres showed that a particular set of six essential TFCs can yield very similar results as the set of 14 TFCs presented in [Hudson and Scheeres, 2009]. The author believes it may be possible to combine the hybrid approach from [Gomez, 2015] with this TFC technique. However, the author also identified simpler approaches in literature and deemed this method undesirable based on the complexity and analytical effort required to re-derive the TFC formulation in equinoctial state representation.

1.4.2. THRUST AND SPECIFIC IMPULSE MODULATION

In [Kluever, 2004], a modification of the original hybrid approach is presented that allows for variable specific impulse I_{sp}, instead of assuming a constant thrust magnitude. This control laws that stem from this strategy could be re-derived in equinoctial state representation and combined with the former hybrid methodology from [Gomez, 2015]. By applying the first order optimality conditions to the new Hamiltonian, an analytical equation can be derived for the optimal I_{sp} as a function of the trajectory states and co-states. In fact, the equations for the optimal thrust steering angles would remain unaffected by the variable I_{sp} modification, and one would just need to implement an additional equation. However, this study shows that the propellant mass benefit of I_{sp} modulation does not outweigh the required additional hardware mass.

A similar strategy is presented in [Gao and Kluever, 2004], where interplanetary low-thrust trajectories are studied using a modified hybrid method in combination with multiple shooting and a mechanism for coasting arcs through a variable thrust magnitude T. The results are promising in comparison to previous interplanetary studies, but indicate that the overall formulation is unsuitable for many-revolution problems. Nonetheless, the coasting arc mechanism may be adjusted to the problem at hand. This method differs from I_{sp} modulation in that the Hamiltonian is linear in T, so deriving the Hamiltonian does not yield a discrete equation for the optimal T, but a singular control problem. Consequently, T may be zero, maximal, or a value in between, depending on the sign of a switching function. The advantage is that, like the variable I_{sp} mechanism, the additional switching function for the optimal thrust magnitude T can be analytically derived without altering the equations for the optimal thrust steering angles. Therefore, the author deemed it most convenient to re-derive this switching function using MEE and combine it with the research of [Gomez, 2015] to allow for coasting arcs in the optimization process and thus develop a novel hybrid optimization methodology.

1.5. PROBLEM STATEMENT

This section distinguishes between project objectives and research questions. The former is related to the project sponsor requirements for the software prototype functionality and performance, whereas the research questions are aimed at extending the scientific research presented in previous literature.

1.5.1. PROJECT OBJECTIVES

The recommendations of Montealegre-Avila [2015], the GMV engineer who developed IGEOR, were to implement a full near-Earth perturbation model, implement a flexible constraint handling functionality, and enhance the propellant-minimization and final geodetic longitude targeting abilities, which were significantly limited in IGEOR yet are of paramount importance for GEO positioning and rendez-vous applications. The solution deemed most promising by the author is to employ a hybrid combination of direct and indirect methods

based on the research in [Gomez, 2015] and investigate whether it may potentially replace IGEOR in GMV's trajectory optimization toolbox. Furthermore, the recommendations of Gomez [2015] were to improve the hybrid methodology by implementing a mechanism for coasting (non-thrusting) arcs, implementing a mechanism for final geodetic longitude targeting, and upgrade the DE algorithm to a self-adaptive DE, such as the one available in ESA's Parallel Global Multiobjective Optimizer (PaGMO). The latter recommendation is not deemed a priority because it is more related to perfecting the performance rather than enhancing the scientific relevance of the new method. Moreover, it is not deemed a priority to implement a full near-Earth perturbations model or extensive operational constraints because these are known to be easily implemented in direct methods [Betts, 1998].

Due to the commercial nature of this project, copyrights, and compatibility reasons, the software developed in [Boudestijn, 2014; Gomez, 2015] cannot be employed in this project and a new prototype must be developed from scratch. Given the ambition of the previous recommendations and the limited time available for this thesis project, the author prioritized the sub-objectives as follows:

1. Develop the GUI and platform for the commercial high-level prototype Hybrid Optimization Software for Trajectories with Electric Propulsion (HOSTEP) while guaranteeing compatibility with all other functionalities of GMV's ***focussuite*** ® toolbox, such as PROPAG, EVENTS, and EPTOS.

2. Reproduce the hybrid methodology published in [Boudestijn, 2014], including orbital averaging, and develop an improved objective function that lessens the fine tuning effort required by the user for different optimization problems.

3. Implement the multi-objective optimization functionality presented in [Gomez, 2015] as well as Earth-shadow eclipses and second-order Earth oblateness perturbations.

4. Extend the hybrid methodologies previously published in literature by incorporating a mechanism adapted from the strategy in [Gao and Kluever, 2004] to allow for coasting (non-thrusting) arcs in the optimization process.

5. Compare the optimal minimum-time GTO-GEO trajectory with the results obtained with the indirect method in [Geffroy and Epenoy, 1997; Sanchez and Campa, 2014; Montealegre-Avila, 2015], and attempt to reproduce the time-propellant Pareto front presented in [Sanchez and Campa, 2014].

6. Extend the former hybrid methodology by enabling targeting of the final geodetic longitude, and compare its performance in rendez-vous problems with that of the indirect method presented in [Sanchez and Campa, 2014; Montealegre-Avila, 2015].

The resulting project objective is formulated as follows:

> *"Design and program a novel Hybrid Optimization Software for Trajectories with Electric Propulsion (HOSTEP) that continues the research presented in [Kluever and Pierson, 1995; Boudestijn, 2014; Gomez, 2015] by incorporating coasting arcs, a partial near-Earth perturbation model and a multi-objective optimization functionality with respect to time-of-flight, propellant expenditure, and final geodetic longitude, while demonstrating an equivalent or superior performance relative to the analytical indirect methodology presented in [Sanchez and Campa, 2014; Montealegre-Avila, 2015]"*

1.5.2. Research Questions

The following research questions aim to bridge the scientific gaps by providing results and objective conclusions that have not been previously presented in literature:

> *"To what extent can a hybrid combination of indirect and direct optimization methods using a multi-objective technique and a mechanism for coasting arcs yield superior optimal solutions than the analytical indirect method implemented in [Montealegre-Avila, 2015], specifically for minimum-propellant optimization problems of low-thrust many-revolution trajectories, while simultaneously allowing for targeting of the final geodetic longitude?"*

This question is divided into the following sub-questions for ease of the later discussion:

1. To what extent can the hybrid method employed in [Kluever, 2010; Boudestijn, 2014; Gomez, 2015] be successfully modified to incorporate a mechanism for coasting (non-thrusting) arcs?

(a) To what extent can a thrust switching function strategy similar to those shown in [Kluever, 2004; Gao and Kluever, 2004] be incorporated into the problem formulation to model coasting arcs and what is the effect on the accuracy and convergence of the algorithm?

2. To what extent can targeting of the final geodetic longitude be incorporated in the trajectory optimization process of this modified hybrid methodology?

(a) Can the targeting of the final geodetic longitude be accomplished through the numerical optimization process and if so, would this be more suitable that incorporating it in the problem Hamiltonian?

(b) How do the convergence properties of the hybrid method compare with those of indirect methods for rendez-vous optimization problems?

3. To what extent can this modified hybrid methodology yield more adequate a priori solutions than the current indirect optimization approach [Montealegre-Avila, 2015] employed by the project sponsor?

(a) How adequate is the relative performance for both minimum-time, minimum-propellant, and rendez-vous problems in terms of solution accuracy, problem flexibility, user effort, and computational performance?

1.6. STRUCTURE OF THIS REPORT

This thesis report is divided into the following six chapters: introduction, methodology, results, discussion, and conclusion. The introduction briefly describes the purpose of this thesis, the relevant heritage, and the research question. Chapter 2 describes the necessary details to reproduce the novel hybrid optimization methodology developed in this thesis. This includes the astrodynamics foundation, the formulation of the OCP, the propagation approaches, as well as the verification and validation activities. Chapter 3 provides the research results and the corresponding factual observations, whereas chapter 4 reveals the author's interpretations and own opinions of the results. Chapter 5 summarizes the conclusions and recommendations of this thesis research project. Appendix A explains the complete derivation of the OCP. Appendix B explains the details about the software tool developed, HOSTEP. Lastly, Appendix C provides additional data of the results cases and Appendix E specifies the hardware software employed for this project.

<div style="text-align: right;">

2

</div>

<div style="text-align: right;">

METHODOLOGY

</div>

"Perfection is not attainable, but if we chase perfection we can catch excellence." – Vince Lombardi.

This chapter provides the necessary details to reproduce the hybrid optimization methodology developed in this thesis. The reference frame, state representation, and the equations of motion are explained first, followed by the orbital perturbations. Section 2.4 describes the optimal control problem and reveals the optimal control laws, are analytically derived in Appendix A. Section 2.4 also describes the Differential Evolution algorithm and multi-objective optimization approach. Section 2.5 describes the two alternative propagation approaches employed, namely continuous integration and orbital averaging. Lastly, section 2.6 and 2.7 reveal the verification and validation activities respectively.

2.1. FRAMES OF REFERENCE

The chosen reference frame to express the disturbing forces on the spacecraft is the RSW radial rotating body frame [Vallado, 1997, p. 43] because the Equations of Motion (EOM) are readily available in this frame with the desired coordinate system from previous low-thrust trajectory studies [Betts, 2010; Falck and Dankanich, 2012; Boudestijn, 2014; Gomez, 2015]. The RSW frame is defined in Equation 2.1 and illustrated in Figure 2.1.

$$\boldsymbol{Q} = \begin{bmatrix} \hat{\boldsymbol{q}}_r \ \hat{\boldsymbol{q}}_\gamma \ \hat{\boldsymbol{q}}_h \end{bmatrix} = \begin{bmatrix} \dfrac{\boldsymbol{r}}{\|\boldsymbol{r}\|} & \dfrac{(\boldsymbol{r} \times \boldsymbol{v}) \times \boldsymbol{r}}{\|\boldsymbol{r} \times \boldsymbol{v}\| \|\boldsymbol{r}\|} & \dfrac{\boldsymbol{r} \times \boldsymbol{v}}{\|\boldsymbol{r} \times \boldsymbol{v}\|} \end{bmatrix} \tag{2.1}$$

The unit vectors $\hat{\boldsymbol{q}}_r$, $\hat{\boldsymbol{q}}_\gamma$, and $\hat{\boldsymbol{q}}_h$ indicate the r-, s-, and w- directions, respectively. $\hat{\boldsymbol{q}}_r$ is aligned with the radius vector, $\hat{\boldsymbol{q}}_h$ coincides with the angular momentum vector, and $\hat{\boldsymbol{q}}_\gamma$ completes the right-handed reference frame. The vectors $\boldsymbol{r}$ and $\boldsymbol{v}$ are the position and velocity vectors that constitute the Cartesian components in an Earth-Centered Earth-Fixed (ECEF) frame, which is described in the upcoming paragraphs. γ denotes the flight-path angle and h is the specific angular momentum.
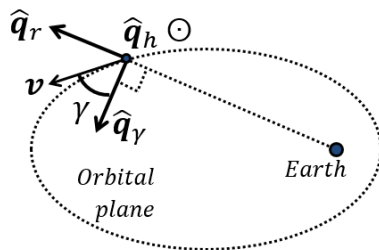
Figure 2.1: Illustration of the RSW frame.
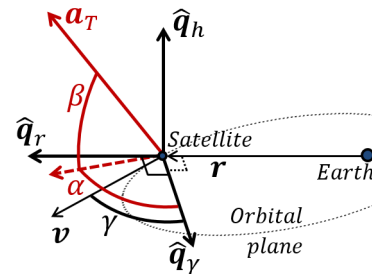
Figure 2.2: Thrust angles in the RSW frame.

Based on this reference frame, the thrust acceleration vector is defined by its magnitude $\|\boldsymbol{a}_T\|$ and two angles: the yaw steering angle α and the pitch steering angle β, as shown in Figure 2.2. It is worth mentioning that the yaw steering angle is usually measured with respect to the velocity vector but it is extended here to incorporate the flight-path angle γ. Hence, the thrust acceleration vector can be decomposed as,

$$\boldsymbol{a}_T^T = \|\boldsymbol{a}_T\| \left[\sin\alpha\cos\beta,\ \cos\alpha\cos\beta,\ \sin\beta\right] \tag{2.2}$$

Moreover, the thrust acceleration magnitude can be computed as the fraction of thrust force T over instantaneous spacecraft mass m [Kluever, 2010, p. 117]:

$$\|\boldsymbol{a}_T\| = \frac{T}{m} = \frac{2\eta P_{in}}{m g_0 I_{sp}} \tag{2.3}$$

which varies with thruster efficiency η, input power P_{in}, Earth's gravitational acceleration at sea level g_0, and specific impulse I_{sp}. It is worth mentioning that the methodology hereby presented does not employ inputs P_{in} and η, because the use of T enhances compatibility with EPTOS and IGEOR. Some previous low-thrust optimization studies such as [Boudestijn, 2014] do employ these parameters and Equation 2.3 is used to calculate the corresponding T values.

For the state representation of the trajectory, both an Earth-Centered-Inertial (ECI) and an ECEF reference frame are employed, depending on the coordinate system under consideration. Keplerian coordinates and Modified Equinoctial Elements (MEE) are expressed using the ECI J2000 frame. An ECI reference frame is a right-handed frame centered at the Earth's center of mass, with the x- and y- axes lying on the equatorial plane and the z-axis aligned with the North pole. The J2000 frame is selected because it is most commonly used. As its name may suggest, the x-axis is aligned with the mean equinox's position at noon (12:00 terrestrial time) on January 1st, 2000. It should be mentioned that ECI frames are not exactly inertial as the Earth's acceleration varies throughout its orbit about the Sun, but this effect is neglected in this thesis. For the specific application of targeting the final geodetic longitude of the satellite, which is interesting for the positioning of GEO satellites, the MEE state vector at the final time t_f is converted to geodetic coordinates, which are expressed about an ECEF reference frame. An ECEF frame is similar to ECI with the exception that its primary axis is fixed to a specific meridian and co-rotates with the Earth [Vallado, 1997, p. 39]. In this thesis, the Earth-Fixed Greenwich (ECG) frame is the chosen ECEF frame.

2.2. STATE REPRESENTATION AND EQUATIONS OF MOTION

The classical Keplerian orbital element representation defined in Equation 2.4 is useful to express the initial and final Boundary Conditions (BC) due to its intuitive meaning. These parameters include the semi-major axis a, eccentricity e, inclination i, right ascension of the ascending node (RAAN) Ω, argument of perigee ω, and true anomaly θ. These can be physically identified in Figure 2.3 and Figure 2.4.

$$\mathbf{oe}^T = \left[a,\ e,\ i,\ \Omega,\ \omega,\ \theta \right] \tag{2.4}$$
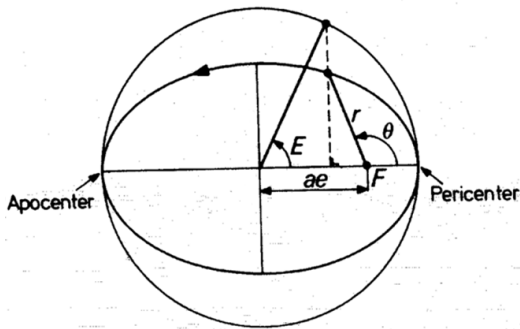
Figure 2.3: Keplerian elements a and e [Wakker, 2010].
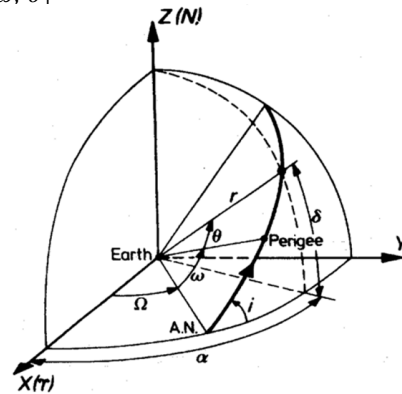
Figure 2.4: Keplerian elements i, Ω, ω, and θ [Wakker, 2010].

Nonetheless, Keplerian elements exhibit two important singularities: Ω is undefined for $i = 0, \pi$ rad and ω is undefined for $e = 0$. Boudestijn [2014] investigated the significance of the zero inclination discontinuity and concluded that its behaviour is detrimental for applications in planetocentric trajectory optimization. The propagation test case of the referenced study is shown in Figure 2.5 and features an Earth-bound orbital transfer intended to cross the equatorial plane. Instead of actually crossing the equatorial plane towards the target orbit with a negative inclination, the propagation became ill-conditioned due to a wrinkle effect at $i = 0$ rad. Boudestijn [2014] argued that as the inclination becomes zero, Ω suddenly increases by π rad due to the singu-

larity, thus causing the inclination to become positive in the next propagation step. This repeating behaviour causes the wrinkle effect and prevents the propagation from crossing the equatorial plane, which is unacceptable for the problem at hand because some orbital transfers of interest may not be simulated.
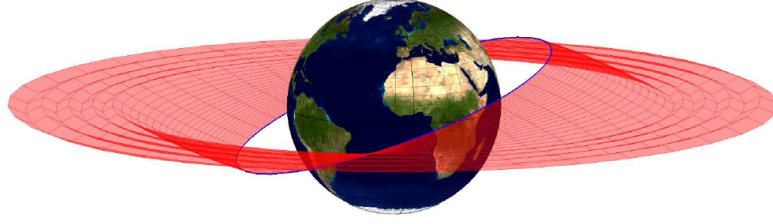
Figure 2.5: Illustration of the "wrinkle" effect experienced with a Keplerian state representation [Boudestijn, 2014].

For this reason, all internal computations of HOSTEP employ MEE, which are an alternative state representation approach that do not exhibit the singularities of Keplerian elements. MEE were proposed in [Walker et al., 1985] and further improved in [Walker, 1986], and are defined by Equation 2.5 to Equation 2.10. The survey in [Hintz, 2008] concluded it is the only non-singular coordinate set for all values of eccentricity and inclination, and a recommended choice for "the integration of orbits with special and general perturbations as well as differential corrections in orbit determination."

$$p = a\left(1 - e^2\right) \qquad (2.5)$$

$$f = e\cos\left(\omega + \Omega\right) \qquad (2.6)$$

$$g = e\sin\left(\omega + \Omega\right) \qquad (2.7)$$

$$j = \tan\left(\frac{i}{2}\right)\cos\Omega \qquad (2.8)$$

$$k = \tan\left(\frac{i}{2}\right)\sin\Omega \qquad (2.9)$$

$$L = \Omega + \omega + \theta \qquad (2.10)$$

where the original MEE element h is referred to as j in this thesis to avoid confusion with the specific angular momentum h of the trajectory. The MEE set can be converted back to Keplerian coordinates as follows,

$$a = \frac{p}{\left(1 - f^2 - g^2\right)} \qquad (2.11)$$

$$e = \sqrt{f^2 + g^2} \qquad (2.12)$$

$$i = 2\mathrm{atan}\left(\sqrt{j^2 + k^2}\right) \qquad (2.13)$$

$$\Omega = \mathrm{atan2}\left(\frac{k}{\sqrt{j^2 + k^2}}, \frac{j}{\sqrt{j^2 + k^2}}\right) \qquad (2.14)$$

$$\omega = \mathrm{atan}\left(\frac{g}{f}\right) - \mathrm{atan}\left(\frac{k}{j}\right) = \mathrm{atan2}\left(gj - fk, fj + gk\right) \qquad (2.15)$$

$$\theta = L - \Omega - \omega \qquad (2.16)$$

Despite the claims in [Hintz, 2008], it should be noted that the MEE set experiences a singularity when $i = \pi$ rad, which causes the elements j and g to become indeterminate. Nonetheless, this corresponds to a purely retrograde orbit which is unexpected within the scope of application of this thesis research.

The EOM for these MEE orbital elements are given by Equation 2.17 to Equation 2.22, where the MEE and thrust vectors are expressed in the J2000 and RSW reference frames. These equations were derived from the Gauss's form of the Lagrange planetary equations and are employed regularly in low-thrust studies [Betts, 1994; Falck and Dankanich, 2012; Betts, 2015].

$$\frac{dp}{dt} = \sqrt{\frac{p}{\mu}}\frac{2p}{w}a_s \qquad (2.17)$$

$$\frac{df}{dt} = \sqrt{\frac{p}{\mu}}\left\{\sin L\, a_r + \frac{1}{w}\left[(w+1)\cos L + f\right]a_s - \frac{g}{w}\left[j\sin L - l\cos L\right]a_w\right\} \qquad (2.18)$$

$$\frac{dg}{dt} = \sqrt{\frac{p}{\mu}}\left\{-\cos L\, a_r + \frac{1}{w}\left[(w+1)\sin L + g\right]a_s + \frac{f}{w}\left[j\sin L - l\cos L\right]a_w\right\} \qquad (2.19)$$

$$\frac{dj}{dt} = \sqrt{\frac{p}{\mu}}\frac{s^2\cos L}{2w}a_w \qquad (2.20)$$

$$\frac{dk}{dt} = \sqrt{\frac{p}{\mu}}\frac{s^2\sin L}{2w}a_w \qquad (2.21)$$

$$\frac{dL}{dt} = \sqrt{\mu p}\left(\frac{w}{p}\right)^2 + \sqrt{\frac{p}{\mu}}\frac{1}{w}\left[j\sin L - l\cos L\right]a_w \tag{2.22}$$

where $\boldsymbol{a}_d^T = [a_r \ a_s \ a_w]$ is the total disturbing acceleration vector experienced by the spacecraft in the RSW reference frame and $\mu = 398600.441$ km^2·s^{-2} is the gravitational constant of Earth [Wertz, 2009, p. 859]. For simplicity, the EOM use the auxiliary variables w and s^2, which are defined by,

$$w = \frac{p}{r} = 1 + f\cos L + g\sin L \tag{2.23}$$

$$s^2 = 1 + j^2 + k^2 \tag{2.24}$$

Additionally, the spacecraft mass m is included in the state vector because it is also dependent on the thrust input through the entire trajectory. The state vector $\boldsymbol{x}$ employed in the computations is defined in Equation 2.25 and the mass flow is defined by Equation 2.26 [Gao and Kluever, 2004]:

$$\boldsymbol{x}^T = \left[p, \ f, \ g, \ j, \ k, \ L, \ m\right] \tag{2.25}$$

$$\frac{dm}{dt} = -\frac{T}{g_0 I_{sp}} \tag{2.26}$$

Moreover, the previous Keplerian state vector $\boldsymbol{œ}$ is used to express the initial orbit $\boldsymbol{œ}_0$, but it is modified as shown in Equation 2.27 to replace the true anomaly by the geodetic longitude Λ. This vector employed to express the target orbit $\boldsymbol{æ}_t$, and final orbit $\boldsymbol{æ}_f$:

$$\boldsymbol{æ}^T = \left[a, \ e, \ i, \ \Omega, \ \omega, \ \Lambda\right] \tag{2.27}$$

Geodetic coordinates – longitude Λ, latitude Φ', and altitude h – are of interest for terrestrial applications. In this case, the geodetic longitude is of critical importance for rendez-vous applications and the positioning of GEO communications satellites. When this type of problem is selected in the Graphical User Interface (GUI) of HOSTEP, the final geodetic longitude of the spacecraft in calculated and evaluated during the optimization. It is worth explaining the difference between geocentric and geodetic coordinates, which are defined with the North and South poles being the two intersections of the Earth's rotation axis and its surface, the equator being the great circle halfway between the poles; the parallels being the great circles parallel to the equator; and the meridians the great circles crossing the poles. The geocentric latitude, $\Phi \in \left(-\frac{\pi}{2}, \frac{\pi}{2}\right]$, is the angle between the equator and the point of interest, measured along its meridian and at the center of the geoid (defined positive in the Northwards direction relative to the equator). Conversely, instead of the Earth's center, the geodetic latitude Φ' employs a plane tangent to Earth's surface at the sub-satellite point P. This is illustrated in Figure 2.6, where the geodetic altitude h of the satellite is measured perpendicularly to the Earth's surface and not along the geocentric radius vector $\boldsymbol{r}$ [Wakker, 2010]. On the other hand, the longitude, $\Lambda \in (-\pi, \pi)$, is the arc length along the equator measured from the Greenwich meridian to the point of interest (defined positive in the Eastwards direction relative to the prime meridian), with the geocentric and geodetic counterparts being equivalent because Λ is not affected by Earth's oblateness.
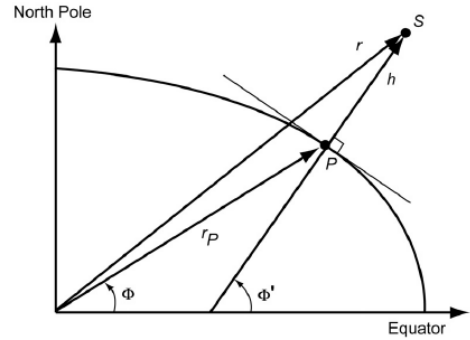
Figure 2.6: Geodetic coordinates [Wakker, 2010].

To calculate the geodetic longitude from the MEE state vector $\boldsymbol{x}$, the position vector must be computed in Cartesian coordinates using Equation 2.28 [Betts, 2015]. The geodetic longitude is then given by Equation 2.28. The calculation of the reminding geodetic coordinates is not necessary but can be found in [Zhu, 1994].

$$\boldsymbol{r} = \begin{bmatrix} x \\ y \\ z \end{bmatrix} = \begin{bmatrix} \frac{r}{s^2}\left(\cos L + \left(j^2 - k^2\right)^2\cos L + 2jk\sin L\right) \\ \frac{r}{s^2}\left(\sin L - \left(j^2 - k^2\right)^2\sin L + 2jk\cos L\right) \\ \frac{2r}{s^2}\left(j\sin L - k\cos L\right) \end{bmatrix} \tag{2.28}$$

$$\Lambda = \text{atan2}\left(y, x\right) \tag{2.29}$$

Lastly, the velocity vector can be calculated in Cartesian coordinates as shown in Equation 2.30 [Betts, 2015]. It should be mentioned that $\boldsymbol{v}$ is only used for the out-of-plane thrusting profile employed in validation test A2, see subsection 2.7.1. This is because the thrust profile is intended to increase the inclination and the direction of the out-of-plane thrust vector thus alternates for $v_z > 0$ and $v_z < 0$.

$$\boldsymbol{v} = \begin{bmatrix} v_x \\ v_y \\ v_z \end{bmatrix} = \begin{bmatrix} -\frac{1}{s^2}\sqrt{\frac{\mu}{p}}\left(\sin L + \alpha^2 \sin L - 2jk\cos L + g - 2fjk + \alpha^2 g\right) \\ -\frac{1}{s^2}\sqrt{\frac{\mu}{p}}\left(-\cos L + \alpha^2 \cos L + 2jk\sin L - f + 2gjk + \alpha^2 f\right) \\ \frac{2}{s^2}\sqrt{\frac{\mu}{p}}\left(h\cos L + k\sin L + fj + gk\right) \end{bmatrix} \tag{2.30}$$

2.3. ORBITAL PERTURBATIONS

One of the main advantages of the direct nature in the hybrid methodology is the flexibility it provides in adjusting the force model within the simulator. Conversely to indirect methods, the additional terms corresponding to an orbital perturbation may simply be included in the EOM, without the need to re-derive the analytical derivation again. The conclusions from the thesis literature study were that several orbital perturbations should be considered to enhance the accuracy of the a priori solution. This includes Earth-Sun eclipses, Earth's second degree zonal harmonic J_2 perturbation, third body attractions from the Moon and Sun, radiation pressure from the Sun, and atmospheric drag if low perigee altitudes are to be studied, such as a LEO or GTO initial condition. However, this was re-evaluated during the requirements evaluation phase of the thesis and its importance was deemed less critical than the novel development of the coasting arc and longitude targeting mechanisms. Therefore, only the most significant perturbations are incorporated: Earth-Sun eclipses and second order zonal harmonic perturbations, i.e. the J_2 effect. Further perturbations were not deemed to have a critical influence on the research results of the coasting arc and longitude targeting feasibility study. The evolution of the perturbing accelerations for a low-thrust GTO-GEO trajectory can be found in [Gebbett, 2014, p. 57] and supports this decision because the magnitude of the J_2 acceleration is comparable to that of the engine thrust. Nonetheless, the author recommends extending the force model to incorporate a full near-Earth perturbation model as it will further enhance the flexibility of HOSTEP and it should not affect the convergence radius of the hybrid method thanks to its direct nature. Further details may be found in section 5.2.

2.3.1. EARTH SHADOW

HOSTEP's force model includes an eclipse simulator developed and thoroughly validated by GMV. Its fundamental basis is superior to that of the conical shadow model employed in [Boudestijn, 2014; Gomez, 2015], which only distinguished between umbra, penumbra, and fully illuminated regions. Instead, this simulator calculates the relative position of the Sun and the Earth and the angle in between, γ, as well as their apparent radii α and β. When the bodies overlap, as illustrated below in Figure 2.7 and Figure 2.8, the eclipse simulator calculates the decrease in the observed Sun area and returns the percentage of received sunlight relative to the 100% condition in full sunlight. This procedure is a well established practice and further details may be found in books such as [Gill and Montenbruck, 2000].
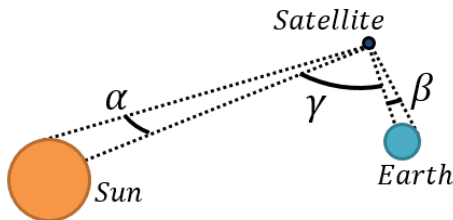
Figure 2.7: Sun- and Earth-satellite angles, not drawn to scale.
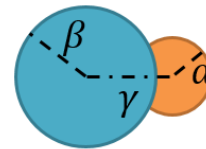
Figure 2.8: Over-positioning of bodies during eclipse, not drawn to scale.

HOSTEP allows the user to specify the minimum light percentage threshold to power the engines. The threshold employed for the test cases in this thesis is 80%, but the author warns that it may differ significantly for different satellite platforms and should therefore be adjusted accordingly.

2.3.2. EARTH J2 PERTURBATION

The J_2 perturbation of Earth is the most pronounced zonal harmonic perturbation arising from the geoid's non-homogeneous mass distribution, also referred to as oblateness. A fundamental description of this type of perturbations may be found in well established books such as [Vallado, 1997; Gill and Montenbruck, 2000]. The J_2 perturbing accelerations are defined in the RSW frame as follows [Kechichian, 2000],

$$a_{r,J_2} = -\frac{3\mu J_2 R_E^2}{2r^4}\left(1 - 12\frac{\left(j\sin(L) - k\cos(L)\right)^2}{s^4}\right) \tag{2.31}$$

$$a_{s,J_2} = -\frac{12\mu J_2 R_E^2}{r^4}\left(\frac{\left(j\sin(L) - k\cos(L)\right)\left(j\cos(L) + k\sin(L)\right)}{s^4}\right) \tag{2.32}$$

$$a_{w,J_2} = -\frac{6\mu J_2 R_E^2}{r^4}\left(\frac{\left(j\sin(L) - k\cos(L)\right)\left(1 - j^2 - k^2\right)}{s^4}\right) \tag{2.33}$$

where s^2 is the auxiliary variable previously defined in Equation 2.24, r is the magnitude of the spacecraft's radius vector, $R_E = 6378.136$ km is the equatorial radius of Earth and $J_2 = 1.082626 \times 10^{-3}$ is a dimensionless constant [Wertz, 2009, p. 859]. When the user selects to model the J_2 effect in HOSTEP, the previous accelerations are added to the thrust acceleration components to calculate the total disturbing acceleration $\boldsymbol{a}_d$ that can substituted in the EOM Equation 2.17 to Equation 2.22.

2.4. OPTIMAL CONTROL PROBLEM

This section describes how the hybrid methodology approaches the Optimal Control Problem (OCP). First, the optimal thrust control laws are presented, with the corresponding derivations explained in Appendix A. Afterwards, the employed Differential Evolution (DE) algorithm is described, together with the suggested tuning parameters. Lastly, the mechanism for multi-objective optimization is explained.

2.4.1. OPTIMAL THRUST CONTROL LAWS

This section reveals the equations that yield the optimal thrust steering angles, α^* and β^*, and the thrust magnitude T^*. It is important to remember that the hybrid method does not aim to fully solve the Two Point Boundary Value Problem (TPVBP), like indirect methods, but rather to derive a control law that efficiently parametrizes the thrust vector and allows to solve the OCP through a direct approach.

The derivation of the optimal thrust steering angles was originally presented in [Kluever, 2010] using Keplerian elements, and the formulation using the MEE set was derived in [Boudestijn, 2014]. Unlike the former hybrid studies, the methodology hereby developed does not assume constant thrust because [Gomez, 2015] concluded that it severely hinders the solution accuracy for minimum-propellant optimization, relative to the global optimum from indirect methods. Consequently, a new optimal thrust control law is required.

An OCP entails a system with a state defined by $\boldsymbol{x}(t)$, a control input defined by $\boldsymbol{u}(t)$, and system dynamics given by the set of ordinary differential equations $\dot{\boldsymbol{x}}(t) = f\left[\boldsymbol{x}(t), \boldsymbol{u}(t), t\right]$. The objective function of the OCP, hereafter denoted F instead of J to avoid confusion with J_2, is defined in standard form in Equation 2.34.

$$F = \Phi\left[\boldsymbol{x}(t_f), t_f\right] + \int_{t_0}^{t_f} \mathcal{L}\left[\boldsymbol{x}(t), \boldsymbol{u}(t), t\right] dt \tag{2.34}$$

with Φ and $\mathcal{L}$ representing the Mayer and Lagrange terms respectively and $\boldsymbol{u}(t)^T = \left[\alpha, \beta, T\right]$ the control vector. According to the optimal control theory developed by Pontryagin [1986], the optimal conditions that yield the optimum of the TPBVP are those that minimize the Hamiltonian equation defined by Equation 2.35.

$$\mathcal{H} = \mathcal{L} + \boldsymbol{\lambda}^T \cdot \dot{\boldsymbol{x}} \tag{2.35}$$

where the co-state vector $\boldsymbol{\lambda}$ contains functions of time that can be analytically derived using the transversality conditions. In essence, these co-states indicate the relative priority of the variation of each state parameter over time. It is worth mentioning that, unlike the physically intuitive objective function, this Hamiltonian equation is merely a mathematical tool useful for the analytical derivation of the optimal control laws. For further details

about the underlying control theory, the reader is referred to the literature study report that precedes this thesis [Jimenez-Lluva, 2016] and well established books such as [Bryson and Ho, 1975; Pontryagin, 1986]. Boudestijn [2014], and subsequently Gomez [2015], employed the following Hamiltonian:

$$\mathcal{H}_{[\text{Gomez, 2015}]} = \lambda_p \frac{dp}{dt} + \lambda_f \frac{df}{dt} + \lambda_g \frac{dg}{dt} + \lambda_j \frac{dj}{dt} + \lambda_k \frac{dk}{dt} \tag{2.36}$$

which does not feature the MEE element L because it becomes redundant through the use of Orbital Averaging (OA). The spacecraft mass m is not included in Equation 2.36 either because it is independent of the control parameters, due to the constant thrust assumption. Since this assumption is no longer applied, the spacecraft mass is dependent on the variable thrust magnitude. Therefore, the mass flow must be included,

$$\mathcal{H}_{\text{HOSTEP}} = \mathcal{H}_{[\text{Gomez, 2015}]} + \lambda_m \frac{dm}{dt} \tag{2.37}$$

Using this Hamiltonian, the optimal thrust control laws are analytically derived in Appendix A. The resulting optimal thrust steering angles are shown below in Equation 2.38 to Equation 2.41.

$$\sin \alpha^* = \frac{-\left(\Lambda_{f,1}^{\alpha} - \Lambda_{g,1}^{\alpha}\right)}{\sqrt{\left(\Lambda_{f,1}^{\alpha} - \Lambda_{g,1}^{\alpha}\right)^2 + \left(\Lambda_p^{\alpha} + \Lambda_{f,2}^{\alpha} + \Lambda_{g,2}^{\alpha}\right)^2}} \tag{2.38}$$

$$\cos \alpha^* = \frac{-\left(\Lambda_p^{\alpha} + \Lambda_{f,2}^{\alpha} + \Lambda_{g,2}^{\alpha}\right)}{\sqrt{\left(\Lambda_{f,1}^{\alpha} - \Lambda_{g,1}^{\alpha}\right)^2 + \left(\Lambda_p^{\alpha} + \Lambda_{f,2}^{\alpha} + \Lambda_{g,2}^{\alpha}\right)^2}} \tag{2.39}$$

$$\sin \beta^* = \frac{-\left(-\Lambda_{f,3}^{\beta} + \Lambda_{g,3}^{\beta} + \Lambda_j^{\beta} + \Lambda_k^{\beta}\right)}{\sqrt{\left(-\Lambda_{f,3}^{\beta} + \Lambda_{g,3}^{\beta} + \Lambda_j^{\beta} + \Lambda_k^{\beta}\right)^2 + \left(\Lambda_p^{\beta} + \Lambda_{f,1}^{\beta} - \Lambda_{g,1}^{\beta} + \Lambda_{f,2}^{\beta} + \Lambda_{g,2}^{\beta}\right)^2}} \tag{2.40}$$

$$\cos \beta^* = \frac{-\left(\Lambda_p^{\beta} + \Lambda_{f,1}^{\beta} - \Lambda_{g,1}^{\beta} + \Lambda_{f,2}^{\beta} + \Lambda_{g,2}^{\beta}\right)}{\sqrt{\left(-\Lambda_{f,3}^{\beta} + \Lambda_{g,3}^{\beta} + \Lambda_j^{\beta} + \Lambda_k^{\beta}\right)^2 + \left(\Lambda_p^{\beta} + \Lambda_{f,1}^{\beta} - \Lambda_{g,1}^{\beta} + \Lambda_{f,2}^{\beta} + \Lambda_{g,2}^{\beta}\right)^2}} \tag{2.41}$$

where Λ_q^{α}, and Λ_q^{β} are the constants in the partial derivatives of $\mathcal{H}$ with respect to α and β respectively that correspond to the qth element in $\boldsymbol{x}$. These constants are defined in equations Equation 2.42 to Equation 2.55:

$$\Lambda_{f,1}^{\alpha} = \lambda_f \sqrt{\frac{p}{\mu}} \cos \beta \sin L \tag{2.42}$$

$$\Lambda_{f,2}^{\alpha} = \lambda_f \sqrt{\frac{p}{\mu}} \frac{\left[(w+1)\cos L + f\right]\cos \beta}{w} \tag{2.43}$$

$$\Lambda_p^{\alpha} = \lambda_p \sqrt{\frac{p}{\mu}} \frac{2p}{w} \cos \beta \tag{2.44}$$

$$\Lambda_{f,1}^{\beta} = \lambda_f \sqrt{\frac{p}{\mu}} \sin \alpha \sin L \tag{2.45}$$

$$\Lambda_{f,2}^{\beta} = \lambda_f \sqrt{\frac{p}{\mu}} \frac{\left[(w+1)\cos L + f\right]\cos \alpha}{w} \tag{2.46}$$

$$\Lambda_{f,3}^{\beta} = \lambda_f \sqrt{\frac{p}{\mu}} \frac{\left(j\sin L - k\cos L\right)g}{w} \tag{2.47}$$

$$\Lambda_j^{\beta} = \lambda_j \sqrt{\frac{p}{\mu}} \frac{s^2 \cos L}{2w} \tag{2.48}$$

$$\Lambda_{g,1}^{\alpha} = \lambda_g \sqrt{\frac{p}{\mu}} \cos \beta \cos L \tag{2.49}$$

$$\Lambda_{g,2}^{\alpha} = \lambda_g \sqrt{\frac{p}{\mu}} \frac{\left[(w+1)\sin L + g\right]\cos \beta}{w} \tag{2.50}$$

$$\Lambda_p^{\beta} = \lambda_p \sqrt{\frac{p}{\mu}} \frac{2p}{w} \cos \alpha \tag{2.51}$$

$$\Lambda_{g,1}^{\beta} = \lambda_g \sqrt{\frac{p}{\mu}} \sin \alpha \cos L \tag{2.52}$$

$$\Lambda_{g,2}^{\beta} = \lambda_g \sqrt{\frac{p}{\mu}} \frac{\left[(w+1)\sin L + g\right]\cos \alpha}{w} \tag{2.53}$$

$$\Lambda_{g,3}^{\beta} = \lambda_g \sqrt{\frac{p}{\mu}} \frac{\left(j\sin L - k\cos L\right)f}{w} \tag{2.54}$$

$$\Lambda_k^{\beta} = \lambda_k \sqrt{\frac{p}{\mu}} \frac{s^2 \sin L}{2w} \tag{2.55}$$

where the square root terms cancel out in the derivation of α^* and β^* angles but not in the derivation of T^*. They may thus be removed from Λ_q^{α} but not from Λ_q^{β} since the latter is to be re-used in the T^* control law. It is worth recalling that the thrust acceleration vector is given by $\boldsymbol{a}_T^T = \|\boldsymbol{a}_T\| \left[\sin \alpha \cos \beta, \ \cos \alpha \cos \beta, \ \sin \beta\right]$, mean-

ing the sine and cosine terms can be directly substituted in the EOM and it is not necessary to calculate values of the steering angles. Nonetheless, these could be calculated through the relationship $\alpha = \text{atan2}(\sin\alpha, \cos\alpha)$, since both α and β range from $-90°$ to $90°$.

The previous control laws are identical to those derived in [Boudestijn, 2014] because the new mass co-state term disappears during the differentiation process, see the complete derivation in Appendix A. The third control law corresponding to the thrust magnitude T, however, constitutes a novel enhancement in the hybrid methodology hereby presented because all previous studies assumed constant thrust. For this derivation, the Hamiltonian derivative is evaluated with respect to T:

$$
\frac{\partial \mathcal{H}}{\partial T} = \Lambda_p^\beta \cos\beta \frac{1}{m} + \left[\Lambda_{f,1}^\beta \cos\beta + \Lambda_{f,2}^\beta \cos\beta - \Lambda_{f,3}^\beta \sin\beta \right] \frac{1}{m}
$$
$$
+ \left[-\Lambda_{g,1}^\beta \cos\beta + \Lambda_{g,2}^\beta \cos\beta + \Lambda_{g,3}^\beta \sin\beta \right] \frac{1}{m} + \Lambda_j^\beta \sin\beta \frac{1}{m} + \Lambda_k^\beta \sin\beta \frac{1}{m} - \lambda_m \frac{1}{g_0 I_{sp}} = S_t \qquad (2.56)
$$

which leads to a bang-bang control problem, as expected, because the Hamiltonian varies linearly with T. Thus, the switching function defined by S_t determines the optimal thrust conditions [Pontryagin, 1986]:

$$
T = \begin{cases} 0, & \text{if } S_t > 0 \\ T_{max}, & \text{if } S_t < 0 \end{cases} \qquad (2.57)
$$

It should be clarified that there may exist a third condition, known as a singular arc, yielding $0 < T < T_{max}$ if $S_t = 0$ and $\dot{S}_t = 0$. Nonetheless, the duration of such arc is rather limited in practical applications when compared with the other two conditions and, more importantly, the condition $S_t = 0$ and $\dot{S}_t = 0$ may never be satisfied due to the numeric nature of the simulation. Therefore, the author decided to neglect the possibility of singular arcs, thus simplifying the problem to a bang-bang control.

2.4.2. DESIGN VECTOR

The previous control laws show that $\boldsymbol{u}^*(t) = f(\boldsymbol{x}, \boldsymbol{\lambda})$, such that the optimal thrust components in the RSW frame can be substituted in the EOM to compute $\dot{\boldsymbol{x}} = f(\boldsymbol{x}, \boldsymbol{\lambda})$. This nature of the hybrid method significantly reduces the amount of optimization variables and allows for a practical computation time as compared to general direct methods such as [Betts, 2010]. In contrast to indirect methods, which derive the co-state EOM $\dot{\boldsymbol{\lambda}}(t)$ and optimize the initial values $\boldsymbol{\lambda}_0$ [Geffroy and Epenoy, 1997], the hybrid strategy aims to approximate the optimal co-state dynamics $\boldsymbol{\lambda}(t)$ instead of fully deriving the TPVBP to obtain the analytical co-state EOM. To approximate the optimal co-state dynamics and avoid the need to re-derive the TPVBP for any change in the problem formulation, the hybrid method artificially defines the co-state values at n_s nodes throughout the trajectory: $\boldsymbol{\lambda}_0, \boldsymbol{\lambda}_1, ..., \boldsymbol{\lambda}_{n_s}$. The values at these nodes are then optimized and linear interpolation is employed in between [Boudestijn, 2014]. These nodes were originally equidistant with respect to the semi-major axis [Kluever, 2010] but Boudestijn [2014] showed that it is more desirable to distribute them equally in time. To avoid confusion with with the number of integration steps per revolution, the GUI refers to this as the number of co-state arcs $N_{arcs} = n_s - 1$. This is illustrated in Figure 2.9 for single and dual co-state arcs.
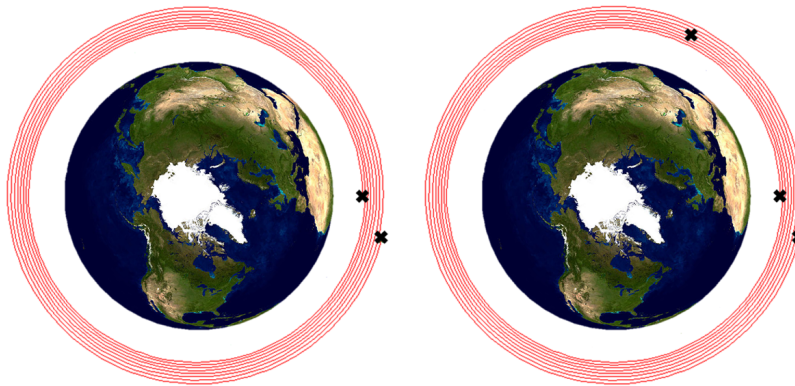
Figure 2.9: Illustration of the co-state nodes, which are equidistant in time, for $N_{arcs} = 1$ and $N_{arcs} = 2$, adapted from [Gomez, 2015].

The number of co-states to be optimized therefore depends on the number of co-state arcs. Moreover, the amount of co-states per node depends on whether a minimum-time problem is being evaluated or whether thrust is variable. In the former case, every co-state discretization node corresponds to five co-states to be optimized whereas, in the latter case, every additional co-state arc introduces six optimization parameters, i.e. including the mass co-state λ_m. Additionally, the Time-of-Flight (TOF) denoted t_f is incorporated in the design vector as it is required for the propagation [Gomez, 2015; Geffroy and Epenoy, 1997]. Nonetheless, it should be clarified that t_f remains a free variable in the optimal control problem, unless the upper and lower bounds are manually constrained to a discrete value, and TOF-minimization is accomplished through the objective function, see subsection 2.4.3. Thus, the two cases depicted in Figure 2.9 would respectively correspond to 11 and 16 optimization variables, for a minimum-time problem, or 13 and 19 optimization parameters if the thrust magnitude is variable. This hybrid formulation constitutes a single shooting problem, where a set of given parameters is simulated and the terminal boundary condition of the propagation is evaluated in the objective function. Further details about single shooting discretization and other alternative schemes can be found in [Jimenez-Lluva, 2016].

It must be clarified, that the simplified co-state dynamics of the hybrid method should, in theory, hinder the solution accuracy relative to the analytical global optimum from indirect methods. This could be enhanced through more sophisticated interpolation methods such as the Chebyshev polynomials described in [Fox et al., 1968; Mason and Handscomb, 2002]. However, this was deemed unnecessary because the original hybrid method yielded a high accuracy for the GTO-GEO transfer – with a minimum TOF of 199.0 days for a single co-state arc [Kluever, 2010] – in comparison to the 198.8-day solution computed with the indirect method in SEPSPOT [Sackett et al., 1975]. Furthermore, Gomez [2015] demonstrated that although slightly improving the solution, increasing the number of co-state arcs leads to significant increments in the computational cost. Therefore, a single co-state arc is used hereafter and the design vector $\boldsymbol{y}$ to be optimized is defined as:

$$\boldsymbol{y}^T = \left[t_f, \, \boldsymbol{\lambda}_0^T, \, \boldsymbol{\lambda}_f^T \right] \tag{2.58}$$

2.4.3. MULTI-OBJECTIVE OPTIMIZATION

In practical applications, one single optimization objective may not be enough. This is because there are usually several conflicting mission objectives of high importance, such as the TOF and the required propellant mass or the radiation experienced by the spacecraft. This raises the need for Multi-Objective Optimization (MOO) which can be accomplished by assigning relative weights to each objective [Deb et al., 2002]:

$$F(\boldsymbol{y}) = W_1 f_1(\boldsymbol{y}) + W_2 f_2(\boldsymbol{y}) + ... + W_n f_n(\boldsymbol{y}) \tag{2.59}$$

where F is referred to as the Aggregate Objective Function (AOF), $\boldsymbol{f}$ is the vector containing the individual optimization objectives, $\boldsymbol{y}$ is the vector to be optimized, and $\boldsymbol{W}$ are the respective multi-objective weights [Deb et al., 2002]. These weights are critical to ensure that the individual components of the AOF vary with similar orders of magnitude, which enhances the convergence of optimization algorithms. Moreover, by varying the weights of each objective, one may find a broad spectrum of possible combinations that can be illustrated in a Pareto front diagram. This diagram shows all the possible combinations of two objectives such that one objective cannot be further improved without negatively affecting the other, which can be very resourceful in the decision making process. An example Pareto front is illustrated in Figure 2.10, which features the GTO-GEO propellant minimization scenario that is approximated using the hybrid methodology in section 3.2.
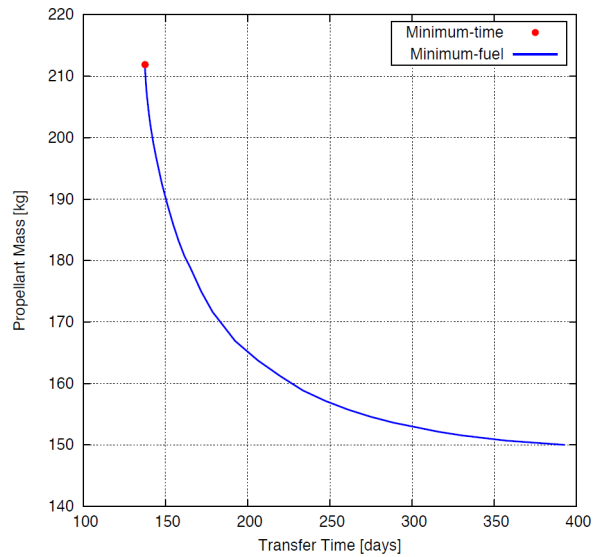
Figure 2.10: Pareto front for a GTO-GEO transfer [Sanchez and Campa, 2014].

Boudestijn [2014] employed two different AOF for the minimum time and minimum propellant case, Equation 2.60 and Equation 2.61 respectively, both of which evaluate only the first three Keplerian elements a, e,

and i. Gomez [2015] expanded this AOF to also target elements ω and Ω and to allow for a multi-objective optimization with respect to TOF, propellant expenditure, and radiation fluence Ψ. The AOF employed in the indirect method presented in Sanchez and Campa [2014] is shown in Equation 2.63.

$$F_{\text{[Boudestijn, 2014], min.time}} = \sum_{q=1}^{3} W_q \left| \text{œ}_q^{final} - \text{œ}_q^{target} \right| + t_f \tag{2.60}$$

$$F_{\text{[Boudestijn, 2014], min.prop}} = \sum_{q=1}^{3} W_q \left| \text{œ}_q^{final} - \text{œ}_q^{target} \right| + W_m \left(1 - \frac{m_f}{m_0} \right) \tag{2.61}$$

$$F_{\text{[Gomez, 2015]}} = \sum_{q=1}^{5} W_q \left| x_q^{final} - x_q^{target} \right| + W_m \left(1 - \frac{m_f}{m_0} \right) + W_t \left(t_f \right) + W_r \left(\Psi \right) \tag{2.62}$$

$$F_{\text{[Sanchez and Campa, 2014]}} = \sqrt{ \sum_{q=1}^{5} W_q \left(x_q^{final} - x_q^{target} \right)^2 + W_{\lambda_m} \left(\lambda_m^{final} \right)^2 + W_{\lambda_L} \left(\lambda_L^{final} \right)^2 } \tag{2.63}$$

where $\text{œ}_q^{final} - \text{œ}_q^{target}$ and $x_q^{final} - x_q^{target}$ are the difference between the target and final achieved value of the qth Keplerian and MEE element, respectively. It should be noted that Boudestijn [2014] only targeted the first three Keplerian elements – a, e, and i – because the others were not included in the Hamiltonian. Moreover, Gomez [2015] did not target the true longitude because he was simultaneously employing the orbital averaging technique, which sacrifices the information of this rapidly-changing variable, see section 2.5. m_0 and m_f are respectively the initial and final total mass of the spacecraft, and t_f is the final time, i.e. the TOF of the trajectory. λ_m^{final} and λ_L^{final} are the co-states of the total mass and true longitude respectively, and they are included in the indirect methodology by Sanchez and Campa [2014] because they are free variables at $t = t_f$ and should therefore yield null values, according to the transversality conditions of the optimal TPBVP [Pontryagin, 1986]. The respective weights W of the parameters were established iteratively in [Boudestijn, 2014; Gomez, 2015] for every test case. In [Sanchez and Campa, 2014], however, all the parameters are dimensionless such that it is sufficient to use unitary weights for all constraints in the objective function, and the square root serves to decrease the numerical value of the residual and hence its fluctuations.

The AOF implemented in HOSTEP harnesses the advantages of the previous examples, and incorporates a more elaborate scaling procedure to reduce the iterative effort required for every different problem. It incorporates the deviation from the desired orbit, the TOF, and the propellant expenditure:

$$F_{\text{HOSTEP}} = \sum_{q=1}^{6} W_q (\epsilon_q)_{sc}^2 + W_t \left(t_f \right) + W_m \left(1 - \frac{m_f}{m_0} \right) \tag{2.64}$$

where ϵ_q represents the orbit error $\text{æ}_q^{final} - \text{æ}_q^{target}$, which in this case targets the first five Keplerian elements and the final geodetic longitude. The sc subscript indicates that this error is scaled with respect to a reference value – the scaling procedure is explained in the upcoming paragraph. The first term aims to minimize the orbit error for all elements, except the rapidly changing variable θ or L, and retains the squared power strategy from [Sanchez and Campa, 2014] to prioritize this objective if the deviation becomes too large. The second and third terms aim to minimize the TOF and propellant expenditure, using the same strategy as in [Gomez, 2015] because of its effective simplicity. This objective function does not feature a square root like that in [Sanchez and Campa, 2014] because the author deemed that the minor advantage of a decreased numeric residual might come at the expense of undesired rapid fluctuations in the vicinity of zero and a potential singularity.

The weights W_q, W_t, and W_m in Equation 2.64 assign a relative priority to each objective, with W_m being automatically nullified if a minimum-time problem is selected. The scaling procedure developed for $(\epsilon_q)_{sc}$, was intricately devised to allow the weights W_q to be set equal to 1.0 and thereby lessen the iterative effort required for fine tuning. The user may employ weights of 0.0 for the elements that need not be targeted, such as ω and Ω in certain a priori applications. The scaling procedure is shown below in Equation 2.68 and aims to scale the final orbit error such that each element attains a value $\in (0, 1]$ if the error is below or equal to the specified requirement, and a value $\in (1, \infty)$ otherwise. Upon squaring the final orbit error, its contribution to the AOF is thus nearly neglected if the final orbital elements are relatively close to the target values:

$$\epsilon_q = \left| \text{æ}_q^{target} - \text{æ}_q^{final} \right| \quad q = 1, 2, 3, 4, 5, 6 \tag{2.65}$$

$$d_q = \frac{1}{(\epsilon_q)_{ub} - (\epsilon_q)_{lb}} \tag{2.66}$$

$$b_q = 1 - k_q(\epsilon_q)_{ub} \tag{2.67}$$

$$(\epsilon_q)_{sc} = d_q\epsilon_q + b_q \tag{2.68}$$

where d and b are auxiliary vectors and $\boldsymbol{\epsilon}_{ub}$ and $\boldsymbol{\epsilon}_{lb}$ are the upper and lower bound vectors of the final orbit deviation. Based on GMV's experience in flight dynamics and trajectory optimization, the recommended error upper bound for optimal a priori solutions is provided in Table 2.1.

Table 2.1: Upper and lower bounds of the error between the final and target Keplerian orbital elements.

Keplerian element	Lower Bound $\boldsymbol{\epsilon}_{lb}$	Upper Bound $\boldsymbol{\epsilon}_{ub}$
Semi-major axis a [km]	0.0	100.0
Eccentricity e [-]	0.0	0.01
Inclination i [deg]	0.0	0.1
RAAN Ω [deg]	0.0	1.0
Arg. of perigee ω [deg]	0.0	1.0
Geodetic longitude Λ [deg]	0.0	1.0

2.4.4. DIFFERENTIAL EVOLUTION ALGORITHM

The Differential Evolution (DE) algorithm is a metaheuristic optimization approach that has been shown to be very suitable for complex global optimization problems [Hoving, 2015; Montealegre-Avila, 2015]. Like many metaheuristic methods, DE is inspired by proceesses in nature and is a further development of the Genetic Algorithms (GA) first presented in [Holland, 1975]. Unlike GA, DE evaluates the differences between the parent solution vectors in each generation before they are crossed over to yield the children solution vector for the next generation. The factual description of the DE algorithm may be found in the literature study report preceding this thesis [Jimenez-Lluva, 2016], in the original publication in [Storn and Price, 1997], or in well established optimization books like [Wahde, 2008].

HOSTEP features a *Fortran 90 ®* algorithm developed by Wang [2010] based on the original DE methodology published in [Storn and Price, 1997]. The decision to implement this algorithm, instead of more sophisticated DE algorithms freely available online, was based on its simplicity as it was readily available in the desired programming language, and because it had been shown to work well for the low-thrust optimization method employed in IGEOR [Montealegre-Avila, 2015]. Nonetheless, the author acknowledges the potential of self-adaptive DE algorithms, such as the one available in PaGMO [Biscani et al., 2010]. The advantage of such superior algorithm would be an enhanced computational time, because it enables parallel computing, and a reduced fine-tuning effort for the user, because it automatically optimizes the factors N_P, C_F, and C_R. This was not implemented in HOSTEP because it does not constitute a critical priority for the methodology prototype, yet the author recommends it for future work – see further details in section 5.2.

The DE algorithm requires three user inputs: the population size N_P, the cross-over rate C_R, and the scaling factor C_F. In the original publication, Storn and Price [1997] recommend a population size between $5D$ and $10D$, with D being the amount of optimization parameters, as well as starting values of $C_R = 0.1$ and $C_F = 0.5$. Their advice is to gradually increase the latter two in case of premature convergence and warn that C_R values between 0.9 and 1.0 might yield poor results albeit showing a faster convergence. In the previous low-thrust hybrid optimization studies, Boudestijn [2014] employed $N_P = 7D$, $C_R = 0.6$, and $C_F = 0.6$ for wide range of test cases with two OA arcs (i.e. 7 optimization parameters). In the original indirect method that was used to develop IGEOR, Sanchez and Campa [2014] used $N_P = 10D$, $C_R = 0.8$, and $C_F = 0.6$. The author found that the latter combination worked better for the problems analyzed in this thesis, with the increased population size helping to find better optima and the increased cross-over rate enhancing the convergence rate without jeopardizing the solution accuracy.

Additionally, the DE available in Wang [2010] was adjusted to allow for a randomized start or to intake a previous solution depending on the GUI settings. In the latter case, the input solution is used to define the upper and lower bounds of the optimization parameters, and then the DE process is initiated randomly as usual.

2.5. State Propagation

This section explains the details of the propagation techniques implemented in HOSTEP: Continuous Integration (CI) and Orbital Averaging (OA). The underlying integration scheme is a fixed-step Runge Kutta 4 (RK4) regardless of whether CI or OA is selected in the GUI. The decision to implement a fixed-step as integrator compared to a variable-step scheme was based on the literature study, which concluded that RK4 yields an acceptable accuracy for a priori low-thrust optimization [Jimenez-Lluva, 2016], and because its simplicity eased the gradual development of HOSTEP from scratch. Nonetheless, the modular architecture of HOSTEP allows for easily adding alternative schemes, and the author recommends implementing a variable-step integration scheme in future HOSTEP versions. This is because the step-size may be significantly increased at certain parts of the trajectory to reduce the propagation effort without jeopardizing the accuracy. Thorough descriptions about the mathematical logic behind variable-step integration schemes can be found in [Gill and Montenbruck, 2000]. Particularly, the literature study identified the RKF7(8) scheme as most convenient among variable-step schemes for low-thrust trajectory optimization applications [Jimenez-Lluva, 2016].

The OA method sacrifices the accuracy of the rapidly changing element (i.e. true anomaly or true longitude) for computational speed. Its counterpart, CI, yields a high-accuracy propagation for all orbital elements. The previous hybrid methodologies in [Boudestijn, 2014; Gomez, 2015] employed OA during the optimization process and CI for the final simulation of the optimal solution. However, this strategy is modified in HOSTEP to allow for using CI or OA irrespectively of whether the computational mode is optimization or simulation. This is because the author identified the future potential of HOSTEP to target also the final geodetic longitude in the optimization, which may only be possible if HOSTEP can employ CI during optimization – further details can be found in section 5.2. Therefore, HOSTEP's GUI allows the user to select CI or OA for either computational mode, optimization or simulation. Additionally, this architecture makes HOSTEP a resourceful research and commercial tool as it provides the flexibility to compute quick a priori solutions with OA as well as high-accuracy trajectories with CI. Furthermore, a post-processing option allows for comparing both CI and OA results – if selected together with the optimization mode, this option compares only the final optimized trajectory. Further information about the operational modes and post-processing options can be found in section B.3.

2.5.1. Continuous Integration

The CI propagation scheme is the higher accuracy but more computationally expensive option. It propagates the state of the orbit in MEE from $t = t_0$ to $t = t_f$ using n_k propagation steps per revolution, which is defined by a true longitude variation of $L = 2\pi$ rad. The use of true longitude, as compared to true anomaly, in CI propagation is preferred as it provides a useful insight for GEO applications. This sequential process is depicted in Figure 2.11. The author designed CI to propagate through discrete revolutions because this logic is necessary for the OA scheme and can thus be reused. Moreover, this logic easily allows for distributing the n_k propagation steps over an equidistant grid in true longitude instead of time. This is desirable to enhance the propagation accuracy near the pericentre where orbital perturbations, such as atmospheric drag, are most prominent [Jimenez-Lluva, 2016]. Nonetheless, since the EOM are expressed with respect to time, the true longitude propagation step $\Delta L = \frac{2\pi}{n_k}$ is converted to a time step, at every epoch, through $\Delta t = \Delta L \frac{dt}{dL}$, with the value of $\frac{dL}{dt}$ being readily available from the EOM, see Equation 2.22 in section 2.2.

Both the CI and OA modules were designed to propagate any combination of design parameters, even though some combinations may lead to hyperbolic orbits, re-entry trajectories, or solutions that do not satisfy the operational constraints. To avoid ill-conditioning of the optimization process, checks are implemented within the CI and OA scheme to avoid such bad solutions. When these violations are detected within the CI or OA propagation, the propagation process is halted and its output is manually set equal to the initial state vector, leading to a large objective function residual such that the solution is disregarded by the optimizer. Lastly, the CI and OA process are designed to stop the propagation when $t = t_f$ is reached, even if the current revolution is not yet completed, to avoid overshooting of the TOF.

2.5.2. Orbital Averaging

The OA technique was presented in [Gao and Kluever, 2005] and is a powerful approach to reduce the computational propagation load of each trajectory simulation throughout the optimization process [Jimenez-Lluva, 2016]. For example, a typical GTO-GEO low-thrust trajectory with about 200 orbital revolutions [Geffroy and Epenoy, 1997] is to be propagated using 30 n_k propagation steps per revolution. The classical CI technique would propagate the state vector from every step to the next, starting from the initial state $\boldsymbol{x}_0$ until the target
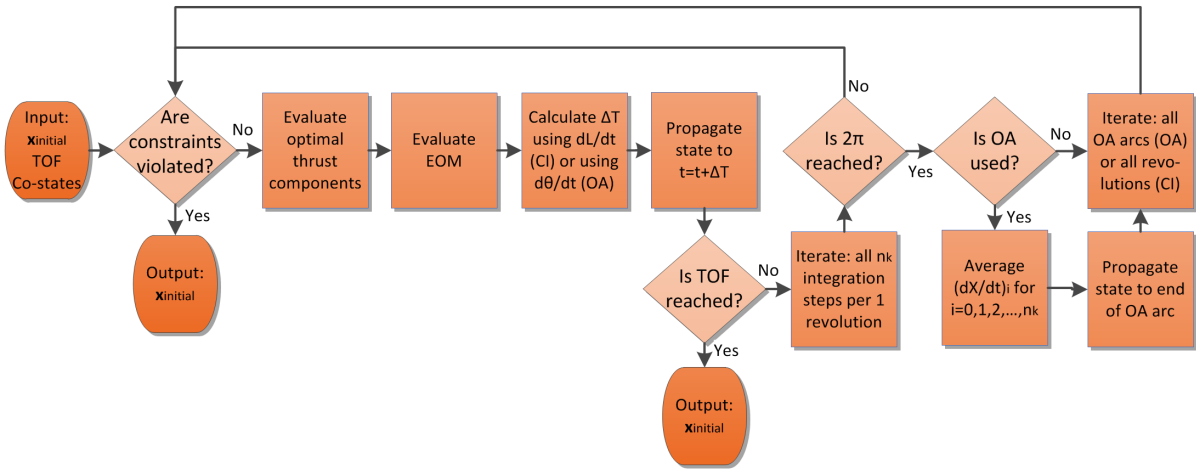
Figure 2.11: Work-flow logic of the propagator.

state $\boldsymbol{x}_t$ is reached and thus evaluating 30×200 steps. On the other hand, the OA approach aims to evaluate the 30 steps of only the first revolution, and then average these 30 state derivatives. Instead of proceeding to evaluate the steps of the next revolution, OA employs this averaged state derivative to propagate the state up to five days forward [Kluever, 2010]. After this five-day step, the variation of the orbital elements becomes too significant and the state derivative must be updated by evaluating the 30 nodes of the subsequent revolution and averaging them again. As compared to CI, OA would thus evaluate only 30×20 nodes, for an OA step-size of five days, thereby significantly reducing the computational propagation effort. Considering that the optimization process might simulate thousands of low-thrust trajectories until the global optimum is located, the OA scheme dramatically speeds up the optimization process.

In low-thrust trajectories, the orbital elements vary gradually and smoothly, meaning that the OA technique can be applied without a significant loss of accuracy. To support this claim, Kluever [2010] employed the OA technique with five-day time steps in a minimum-TOF LEO-GEO low-thrust transfer optimization. His result of 199.0 days was very accurate with respect to the 198.8 days solution from NASA's SEPSPOT indirect optimizer. The OA technique was further employed to numerical optimization of low-thrust trajectories in Gao and Kluever [2005] [Boudestijn, 2014] [Gomez, 2015], which demonstrated it to be a very effective technique as it was faster than CI while achieving a satisfactory accuracy.
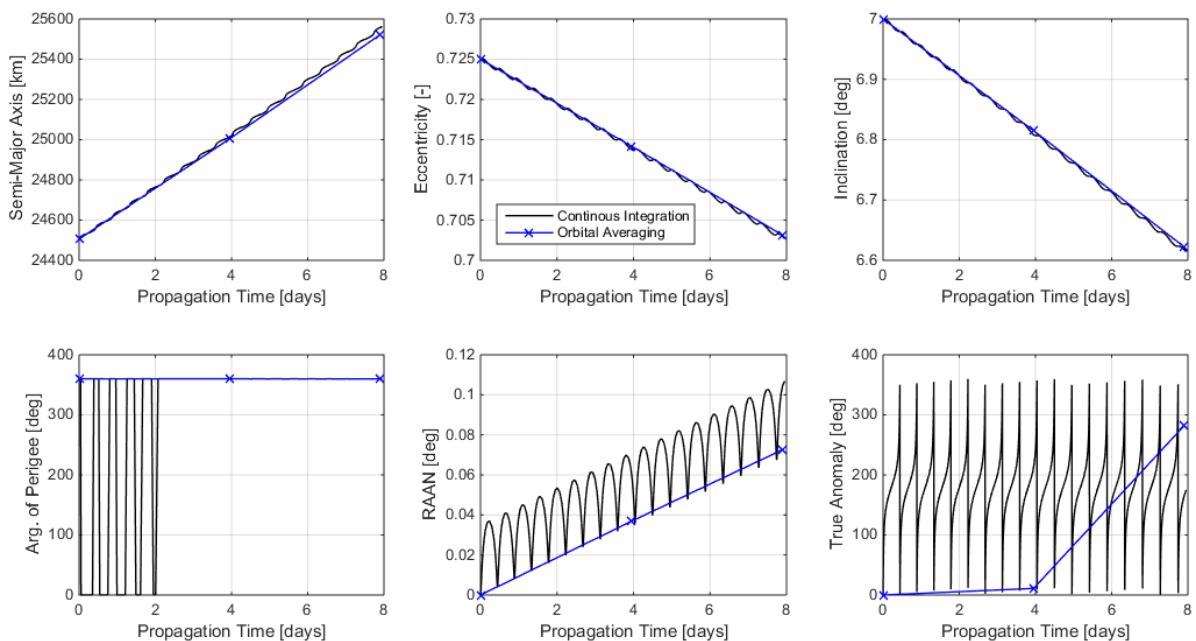
Figure 2.12: Comparison of continuous integration and orbital averaging.

Nonetheless, OA has two drawbacks: the information about the micro-variations of the orbital elements is lost in the process and, more importantly, the propagation of rapidly-changing variables is too inaccurate to be of use in practical applications. For this explanation, let it be assumed that Keplerian elements are used in the propagation. Whereas the elements a, e, i, ω, and Ω vary by negligible amounts within a single low-thrust revolution, the true anomaly θ continuously spans the $[0, 2\pi)$ rad range. It is exactly this rapidly-changing nature that hinders the accuracy of the true anomaly propagation to such extent that the information can be considered lost for practical purposes. This behaviour is shown in Figure 2.12, where the initial GTO orbit from Case A, see section 3.1 was propagated with OA and CI for an out-of-plane thrust profile intended to increase the inclination.

The micro-variations of the slowly-changing elements within each revolution is not of paramount interest when generating a priori optimal solutions because only the overall trend is required to determine when the target orbit is reached. Moreover, many a priori applications do not require accurate information of the satellite's position within the orbit (i.e. the rapidly changing element θ or L). However, this information is critical to the success of other applications such as GEO positioning or rendez-vous missions, rendering the OA method unacceptable. Therefore, HOSTEP is flexible such that the user can choose to employ either CI or OA depending on the situation. The OA option significantly lowers the propagation effort, and hence the optimization load, whereas the CI alternative allows for an accurate propagation of spacecraft final geodetic longitude.

PRACTICAL IMPLEMENTATION

The propagation logic within the evaluated revolution in OA is similar to that of the CI process, see Figure 2.11. The exception is that the revolution is defined by $\theta = 2\pi$ instead of $L = 2\pi$ and the propagation steps are equidistant in true anomaly θ instead of true longitude L. The latter is accomplished by converting the true anomaly propagation step $\Delta\theta = \frac{2\pi}{n_k}$ to a time step, at every epoch, through $\Delta t = \Delta\theta \frac{dt}{d\theta}$. The rate of change of θ for a thrust acceleration input $\boldsymbol{a}_T$ in the RSW reference frame is given by the first two terms in Equation 2.69 [Vallado, 1997, p. 566], where $h = \sqrt{\mu p}$ [Vallado, 1997, p. 108]. Additionally, the contribution of the Earth's attraction is given by the third term in Equation 2.69 [Vallado, 1997, p. 107]. Equation 2.70 is the simplification that was employed by [Boudestijn, 2014] and [Gomez, 2015].

$$\frac{d\theta}{dt} = \frac{1-e^2}{nae}\cos\theta\, a_{r,T} - \frac{1-e^2}{nae}\frac{2+e\cos\theta}{1+e\cos\theta} a_{s,T} + \frac{h}{r^2} \tag{2.69}$$

$$\frac{d\theta}{dt} \approx \frac{na}{r} \tag{2.70}$$

where $n = \sqrt{\frac{\mu}{a^3}}$ is the mean motion of the spacecraft. This difference with the CI method is critical to capture and average the secular trend of the system dynamics. This is because L is also influenced by the variations in ω and Ω and $L = 2\pi$ might therefore not exactly constitute an orbital revolution.

After the EOM have been evaluated in all propagation steps of one discrete revolution, these n_k values of $\dot{\boldsymbol{x}}$ are averaged numerically to yield $\bar{\dot{\boldsymbol{x}}}$. The numerical averaging approach presented in [Kluever, 2010] entails a change of variable in the integration process as follows:

$$\bar{\dot{\boldsymbol{x}}} = \frac{\Delta\boldsymbol{x}}{T_{orb}} = \frac{1}{T_{orb}}\int_{t_{lb}}^{t_{ub}}\frac{d\boldsymbol{x}}{dt}dt = \frac{1}{T_{orb}}\int_{E_{lb}}^{E_{ub}}\frac{d\boldsymbol{x}}{dt}\left(\frac{dE}{dt}\right)^{-1}dE \tag{2.71}$$

where t_{lb}, t_{ub} and E_{lb}, E_{ub} are the lower and upper bounds of the time and eccentric longitude respectively. The strategy in [Kluever, 2010] is to select these bounds to exclude the Earth shadow region, thus disregarding any thrust input during eclipse yet maintaining constant thrust elsewhere. This strategy has been modified in HOSTEP, which integrates over the complete revolution irrespective of eclipses, see Equation 2.71, with thrust acceleration being automatically set to zero if sunlight incidence is below the user-specified threshold.

$$\bar{\dot{\boldsymbol{x}}} = \frac{\Delta\boldsymbol{x}}{T_{orb}} = \frac{1}{T_{orb}}\int_{t_0}^{t_{2\pi}}\frac{d\boldsymbol{x}}{dt}dt = \frac{1}{T_{orb}}\int_{0}^{2\pi}\frac{d\boldsymbol{x}}{dt}\left(\frac{d\theta}{dt}\right)^{-1}d\theta \tag{2.72}$$

This was done because, although the electric engine cannot be operated in the absence of sunlight [Duchemin et al., 2011], there may be other important force model contributions during eclipses, such as third body perturbing forces, that should not be disregarded within the averaging process [Jimenez-Lluva, 2016]. Moreover, the use of true anomaly θ is preferred over eccentric anomaly E for this application because it creates a higher concentration of data points near perigee. Another considerable method adjustment is the calculation of the

orbital period, T_{orb}. The original averaging method analytically computed $T_{orb} = 2\pi\sqrt{\frac{a^3}{\mu}}$ using the semi-major axis, a, at the start of the revolution and assumed that the change in a throughout the revolution is negligible [Kluever, 2010]. Instead, HOSTEP computationally evaluates the sum of Δt increments for the n_k propagation steps in one discrete revolution, thus yielding a more accurate T_{orb}.

HOSTEP numerically approximates the integral $\Delta \boldsymbol{x}$ in Equation 2.72 in one of three alternative methods: a part-wise trapezoidal or Simpson's integration scheme formulated with a constant step-size in true anomaly, $\Delta \boldsymbol{x}_{trap,\theta}$ and $\Delta \boldsymbol{x}_{simp,\theta}$, or a trapezoidal scheme employing a varying step-size in time, $\Delta \boldsymbol{x}_{trap,t}$. Detailed descriptions of these schemes may be found in well-established calculus sources such as [Steward, 2003]. They are defined by the corresponding formulae below, of which the second expressions are the simplified versions implemented in HOSTEP:

$$\Delta \boldsymbol{x}_{trap,\theta} \approx \sum_{i=0}^{n_k-1} \left\{ \frac{\left[\frac{d\boldsymbol{x}}{dt}\frac{dt}{d\theta}\right]_{\theta=\theta_i} + \left[\frac{d\boldsymbol{x}}{dt}\frac{dt}{d\theta}\right]_{\theta=\theta_{i+1}}}{2} \Delta\theta \right\} \tag{2.73}$$

$$\Delta \boldsymbol{x}_{trap,\theta} \approx \frac{\Delta\theta}{2} \left\{ \left[\frac{d\boldsymbol{x}}{dt}\frac{dt}{d\theta}\right]_{\theta=\theta_0} + 2\sum_{i=1}^{n_k-2} \left[\frac{d\boldsymbol{x}}{dt}\frac{dt}{d\theta}\right]_{\theta=\theta_i} + \left[\frac{d\boldsymbol{x}}{dt}\frac{dt}{d\theta}\right]_{\theta=\theta_{n_k}} \right\} \tag{2.74}$$

$$\Delta \boldsymbol{x}_{simp,\theta} \approx \sum_{i=1}^{n_k-1} \left\{ \frac{\left[\frac{d\boldsymbol{x}}{dt}\frac{dt}{d\theta}\right]_{\theta=\theta_{i-1}} + 4\left[\frac{d\boldsymbol{x}}{dt}\frac{dt}{d\theta}\right]_{\theta=\theta_i} + \left[\frac{d\boldsymbol{x}}{dt}\frac{dt}{d\theta}\right]_{\theta=\theta_{i+1}}}{3} \Delta\theta \right\} \tag{2.75}$$

$$\Delta \boldsymbol{x}_{simp,\theta} \approx \frac{\Delta\theta}{3} \left\{ \left[\frac{d\boldsymbol{x}}{dt}\frac{dt}{d\theta}\right]_{\theta=\theta_0} + 4\sum_{i=0}^{\lfloor\frac{2n_k-3}{4}\rfloor} \left[\frac{d\boldsymbol{x}}{dt}\frac{dt}{d\theta}\right]_{\theta=\theta_{2i+1}} + 2\sum_{i=1}^{\lfloor\frac{2n_k-1}{4}\rfloor} \left[\frac{d\boldsymbol{x}}{dt}\frac{dt}{d\theta}\right]_{\theta=\theta_{2i}} + \left[\frac{d\boldsymbol{x}}{dt}\frac{dt}{d\theta}\right]_{\theta=\theta_{n_k}} \right\} \tag{2.76}$$

$$\Delta \boldsymbol{x}_{trap,t} \approx \sum_{i=0}^{n_k-1} \left\{ \frac{\left[\frac{d\boldsymbol{x}}{dt}dt\right]_{t=t_i} + \left[\frac{d\boldsymbol{x}}{dt}dt\right]_{t=t_{i+1}}}{2} \right\} \tag{2.77}$$

$$\Delta \boldsymbol{x}_{trap,t} \approx \frac{1}{2} \left\{ \left[\frac{d\boldsymbol{x}}{dt}dt\right]_{t=t_0} + \sum_{i=1}^{n_k-2} \left\{ \left[\frac{d\boldsymbol{x}}{dt}dt\right]_{t=t_i} + \left[\frac{d\boldsymbol{x}}{dt}dt\right]_{t=t_{i+1}} \right\} + \left[\frac{d\boldsymbol{x}}{dt}dt\right]_{t=t_{nk}} \right\} \tag{2.78}$$

The previous hybrid methodologies in literature only employed the trapezoidal integration scheme [Kluever, 2010; Boudestijn, 2014; Gomez, 2015]. Simpson's scheme was implemented in HOSTEP to evaluate its effect on the accuracy since there is evidence that it is more precise in approximating second degree polynomials in the proximity of turning points [Steward, 2003]. This was deemed to be of particular interest because, since the the orbital elements oscillate per revolution and the integration steps are equidistant in θ or L, there are generally few propagation steps near the apogee for eccentric orbits, which is exactly the turning point of the sinusoid.

The three schemes were tested for the three GTO-GEO optimized trajectories from Case A1 in chapter 3 and the results are presented in Table 2.2 and Table 2.3. The inputs for these trajectory simulation are similar to those shown in Table 3.2, with the computational mode set to simulation instead of optimization and averaging strategy varied according to the scheme being tested. Moreover, the design vectors specified for the three trajectories include their corresponding TOF from Table 3.3 and co-states from Table 3.5.

The results show that there is no significant difference between the trapezoidal and Simpson's integration schemes, but there is a significant improvement when using time as the averaging variable instead of true anomaly in the trapezoidal scheme. This can be safely stated, not only because the absolute OA error decreases for almost all elements, but more importantly because the latter scheme exhibits zero error for the mass change. Since the mass flow is a linear EOM with respect to time, there should be no error upon averaging it with a trapezoidal scheme. These results indicate that the calculation of $\frac{d\theta}{dt}$ is not as accurate as expected, even though both Equation 2.69 and Equation 2.70 were tested and yielded no significant difference. Therefore, the simulations and optimizations presented in the upcoming chapters employ the trapezoidal integration scheme with respect to time.

Table 2.2: Comparison of the OA errors for the three Case A1 optimal trajectories using the trapezoidal and Simpson's scheme with true anomaly as averaging variable.

State variable	Case A1 Solution #1		Case A1 Solution #2		Case A1 Solution #3	
	Trapezoidal OA error	Simpson's OA error	Trapezoidal OA error	Simpson's OA error	Trapezoidal OA error	Simpson's OA error
Semi-major axis a [km]	-37.144	-37.237	43.435	43.242	-41.709	-41.808
Eccentricity e [-]	0.014	0.014	0.014	0.014	0.014	0.014
Inclination i [deg]	0.039	0.039	0.206	0.206	0.142	0.1423
RAAN Ω [deg]	-146.905	-146.884	-14.390	-14.390	-76.259	-76.2632
Arg. of perigee ω [deg]	164.044	164.030	-87.017	-87.022	103.934	103.9437
Total mass m [kg]	-0.012	-0.012	-0.009	-0.009	-0.012	-0.012

Table 2.3: Comparison of the OA errors for the three Case A1 optimal trajectories using the trapezoidal scheme with true anomaly and time as averaging variables.

State variable	Case A1 Solution #1		Case A1 Solution #2		Case A1 Solution #3	
	Tr. anom. OA error	Time OA error	Tr. anom. OA error	Time OA error	Tr. anom. OA error	Time OA error
Semi-major axis a [km]	-37.144	-72.535	43.435	30.761	-41.709	-24.502
Eccentricity e [-]	0.014	0.011	0.014	0.011	0.014	0.011
Inclination i [deg]	0.039	0.034	0.206	0.207	0.142	0.134
RAAN Ω [deg]	-146.905	-126.505	-14.390	-6.797	-76.259	-66.778
Arg. of perigee ω [deg]	164.044	95.590	-87.017	-138.185	103.934	46.402
Total mass m [kg]	-0.012	0.000	-0.009	0.000	-0.012	0.000

2.6. Verification Activities

This section describes the Verification and Validation (V&V) strategy and activities. The primary objective of the V&V activities was to avoid the costs of potential troubleshooting in the later development stages. It is important to notice that the cost of fixing software defects increases exponentially with the project progress when it is detected. This is shown in Figure 2.13 [McConnell, 1996]. Whereas verification is generally attributed
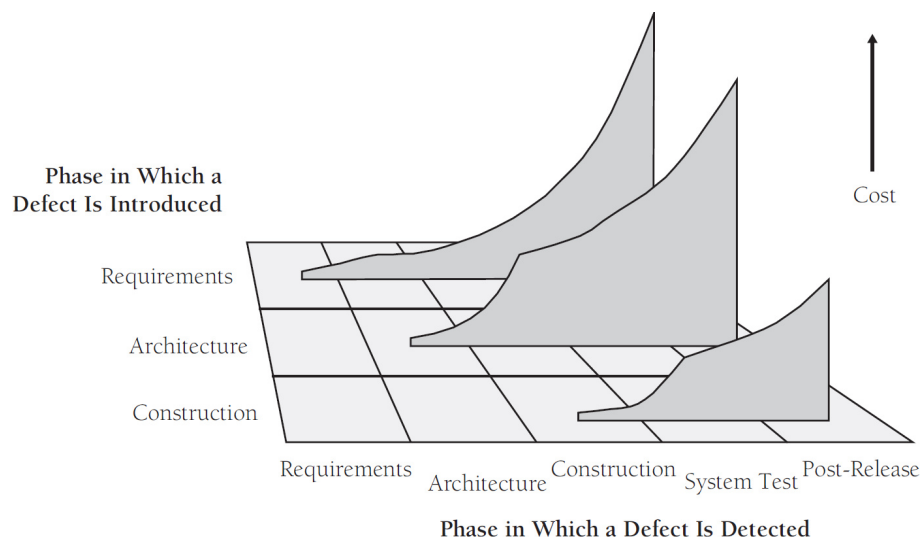
Figure 2.13: Defect fixing costs as a function of introduction and detection phase [McConnell, 1996].

to the process, "Am I building the product right?", validation is related to requirements, "Am I building the right product?". V&V can be approached through: test, analysis, demonstration, inspection, and review. Tests are considered ideal because they are most objective, but often require most resources. Due to this inherent trade-off, it is desirable to employ other methods as much as possible [Autrán-Cerqueira, 2016].

The verification activities of large software projects include [Autrán-Cerqueira, 2016]:

- Verification of requirements: ensure compliance with the SMART criterion (specific, measurable, achievable, relevant, and time-bound), ensure specification about when each requirement will be validated, and ensure traceability between each requirement and its nature.

- Verification of design: ensure that it implements all requirements, ensure that it complies with the design standards of GMV, and ensure traceability between the requirements and the design architecture.

- Verification of code:

    - Traceability: ensure that all files can be traced to design components.

    - Coding rules: ensure compliance with existing standard to prevent coding errors and enhance future maintainability.

    - Dynamic analysis: detect defects that are hard to detect or non-repeatable.

    - Unit testing: ensure nominal execution in representative environments, evaluate robustness to unexpected situations, and ensure coverage of all loops and conditional statements.

    - Code inspection: ensure correct and efficient implementation while enhancing cross-learning.

- Verification of integration: perform representative hardware environment tests, evaluate whether results are as expected, and justify discrepancies.

- Verification of documentation: define who is responsible per activity, what the deliverables are, when these should be reviewed and submitted, what the general output is, and what the specific outputs are.

As the reader may expect, the limited constraints of this thesis did not allow to scrutinize these activities as one should do in large scale projects. Nonetheless, this thesis project aims to provide a research feasibility study rather than critical software development, hence lessening the need for verification and validation activities. In fact, the last activity in the list above is beyond the scope of this thesis project.

Requirement verification was performed in consultation with the project sponsor. High-level requirements were assessed and prioritized in the early stages of the project to produce the project objectives list in section 1.5. Low level requirements were assessed throughout the code development process. For example, the interface requirements that allow the validation tools PROPAG and EVENTS to automatically import HOSTEP's output manoeuvre and orbit files respectively, were evaluated shortly before the corresponding code implementation to save by avoiding excessive analysis or the less critical requirements.

Design verification was initiated in the earliest stage because an initial solid foundation for the software architecture is essential to meet the requirements effectively and efficiently. However, design verification was kept an iterative process that lasted until the mid-term review, because the thorough understanding of the hybrid method gained gradually over time allowed for perfecting the architecture and work-flow of HOSTEP. Nonetheless, the project sponsor's insightful input of previous software projects was very valuable in the early stage of this process. Further details about HOSTEP architecture and work-flow may be found in Appendix B.

Code verification was conducted since the start of the code development process to alleviate the debugging effort at the end. A considerable effort was made prior to the construction stage in order to understand and prioritize GMV's programming rules as well as to identify tips and guidelines such as the "7 complexity rule of thumb" – maximum 7 public subroutines per module, 7 input/output variables per subroutine, etc. The unitary test campaign was focused on several subroutines, trading-off the easiness of the unit test implementations and the criticality of the subroutines with respect to HOSTEP's overall performance. Dynamic analysis was applied to automate executions over night and helped identify rare errors arising from bad solutions that sometimes halted the optimization. Lastly, code inspection was carried out throughout the entire software development process with the aid of the software editor debugger, which streamlined the decision coverage and statement inspection, as well as automated plot generation within the GUI, which allowed for quickly identifying anomalies in the trajectories.

2.7. Validation Activities

The HOSTEP validation campaign aims to evaluate its core functionalities and achieve the project objectives as accurately as possible. The test cases focus on validating the accuracy of the propagator and the eclipse simulator. The propagation process is validated in comparison with PROPAG, and the eclipses are validated in

comparison with EVENTS, both of which are commercial and thoroughly validated elements available within GMV's *focussuite* ® toolbox. To enhance the automation of these validation tests, HOSTEP's GUI features a post-processing option to output a manoeuvre and an orbit file that can be directly read by PROPAG and EVENTS respectively – further details about these options can be found in Appendix B. Thus, the simulations of PROPAG and EVENTS correspond to the same thrust profile and trajectory of HOSTEP. This architecture has eased the maintenance of these validation tests throughout the code development process and can be continued in future developments of HOSTEP.

2.7.1. TESTS A1-A3: PROPAGATOR VALIDATION

The propagator is validated in three different test cases: tangential, out-of-plane, and radial thrust profiles, which are illustrated in Figure 2.14. These profiles are accomplished through hard-coding the thrust steering angles when the user selects these specific thrust profiles in the GUI – the corresponding values may be found Table B.1. It is worth recalling that the integration steps within every revolution are equidistant in true anomaly or true longitude, thus leading to a higher concentration of nodes near perigee in Figure 2.14. For this validation, all orbital perturbations were disregarded, including eclipses, both in HOSTEP and PROPAG. The initial orbit was chosen to be a GTO because it combines a high eccentricity with a slight inclination that should provide a better insight of the simulator behaviour. The initial orbit is taken to be a slightly inclined GTO: $a = 24505.9$ km, $e = 0.725$, $i = 7.0$ deg, $\omega = 0.0$ deg, $\Omega = 0.0$ deg, and $\theta = 0.0$ deg [Geffroy and Epenoy, 1997]. The spacecraft parameters used are: $T = 350.0$ mN, and $I_{sp} = 2000.0$ s, $m = 2000.0$ kg. The complete list of inputs and GUI options for these test cases may be found in Appendix C.
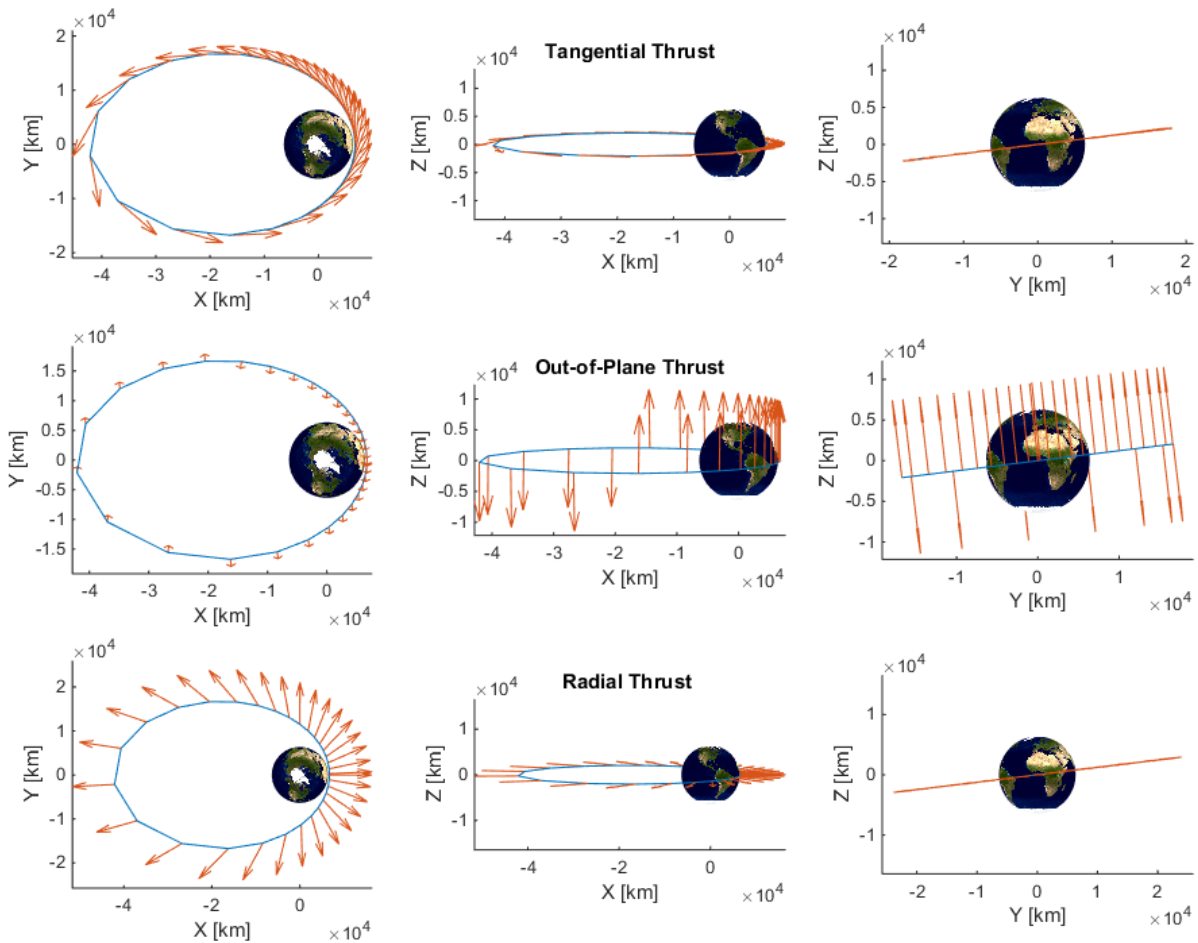
Figure 2.14: Visualization of the validation thrust profiles: tangential (top), out-of-plane (middle), and radial (bottom).

The validation results for these test cases are shown in Figure 2.15 to Figure 2.17. These plots present PROPAG's results, HOSTEP's results, and the error of HOSTEP with respect to PROPAG, using CI and OA. The CI simulation employs 30 propagation steps per revolution whereas the OA simulation was repeated for 30, 40, and 50

propagation steps per revolution and OA steps of 3.0, 4.0, and 5.0 days. The orbital elements studied are the semi-major axis, eccentricity, and inclination because these provide a more useful and intuitive insight.

TANGENTIAL THRUSTING: TEST A1

The most prominent OA error can be observed in Figure 2.15 for the semi-major axis, which is to be expected and the highest acceleration component is closer to the tangential direction. As expected, increasing the OA step-size has a more detrimental effect on the accuracy of the OA approximation because over time, as the orbital elements vary further, the averaged (constant) derivative becomes less realistic. Moreover, increasing the number of integration steps, n_k, enhances the OA accuracy due to the nature of the trapezoidal scheme. Moreover, the oscillating nature of the OA error is expected because the CI values exhibit a short term oscillation whereas the AO propagation has only a secular variation. This is more prominent for eccentricity because the OA-CI discrepancy is lower, whereas for the semi-major axis, the oscillation is less significant in comparison with the OA error itself. The CI error observed for a and e is acceptable for a priori optimization. In the case of inclination, the errors in all curves are too small and can be assumed to be numeric in nature.
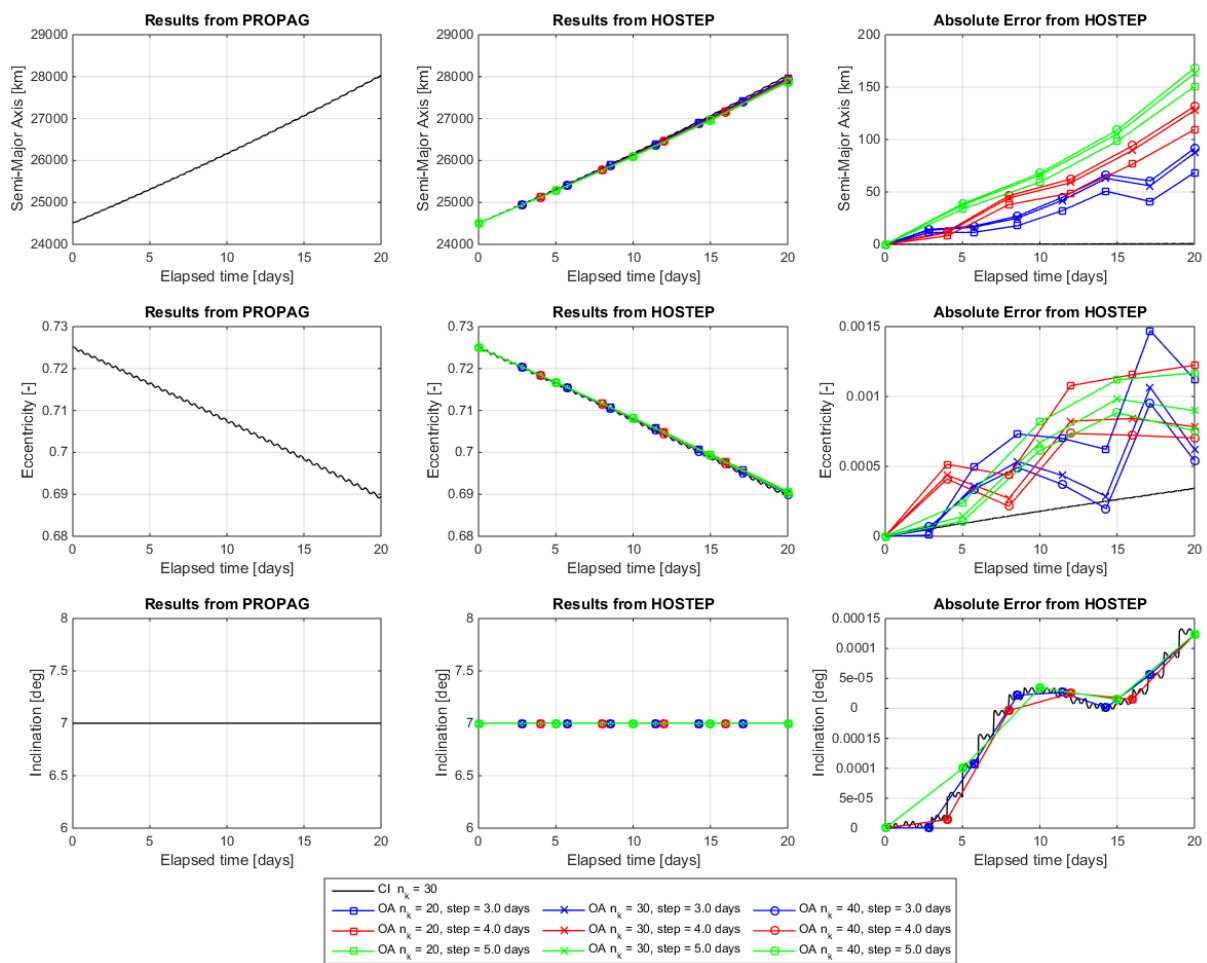
Figure 2.15: Test A1: tangential thrust propagation comparison between PROPAG and HOSTEP for a, e, and i using CI and OA.
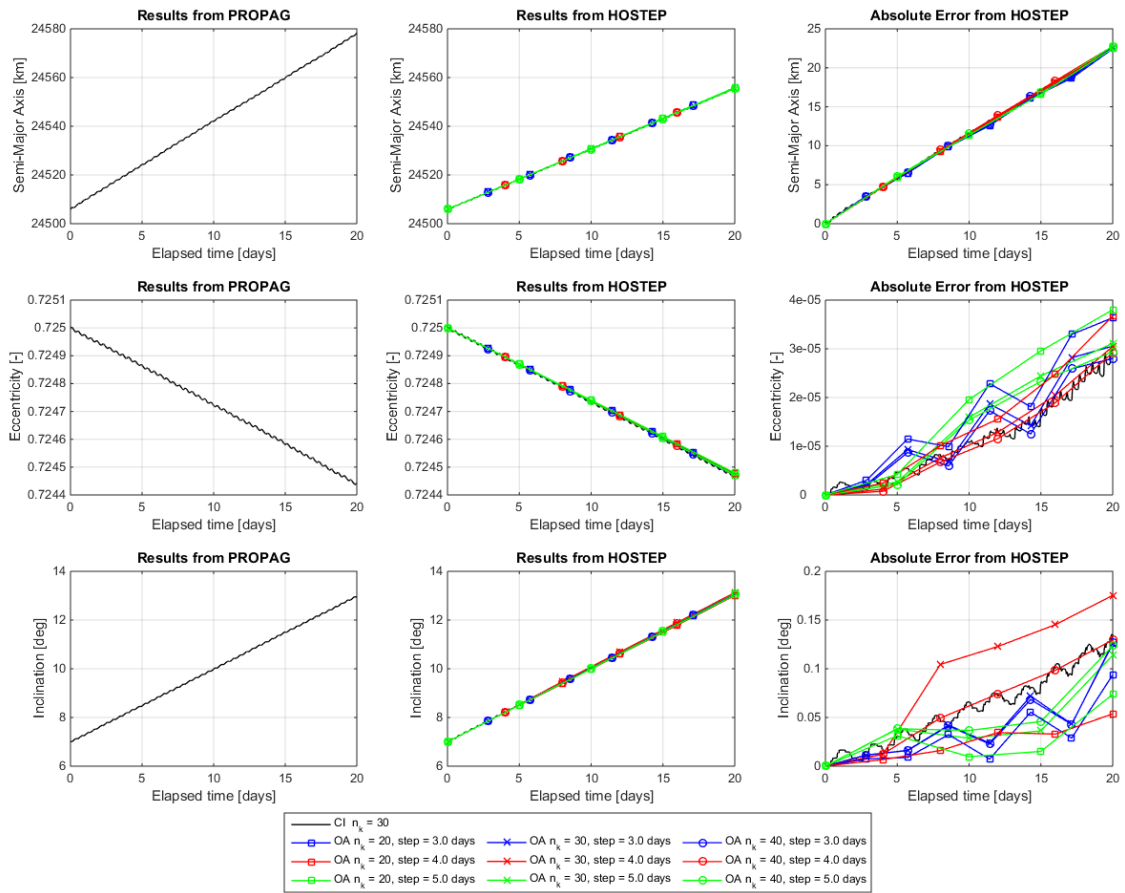
Figure 2.16: Test A2: out-of-plane thrusting comparison between PROPAG and HOSTEP for *a*, *e*, and *i* using CI and OA.
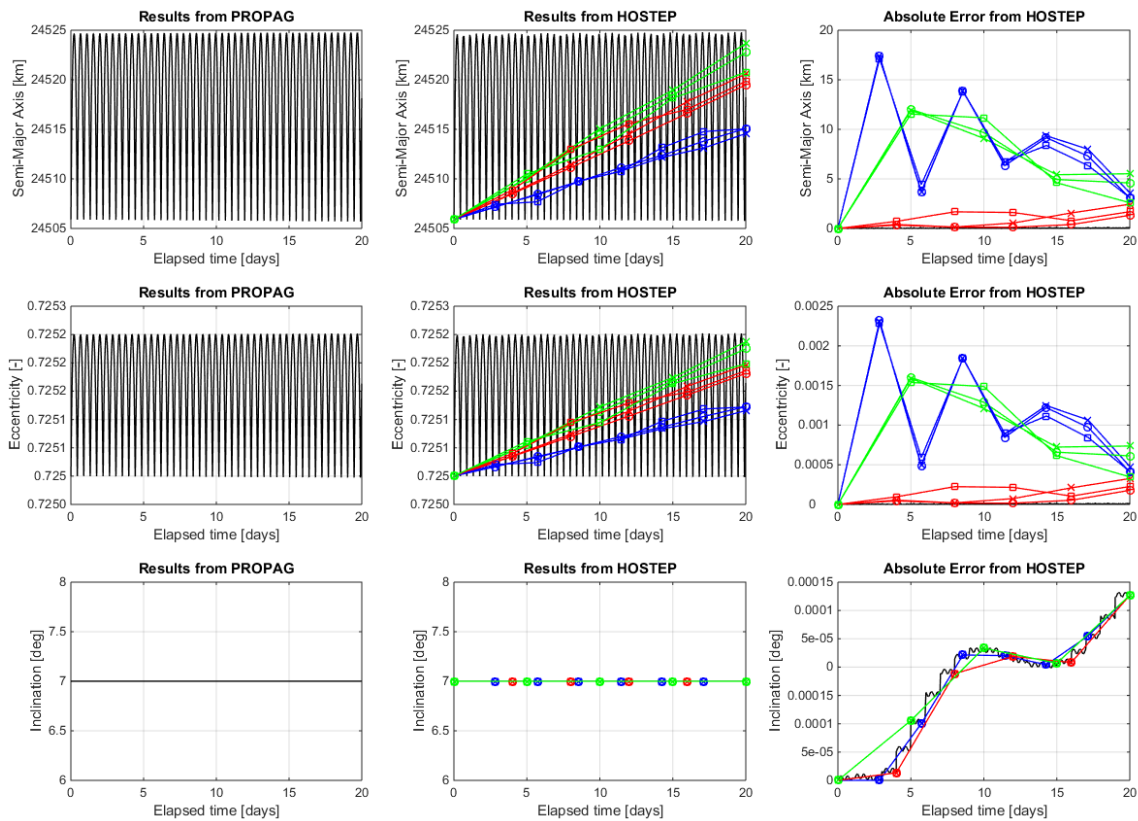
Figure 2.17: Test A3: radial thrust propagation comparison between PROPAG and HOSTEP for *a*, *e*, and *i* using CI and OA.

OUT-OF-PLANE THRUSTING: TEST A2

In the inclination change scenario, Figure 2.16, the error of the CI propagation is so prominent for the semi-major axis that it veils the error of the OA approximations. This is because, whereas PROPAG directly employs numerical integration to compute the state in cartesian component, HOSTEP employs the MEE formulation derived from Gauss' form of the Lagrange planetary EOM, Equation 2.5 to Equation 2.10. The author believes that the assumptions in the original derivation of these EOM cause a discrepancy for prolonged out-of-plane manoeuvres. In essence, the formulation assumes that out-of-plane thrust accelerations, u_r, do not influence the semi-latus rectum p, since the effect of $u_r$ is simply not captured in the corresponding EOM, Equation 2.5. In practice, however, an infinitesimal ΔV change perfectly perpendicular to the velocity vector does vary the magnitude of the velocity vector, thereby influencing the semi-major axis. Therefore, the semi-major axis deviation in Figure 2.16 is to be expected, but the author deems this acceptable since the underlying OM have been thoroughly employed in previous trustworthy studies [Betts, 2010; Falck and Dankanich, 2012; Boudestijn, 2014; Gomez, 2015]. Moreover, the author believes that the CI error in eccentricity and inclination are both related to the deviation in a and the limitations of the underlying EOM. Hence, this test was repeated using CI with 1000 integration steps per revolution, which resulted in small changes in HOSTEP's simulation yet significant alterations in PROPAG's results; the error in e and i vanished, with the error in a decreasing from 22.64 km to 0.50 km. The author thus concludes that the CI deviation is caused by the EOM limitations and deems this acceptable for a priori optimization purposes. Regarding the OA results, the eccentricity error exhibits the expected pattern that a lower number of integration steps n_k yields a larger deviation in all OA cases, but this pattern does not hold for the inclination error. The effect of the OA step on the error is not conclusive for this test as there is no noticeable pattern. Interestingly enough, the combination of $n_k = 40$ and a 4.0-day OA step-size yields the smallest e and i error.

RADIAL THRUSTING: TEST A3

The CI error in Figure 2.17 is negligible for the semi-major axis and eccentricity, and can be assumed to be of numeric nature for the inclination. Similarly, the OA deviation in inclination can be assumed to be caused by numerical noise. Interestingly enough, the OA approximations show an identical error pattern for a and e. The oscillating trend of the OA error, most noticeable for the blue data points, is thought to stem from the oscillating nature of the orbital elements themselves; because the OA data points remain within the oscillation amplitude of the high frequency sinusoidal CI curve, a small epoch error in the OA data points may lead to a large value error. This effect may be caused by approximation errors in the data processing process and are thus deemed acceptable. Nonetheless, the OA results show a secular increase over time that causes the OA approximation to exceed the oscillation amplitude in larger propagation periods. However, the author deems this secular error acceptable in comparison with the errors of the tangential thrust test case. Again, the combination of $n_k = 40$ and a 4.0-day OA step-size again yields the smallest a and e error and it therefore recommended. Hence, the latter combination is employed for the result cases in chapter 3 that employ the OA technique.

2.7.2. TEST B1: ECLIPSE SIMULATION VALIDATION

HOSTEP employs an eclipse simulator that was readily available and validated at GMV. The working principle of this tool is based on well established approaches, see subsection 2.3.1. Although the author trusts that the simulator has been readily validated already, the eclipse simulation of HOSTEP has been validated to ensure correct use and integration of this tool. The results of HOSTEP are thus compared to the results of EVENTS, one of the commercial tools developed by GMV that can simulate eclipses among other possibilities. To do so, HOSTEP outputs a trajectory description file that can be automatically read and evaluated by EVENTS. Additionally, HOSTEP outputs a summary file, which can include either thrusting or coasting arcs, and the dates corresponding to the eclipses are validated in comparison with the eclipses dates generated by EVENTS, see Table 2.4. The initial conditions and design vector employed for this validation test are similar to those from the LEO-GEO trajectory in Case C, see section 3.4. The input settings and the input co-states are shown in Appendix C. The only difference is that the HOSTEP simulation for this test employs 1000 integration steps per revolution, instead of the regular 30, to capture the eclipse start and end dates with greater accuracy.

The small discrepancies in the dates of Table 2.4 arise from the differences in computational logic between the two software tools. Whereas EVENTS employs a constant time step-size of 100 s for this simulation, HOSTEP uses a discrete number of integration steps per revolution in HOSTEP equidistant in true longitude. Hence, the results of HOSTEP have been visually inspected to confirm that every in- and out- epoch of EVENTS lie between two integration nodes of HOSTEP, with one of them corresponding to the in- or out- epochs of HOSTEP.

Table 2.4: Validation of eclipse dates for the trajectory Test B1.

HOSTEP epoch in	HOSTEP epoch out	EVENTS epoch in	EVENTS epoch out
2000/01/01-12:08:47.854	2000/01/01-12:44:33.825	2000/01/01-12:08:42.924	2000/01/01-12:44:38.600
2000/01/01-13:44:26.184	2000/01/01-14:20:13.527	2000/01/01-13:44:23.034	2000/01/01-14:20:18.645
2000/01/01-15:20:06.821	2000/01/01-15:55:55.538	2000/01/01-15:20:05.452	2000/01/01-15:56:00.999
2000/01/01-16:55:55.514	2000/01/01-17:31:45.608	2000/01/01-16:55:50.182	2000/01/01-17:31:45.668
2000/01/01-18:31:40.778	2000/01/01-19:07:32.249	2000/01/01-18:31:37.229	2000/01/01-19:07:32.655
⋮	⋮	⋮	⋮
2000/07/02-07:23:43.887	2000/07/02-07:44:06.952	2000/07/02-07:23:14.671	2000/07/02-07:44:24.378
2000/07/02-20:44:57.467	2000/07/02-21:03:10.021	2000/07/02-20:44:25.518	2000/07/02-21:03:30.223
2000/07/03-10:15:02.391	2000/07/03-10:31:01.909	2000/07/03-10:14:38.872	2000/07/03-10:31:15.703
2000/07/03-23:55:02.715	2000/07/04-00:07:09.644	2000/07/03-23:54:16.361	2000/07/04-00:07:49.563
2000/07/04-13:44:26.130	2000/07/04-13:52:35.740	2000/07/04-13:43:51.233	2000/07/04-13:53:10.106

However, it must be noted that the eclipse from HOSTEP is always shorter than that of EVENTS, and the author recommends adjusting HOSTEP's logic to extend the simulated shadow arc to the subsequent integration step to be conservative in the future in case a higher accuracy is required of HOSTEP. Nonetheless, the worst case for an $n_k = 30$ propagation would be that two nodes are fully shadowed, meaning that the thrust contribution over $2/300 = 5\%$ of the revolution should have been neglected – since these nodes are equidistant in true longitude for CI – which is deemed acceptable for a priori trajectory optimization.

As a sanity check, the eclipse duration is verified at the initial LEO through simplified analysis. A cylindrical shadow model is assumed such that the line crossing the start- and end-points of the umbra arc equals the Earth's diameter. Therefore, the eclipse arc half-angle ϕ can be found through $\sin \phi = \frac{R_E}{R_E + H}$, with R_E and H being the Earth's radius and orbit altitude respectively. The ratio $2\phi : 2\pi$ thus equals the ratio $T_{eclipse} : T_{orb}$, with $T_{orb} = 2\pi \sqrt{\frac{a^3}{\mu}}$ being the orbital period. At the initial altitude of 550 km, $\phi = 1.17$ rad and $T_{orb} = 95.65$ min. This yields $T_{eclipse} = 35.61$ min, which is consistent with the first eclipse cycles in the LEO-GEO transfer.

2.7.3. Tests C1-C2: Optimizer Validation

The combination of HOSTEP's simulation and optimization processes is validated in comparison to the analytical solution developed in [Edelbaum, 1961]. This analytical solution defines the optimal ΔV required for a low-thrust transfer between two nearly circular orbits with different inclinations:

$$\Delta V = \sqrt{V_1^2 - 2V_1 V_2 \cos\left(\frac{\pi}{2}\Delta i\right) + V_2^2} \tag{2.79}$$

where V_1 and V_2 are the initial and final circular velocities, respectively, and Δi denotes the inclination change. The resulting propellant mass corresponding to this ΔV can be calculated through Tsiolkovki's equation:

$$\Delta V = g_0 I_{sp} \ln\left(\frac{m_0}{m_0 - m_{prop}}\right) \tag{2.80}$$

where m_f and m_0 are the initial and final spacecraft mass, respectively, m_{prop} is the propellant mass, g_0 is the sea-level gravitational acceleration, and I_{sp} is the specific impulse. Lastly, the TOF can be computed by dividing the propellant mass m_{prop} by the mass flow rate, which is calculated in Equation 2.26.

Two circular transfers are optimized to validate HOSTEP with respect to the analytical optimal limit. Test C1 features a co-planar transfer from $a_0 = 7000.0$ km to $a_t = 42000.0$ km and Test C2 optimizes a non-co-planar transfer from $a_0 = 7000.0$ km to $a_t = 9000.0$ km with an inclination change $\Delta i = 3.0$. The first test scenario was specifically chosen because it was also optimized in [Gebbett, 2014] using a direct optimization method. Eclipses and perturbations are disregarded for this optimization because the analytical solution from Edelbaum and the results from [Gebbett, 2014] assumed continuous thrust. The inputs for Test C1 are shown in Table 2.5, and the only inputs that are adjusted for Test C2 are the target elements highlighted in blue. Test C2 employed $a_t = 9000.0$ km, $i_t = 0.05$ deg, and $(t_f)_{ub} = 4.0$ days.

Five DE repetitions were executed for each test, all of them employing Continuous Integration. The upper

boundary of the TOF was specifically set close to the analytical solution to aid the DE optimizer approach the optimum as closely as possible within the specified maximum number of iterations. Moreover, the upper boundary of the final orbit error was more constrained than the recommended values previously shown in Table 2.1 to refine the solution with better accuracy for these tests. The best solution for Test C1 and Test C2 is shown in Table 2.6, and their respective convergence is illustrated in Figure 2.18 and Figure 2.19.

Table 2.5: Inputs for the Case C1 trajectory.

Comp. mode	Optimization	DE mode	Random	a_t [km]	42000.0 *	$(\epsilon_a)_{ub}$ [km]	10.0
Var. thrust	Off	DV source	n/a	e_t [-]	0.001	$(\epsilon_e)_{ub}$ [-]	0.001
Long. target.	Off	DE_{rep} [-]	5	i_t [deg]	0.005 †	$(\epsilon_i)_{ub}$ [deg]	0.01
N_{arcs} [-]	1	N_{iter} [-]	1000	Ω_t [deg]	1.0×10^{-12}	$(\epsilon_\Omega)_{ub}$ [deg]	1.0
m_0 [kg]	300.0	N_P [-]	$10D$	ω_t [deg]	1.0×10^{-12}	$(\epsilon_\omega)_{ub}$ [deg]	1.0
T [mN]	1000.0	C_F [-]	0.6	Λ_t [deg]	n/a	$(\epsilon_\Lambda)_{ub}$ [deg]	n/a
I_{sp} [s]	3100.0	C_R [-]	0.8			W_t [-]	0.1
n_k [-]	40.0	$(t_f)_{ub}$ [day]	15.0 ‡	a_0 [km]	7000.0	W_a [-]	1.0
Propag. scheme	CI	$(t_f)_{lb}$ [day]	0.0	e_0 [-]	0.001	W_e [-]	1.0
OA_{step} [day]	n/a	λ_{ub} [-]	1.0×10^4	i_0 [deg]	0.005	W_i [-]	1.0
Avg. scheme	Trapez.	λ_{lb} [-]	-1.0×10^4	Ω_0 [deg]	1.0×10^{-12}	W_Ω [-]	0.0
Avg. variable	Time			ω_0 [deg]	1.0×10^{-12}	W_ω [-]	0.0
Eclipse thr. [%]	Off	Launch		θ_0 [deg]	1.0×10^{-12}	W_m [-]	n/a
J_2 perturb. [-]	Off	date [UTC]	n/a			W_Λ [-]	n/a

* The target semi-major axis value is adjusted to 9000 km for Test C2.
† The target inclination value is adjusted to 0.05 deg for Test C2.
‡ The allowed maximum TOF is adjusted to 4.0 days for Test C2.

Table 2.6: Validation of the circular orbit transfers Test C1 and C2.

	Test C1		Test C2	
	Time-of-flight t_f [days]	**Propellant mass** m_{prop} [kg]	**Time-of-flight** t_f [days]	**Propellant mass** m_{prop} [kg]
HOSTEP	14.45	41.37	3.76	10.68
[Gebbett, 2014]	14.60	41.48	n/a	n/a
Edelbaum	14.42	40.98	3.62	10.32
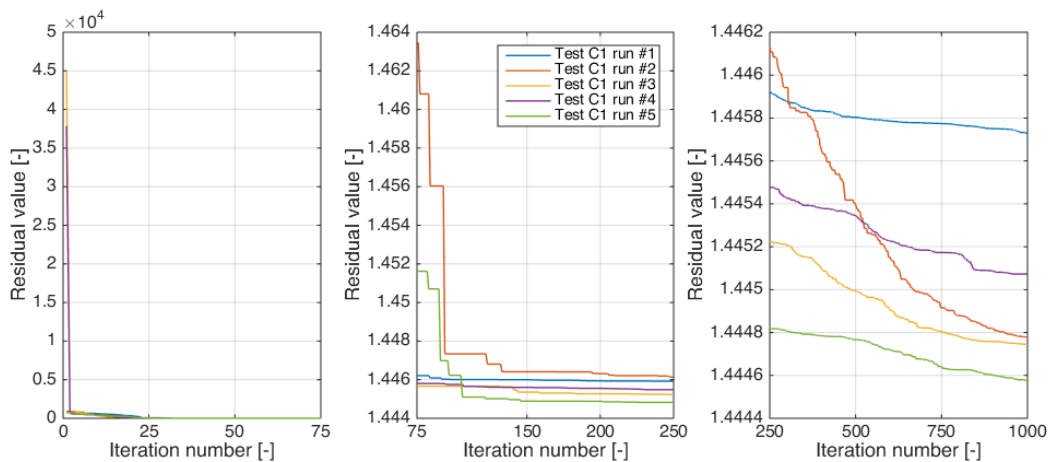
Figure 2.18: Convergence of the 5 DE executions for Test C1, zoomed-in for three different ranges of iteration numbers.

Table 2.6 shows that HOSTEP has a high degree of accuracy in comparison with the analytical solution, and that it performs better than the optimization presented in [Gebbett, 2014]. Figure 2.18 and Figure 2.19 reveal an adequate convergence for all each executions. Test C1 employed a computational time of 1 hr 26 min, whereas Test C2 required 2 hr 41 min. Assuming an equal load distribution this yields respectively 17.2 min and
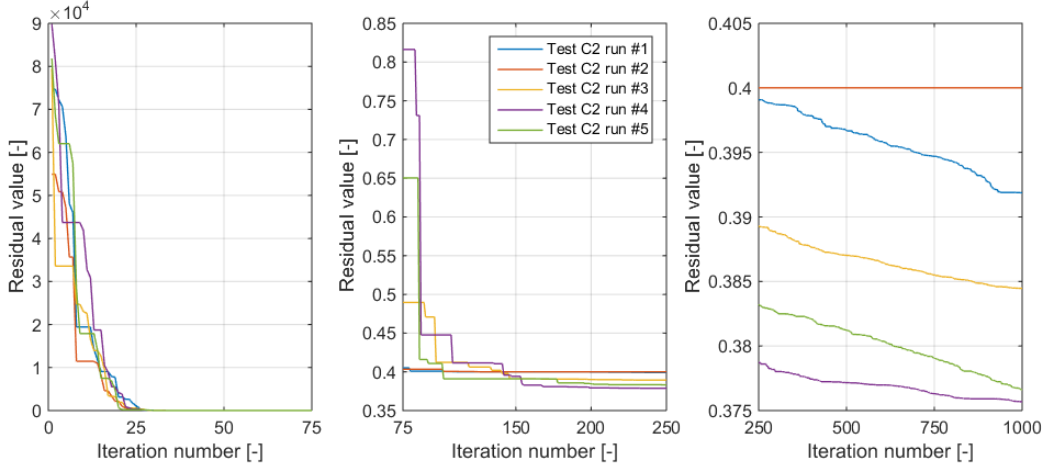
Figure 2.19: Convergence of the 5 DE executions for Test C2, zoomed-in for three different ranges of iteration numbers.

32.2 min for every complete DE repetition, 1.032 s and 1.932 s per every DE iteration, and 9.38 ms and 17.56 ms per simulation evaluation (since every generation has a population size of $N_P = 10D = 110$). The author recommends implementing more sophisticated stopping criteria or a superior DE algorithm altogether – see further details in subsection 4.4.1 – because the graphs above show that the residual improvement in the last 500 iterations is sometimes not worth the corresponding computational time. Nonetheless, this is acceptable for the scope of this thesis because the computational time is not a primary requirement.

2.7.4. TESTS D1: J2 PERTURBATION VALIDATION

The J$_2$ perturbing accelerations implemented in HOSTEP are validated through comparison with the analytical secular drift. The same inputs from Test A1 are used to simulate the first 20-days of the GTO-GEO trajectory, with the thrust set to zero and the J$_2$ perturbation activated. As explained in well established books like [Vallado, 1997; Kluever, 2010], the Keplerian elements a, e, and i exhibit oscillations only, whereas ω and Ω experience a secular drift as a consequence of the J$_2$ effect. This secular drift can be calculated as follows,

$$\dot{\overline{\Omega}}_{J_2} = \frac{3nR_E^2 J_2}{4a^2\left(1-e^2\right)^2}\left(4 - 5\sin^2 i\right) \tag{2.81}$$

$$\dot{\overline{\omega}}_{J_2} = \frac{-3nR_E^2 J_2}{2a^2\left(1-e^2\right)^2}\cos i \tag{2.82}$$

where $n = \sqrt{\frac{\mu}{a^3}}$ is the mean motion of the spacecraft, $R_E = 6378.137$ km is the Earth's radius, and J$_2 = 1.0826269\times 10^{-3}$ is the dimensionless constant corresponding to the second order Earth zonal harmonic perturbation. The output of the previous equations is [rad·s^{-1}]. The observed secular drift from HOSTEP's simulation over 20 days is compared with the analytical solution in Table 2.7.

Table 2.7: Comparison of the secular drift in Ω and ω over 20 days for HOSTEP's propagation and the analytical solution.

	$\Delta\Omega_{J_2}$ [deg]	$\Delta\omega_{J_2}$ [deg]
HOSTEP	-7.956	15.737
Analytical solution	-7.906	15.635

The error between the observed and calculated drift for this period of 20 days is 0.05 and 0.1 deg for Ω and ω respectively. This is deemed acceptable for a priori optimization because a linear accumulation of this error would remain below the requirement from Table 2.1 for a typical 137 days GTO-GEO trajectory.

3

RESULTS

"The important thing is not to stop questioning." – Albert Einstein.

This chapter presents the results of HOSTEP for several different test cases. These test cases are described below in Table 3.1, together with the reference data from literature that is used as comparison. Case A, B, and C investigate the GTO-GEO transfer because it is the most frequent trajectory for satellites with all-electric propulsion [Duchemin et al., 2011]. Case A optimizes for minimum-TOF, both with and without the J_2 perturbation, and compares HOSTEP's optimal solutions with those of the reference indirect method. Case B performs propellant-minimization using the coasting mechanism and reproduces the Pareto front of the propellant mass against TOF that is available from the reference indirect method. Case C investigates the effect of targeting the final geodetic longitude in combination with propellant minimization, which was neither attempted in the reference indirect nor hybrid methods. Lastly, Case D evaluates the LEO-GEO trajectory to compare HOSTEP's results with the solutions of the reference hybrid methodologies.

Table 3.1: Description of the different results cases presented.

Test case	Transfer Description	Comparison data
Case A	Minimum-TOF GTO-GEO	[Montealegre-Avila, 2015; Sanchez and Campa, 2014; Geffroy and Epenoy, 1997]
Case B	Minimum-propellant GTO-GEO	[Sanchez and Campa, 2014]
Case C	GTO-GEO with longitude targeting	
Case D	Minimum-TOF LEO-GEO	[Boudestijn, 2014; Kluever, 2010]

3.1. CASE A: MINIMUM-TIME GTO-GEO TRAJECTORY

The GTO-GEO transfer is among the most popular scenarios for commercial applications because the majority of communications satellites are placed at GEO orbits. The economic incentive for minimum-time optimization lies in reaching the target orbit as quickly as possible to reduce the Launch and Early Operations Phase (LEOP) costs. Moreover, it helps ensure that the system can deliver its services on time, as telecom operators generally have very tight schedule constraints before loosing the market opportunity.

The solution of HOSTEP for this trajectory is compared with the indirect method employed in [Geffroy and Epenoy, 1997; Sanchez and Campa, 2014; Montealegre-Avila, 2015]. Since the three studies present a reference solution that does not include any orbital perturbations beyond the thrust of the engine, the trajectory is first optimized with HOSTEP in unperturbed conditions. Additionally, the trajectory is also optimized with the J_2 perturbation since this case was documented in [Montealegre-Avila, 2015]. It should be clarified that neither sub-case incorporates Earth shadow regions. Although Geffroy and Epenoy [1997] also presented a solution including eclipses, the author deemed it inefficient to reproduce this solution because it constitutes a worst case scenario, thus providing little practical insight at the expense of long simulation times. This is because the chosen initial conditions lead to shadow regions initially at apogee, yielding a TOF of 240 days, 628 revolutions, and a propellant mass of 370 kg.

3.1.1. CASE A1: UNPERTURBED TRAJECTORY

Four optimization executions are performed for this scenario to evaluate the effect of the input optimization parameters. The input parameters for the first, and less optimal, solution are shown in Table 3.2, with the marked fields being the parameters that are adjusted for the subsequent executions. Every trial is optimized using a single co-state arc, meaning that the co-state vector $\boldsymbol{\lambda}$ is defined at two nodes, $t = 0$ and $t = t_f$, yielding 11 optimization parameters together with the TOF itself. The CI integration option is selected with 40 integration steps per revolution and an OA_{step} of 4.0 days is selected to compare the optimal trajectory simulation between the two propagation methods. Since the first execution only yielded a near-optimal solution, the marked values were adjusted in order to refine the optimized trajectory. The four optimization results are compared with the reference optima from indirect methods in Table 3.3.

Table 3.2: Inputs for the Case A1 executions.

Comp. mode	Optimization	DE mode	Random	a_t [km]	42165.0	$(\epsilon_a)_{ub}$ [km]	100.0
Var. thrust	Off	DV source	n/a	e_t [-]	1.0×10^{-12}	$(\epsilon_e)_{ub}$ [-]	0.01
Long. target.	Off	DE_{rep} [-]	1	i_t [deg]	1.0×10^{-12}	$(\epsilon_i)_{ub}$ [deg]	0.1
N_{arcs} [-]	1	N_{iter} [-]	1000 *	Ω_t [deg]	1.0×10^{-12}	$(\epsilon_\Omega)_{ub}$ [deg]	1.0
m_0 [kg]	2000.0	N_P [-]	10D	ω_t [deg]	1.0×10^{-12}	$(\epsilon_\omega)_{ub}$ [deg]	1.0
T [mN]	350.0	C_F [-]	0.6	Λ_t [deg]	n/a	$(\epsilon_\Lambda)_{ub}$ [deg]	n/a
I_{sp} [s]	2000.0	C_R [-]	0.8			W_t [-]	0.1
n_k [-]	40	$(t_f)_{ub}$ [day]	140.0 †	a_0 [km]	24505.9	W_a [-]	1.0
Propag. scheme	CI	$(t_f)_{lb}$ [day]	135.0	e_0 [-]	0.725	W_e [-]	1.0
OA_{step} [day]	4.0	λ_{ub} [-]	500 ‡	i_0 [deg]	7.0	W_i [-]	1.0
Avg. scheme	Trapez.	λ_{lb} [-]	-500 ‡	Ω_0 [deg]	1.0×10^{-12}	W_Ω [-]	0.0
Avg. variable	Time			ω_0 [deg]	1.0×10^{-12}	W_ω [-]	0.0
Eclipse thr. [%]	Off	Launch		θ_0 [deg]	1.0×10^{-12}	W_m [-]	n/a
J_2 perturb. [-]	Off	date [UTC]	n/a			W_Λ [-]	n/a

* The maximum number of iterations was modified to 2000 and 1500 respectively for executions #3 and #4 in Table 3.3.
† The upper TOF boundary was modified to 139.0, 138.5, and 137.7 days respectively for the subsequent executions.
‡ The upper and lower co-state boundaries were modified set to $\pm1.0\times10^4$ for the subsequent executions.

Table 3.3: Comparison of HOSTEP's Case A1 results with the analytical optimum from reference indirect methods.

	Time-of-flight t_f [days]	Revolutions N_{rev} [-]	Propellant mass m_{prop} [kg]
HOSTEP, solution #1	138.68	195	213.81
HOSTEP, solution #2	137.95	195	212.70
HOSTEP, solution #3	137.74	195	212.37
HOSTEP, solution #4	137.45	193	211.91
IGEOR [Montealegre-Avila, 2015]	137.41	190	211.86
[Sanchez and Campa, 2014]	137.5	190	212
[Geffroy and Epenoy, 1997]	137.5	190	212

HOSTEP's best solution differs by only 1 hr in TOF with the analytical global optimum computed with IGEOR. This shows that, despite its simplified co-state dynamics, the hybrid method can achieve a great accuracy in minimum-TOF optimization, even when a single co-state arc is employed. The deviation of both HOSTEP and IGEOR with the other reference indirect implementations is larger, which arises from the differences in the values employed for the target orbit and the fact that the reference results were presented with a limited precision. This is because the former indirect methods used $e_t = 0.0001$ and $i_t = 0.01$ as target, and when IGEOR was executed with these adjusted values, it reached exactly the same results upon round-off. Furthermore, HOSTEP's results indicate a deficiency in the number of revolutions, which is evaluated based on the true longitude variation. Since the details about the approach used in the reference indirect methods are undocumented, this could arise from a difference in the approach used. Nonetheless, HOSTEP's solution #3 and #4 exhibit a difference of two revolutions and about 4.5 hr, which is not feasible because the lowest orbital period along the entire trajectory is 10.6 hr.

As expected, HOSTEP's solution accuracy worsens as the TOF design space is enlarged. Nonetheless, this is also

affected by the maximum allowed number of iterations, as may be observed in the convergence plot shown in Figure D.1. The corresponding computational times for the four HOSTEP executions were 72 min, 84 min, 162 min, and 118 min respectively, under the same conditions using the hardware and software described in Appendix E. This shows that the effect of increasing the maximum allowed number of iterations is approximately linear on computational time. The optimization in IGEOR was executed twice, both reaching the same solution presented in Table 3.3 and requiring 87 and 92 min respectively.
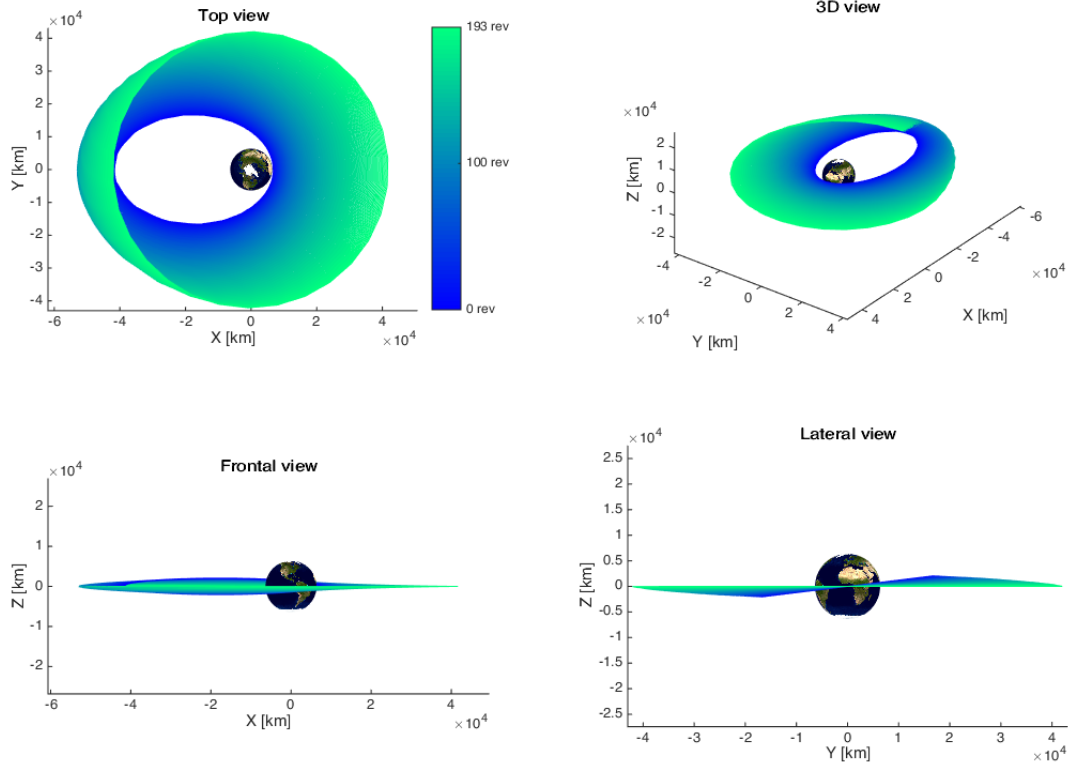
Figure 3.1: Illustration of HOSTEP's optimal Case A1 trajectory in (a) top, (b) 3D, (c) frontal, and (d) lateral views.

Figure 3.1 illustrates the trajectory evolution over time with the aid of a color scale for HOSTEP's solution #4. These projections are very similar to the ones presented in [Montealegre-Avila, 2015], which is to be expected since the TOF and propellant expenditure are also similar. The color overlap observed near apogee for Figure 3.1 (b) occurs because the inclination is not exactly zero, which helps to visualize that the optimal trajectory first raises the apogee altitude, while adjusting the inclination, and gradually decreases it afterwards.

Table 3.4: Comparison of the CI results and OA error for the Case A1 optimal trajectories.

| | Solution #1 | | Solution #2 | | Solution #3 | | Solution #4 | |
	CI result	OA error	CI result	OA error	CI result	OA error	CI result	OA error
a [km]	42165.923	-98.533	42164.580	30.756	42164.877	-24.502	42164.684	-32.227
e [-]	2.309E-5	0.011	1.453E-5	0.011	1.129E-4	0.011	5.278E-4	0.012
i [deg]	1.263E-3	0.229	1.685E-3	0.229	2.928E-3	0.115	2.590E-4	0.172
m [kg]	1786.186	0.000	1787.301	0.000	1787.632	0.000	1788.086	0.000

The OA error for the main Keplerian elements of interest – semi-major axis, eccentricity and inclination – is presented in Table 3.4 and the variation over time of the elements corresponding to solution #4 is shown in Figure 3.2. The element evolution propagated with CI is very similar to that presented in [Montealegre-Avila, 2015], and the OA approximation closely resembles the CI propagation. It must be clarified that the optimization was carried out using CI and only the final trajectory was propagated with both CI and OA to evaluate the OA error. A closer inspection at the OA errors shown in Table 3.4 reveals that it nearly satisfies the requirements from Table 2.1 for the best two solutions, and the combination of OA errors is still deemed acceptable for a priori optimization since the OA error for a is well below the requirement. Consequently, is was decided to employ OA for the optimization process in Case B.
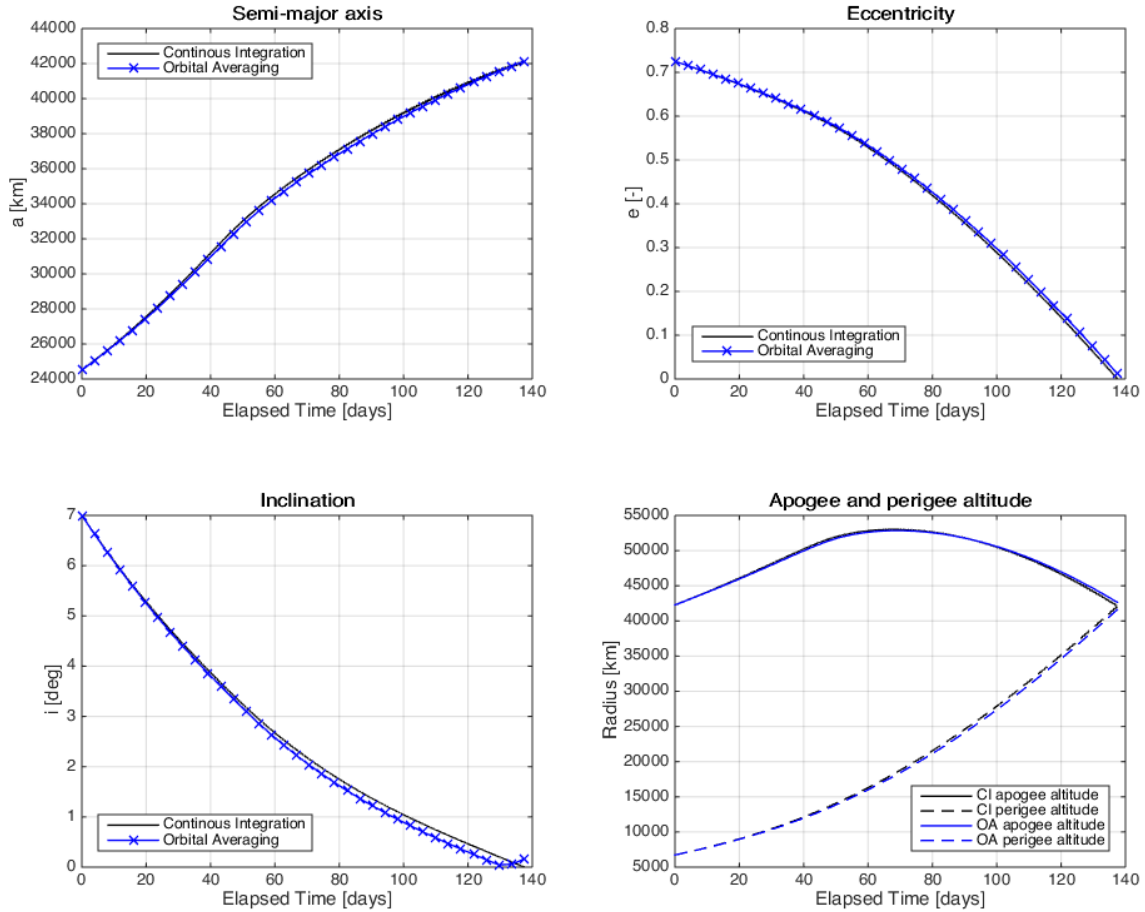
Figure 3.2: Comparison between the CI and OA evolution of the main Keplerian elements – (a) semi-major axis, (b) eccentricity, (c) inclination, and (d) apogee and perigee altitude – for the optimal Case A1 trajectory computed with HOSTEP.

Table 3.5: Optimal co-states for the four Case A1 solutions computed with HOSTEP.

Solution #	Node #	λ_p [-]	λ_f [-]	λ_g [-]	λ_j [-]	λ_k [-]
1	1	-0.0480	52.6406	-48.2484	1000.0000	120.7258
	2	0.0027	999.9970	15.5347	144.8889	-93.7007
2	1	-0.2841	-1023.5188	-199.3850	4804.5768	404.0099
	2	-0.0334	9845.9082	76.2233	4018.6292	-403.6160
3	1	-0.2230	-1639.1706	510.9440	2415.2460	-112.6927
	2	-0.0503	9996.3885	-246.3236	6551.9830	218.3890
4	1	-0.1758	-2411.9416	-1.4360	1793.2510	-1.5825
	2	-0.0524	9851.1740	-8.2504	5658.9952	-4.0730

The values of the optimal co-states calculated with the hybrid method are shown in Table 3.5. These optimal co-states differ significantly from those of the reference indirect methods, though this is to be expected due to the different nature of the hybrid formulation. In essence, these co-states are merely a mathematical tool in the optimal control theory developed in [Pontryagin, 1986]. It is important to mention that, due to the geometry of the control laws, the co-states may be scaled by any factor without altering the optimal trajectory. This also explains why the co-states of different HOSTEP solutions differ from one another. Furthermore, the four solutions show that the DE scales the optimal co-states in accordance with the imposed co-state boundaries. Albeit not critical for the accuracy of the solution, the author recommends scaling the co-state for the semi-latus rectum in future versions of HOSTEP to avoid this effect. For example, one could multiply λ_p by p to create a vector of co-states that vary with similar orders of magnitude.

3.1.2. CASE A2: J2-PERTURBED TRAJECTORY

The inputs for this case are shown in Table 3.6 and are similar to those of the A1 trajectories, with the exception of the J_2 effect perturbation. Table 3.7 shows the comparison of the results from HOSTEP and IGEOR for the J_2-perturbed and unperturbed trajectories. It should be clarified that IGEOR [Montealegre-Avila, 2015] is based on the indirect methodology developed in [Sanchez and Campa, 2014] which did not present perturbed trajectories. The projections of HOSTEP's optimal J_2-perturbed trajectory are shown in Figure 3.3.

Table 3.6: Inputs for the Case A2 executions.

Comp. mode	Optimization	DE mode	Random	a_t [km]	42165.0	$(\epsilon_a)_{ub}$ [km]	100.0
Var. thrust	Off	DV source	n/a	e_t [-]	1.0×10^{-12}	$(\epsilon_e)_{ub}$ [-]	0.01
Long. target.	Off	DE_{rep} [-]	1	i_t [deg]	1.0×10^{-12}	$(\epsilon_i)_{ub}$ [deg]	0.1
N_{arcs} [-]	1	N_{iter} [-]	2000	Ω_t [deg]	1.0×10^{-12}	$(\epsilon_\Omega)_{ub}$ [deg]	1.0
m_0 [kg]	2000.0	N_P [-]	10D	ω_t [deg]	1.0×10^{-12}	$(\epsilon_\omega)_{ub}$ [deg]	1.0
T [mN]	350.0	C_F [-]	0.6	Λ_t [deg]	n/a	$(\epsilon_\Lambda)_{ub}$ [deg]	n/a
I_{sp} [s]	2000.0	C_R [-]	0.8			W_t [-]	0.1
n_k [-]	40	$(t_f)_{ub}$ [day]	138.5	a_0 [km]	24505.9	W_a [-]	1.0
Propag. scheme	CI	$(t_f)_{lb}$ [day]	135.0	e_0 [-]	0.725	W_e [-]	1.0
OA_{step} [day]	4.0	λ_{ub} [-]	1.0×10^4 *	i_0 [deg]	7.0	W_i [-]	1.0
Avg. scheme	Trapez.	λ_{lb} [-]	-1.0×10^4 *	Ω_0 [deg]	1.0×10^{-12}	W_Ω [-]	0.0
Avg. variable	Time			ω_0 [deg]	1.0×10^{-12}	W_ω [-]	0.0
Eclipse thr. [%]	Off	Launch		θ_0 [deg]	1.0×10^{-12}	W_m [-]	n/a
J2 perturb. [-]	Off	date [UTC]	n/a			W_Λ [-]	n/a

* The upper and lower co-state boundaries were modified set to $\pm1.5\times10^4$ for the fourth execution presented in Table 3.3.
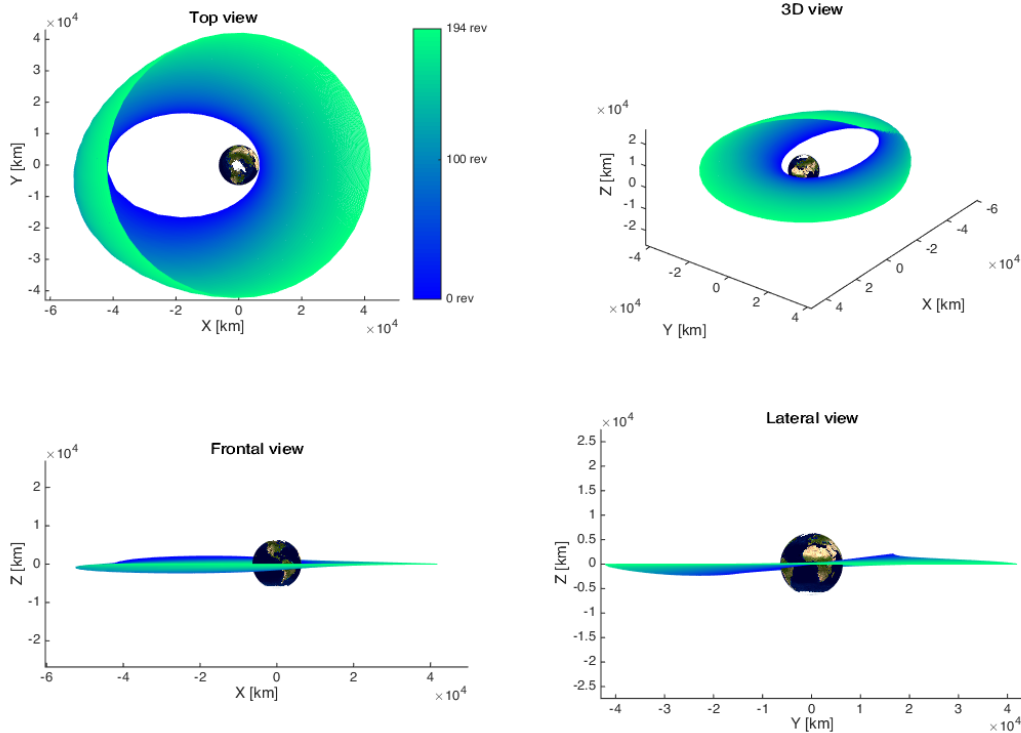
Figure 3.3: Illustration of the optimal Case A2 trajectory from the (a) top, (b) 3D, (c) frontal, and (d) lateral perspective.

Figure 3.3 shows a clear resemblance with the optimal trajectory from Case A1, with a noticeable secular drift for the argument of perigee in the positive direction, as expected from the analytical secular calculation previously shown with Equation 2.82. The evolution of a, e, i, and the radius at the apses, which may be found in Figure D.2, is identical to that of Case A1, except for the inclination which shows only a minor difference. Moreover, Figure 3.4 compares the CI and OA evolution for this case, revealing a larger OA error than previ-

ously observed in Case A1. This is to be expected because of the larger disturbing acceleration experienced by the spacecraft. The comparison of the CI and OA terminal values and the corresponding OA error can be found in Table D.3 and show that the OA error exceed the requirements when including the J_2 perturbation.
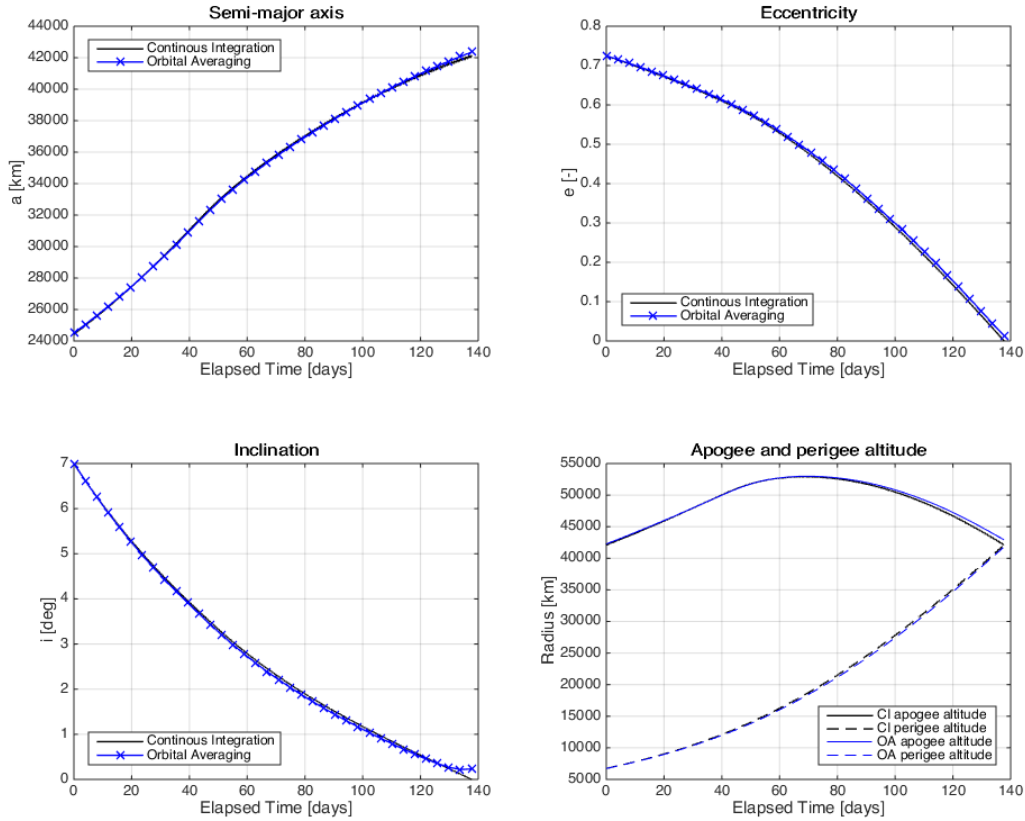
Figure 3.4: Comparison between the CI and OA evolution of the main Keplerian elements – (a) semi-major axis, (b) eccentricity, (c) inclination, and (d) apogee and perigee altitude – for HOSTEP's optimal Case A2 trajectory.

Table 3.7: Comparison of the four HOSTEP's solutions for Case A2 with the reference solutions.

	Time-of-flight t_f [days]	Revolutions N_{rev} [-]	Propellant mass m_{prop} [kg]	Geodetic Longitude Λ_f [deg]
HOSTEP, J_2-pert. solution #1	137.78	195	212.46	-92.74
HOSTEP, J_2-pert. solution #2	137.72	194	212.35	-67.84
HOSTEP, J_2-pert. solution #3	137.71	194	212.32	-61.62
HOSTEP, J_2-pert. solution #4	137.71	194	212.32	-63.65
IGEOR, J_2-perturbed	137.75	192	212.39	339.22
HOSTEP, unperturbed	137.45	193	211.91	24.80
IGEOR, unperturbed	137.41	190	211.86	208.99

The results of the four executions are shown in Table 3.7. Clearly, the inclusion of the J_2 perturbation leads to a longer TOF for this GTO-GEO trajectory. Nonetheless, it is important to realize that the effect of this perturbation varies with the problem under consideration and whether the perturbing acceleration favours the orbital transfer. In this particular case, the resulting effect calculated with HOSTEP is significantly similar to the findings from IGEOR [Montealegre-Avila, 2015]. Moreover, despite the slight difference in the e_t and i_t target values, it is also consistent with the results presented in [Geffroy and Epenoy, 1997], which showed a 2 hr increment in the TOF when incorporating the J_2 perturbation. Another important observation is that the final geodetic longitude varies for the four solutions, which is of particular interest for the later analysis in Case C, see section 3.3. In all four J_2-perturbed trajectories computed with HOSTEP, the final geodetic longitudes lie within a 30 deg arc that is Westwards with respect to the value for the unperturbed solution. The fact it varies 2 deg for solution #3 and #4 although these are nearly identical, indicates a high sensitivity of the final geodetic longitude to minute variations in the thrust profile.
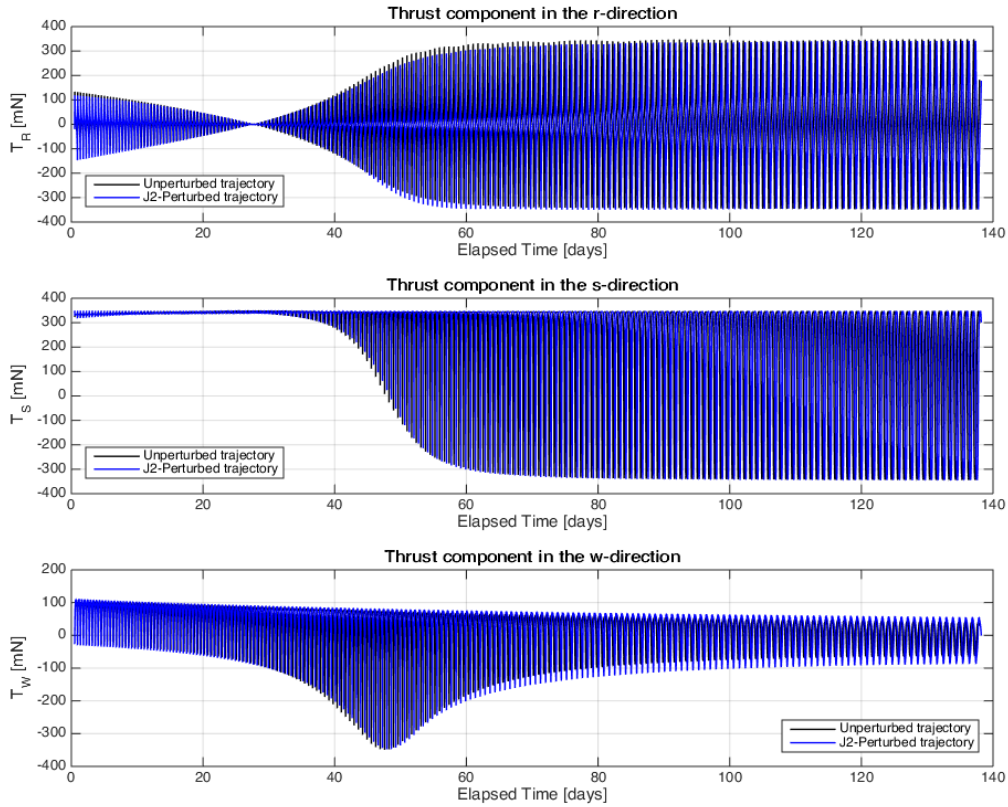
Figure 3.5: Evolution of the thrust components in the RSW frame for the optimal unperturbed and J$_2$-perturbed trajectories of HOSTEP.

The thrust components in the RSW frame are shown in Figure 3.5 for the unperturbed and J$_2$-perturbed trajectories. Visual inspection of the oscillations confirms that the thrust components in the s- and w-directions reach maximum values near the apses, as expected, whereas that in the r-direction is maximal near the nodal points. The overall trend is very similar for both profiles, with only small differences between the oscillation amplitude at certain regions. Nonetheless, since not all orbital elements are being targeted, these differences may simply indicate an alternative trajectory solution rather than a direct consequence of the J$_2$ effect.

Lastly, the corresponding co-states of the previous solutions are shown in Table 3.8. The results for the first three executions are very similar, with the exception of λ_g and λ_k which vary accordingly. The latter is to be expected because Ω remains close to 2π rad for this trajectory – see Figure D.3 – which causes $\sin(\Omega)$, and therefore g and k to remain close to zero, and therefore the effect of λ_g and λ_k on the trajectory is very small. For solution #4, every co-state exhibits an increase of a factor of 1.44 with respect to solution #3. This is a result of the larger co-state boundaries imposed for this execution and confirms the earlier claim that all co-states can be scaled by an equal factor without a change in the control laws or the resulting trajectory.

Table 3.8: Optimal co-state results from HOSTEP for the four Case A2 solutions.

Solution #	Node #	λ_p [-]	λ_f [-]	λ_g [-]	λ_j [-]	λ_k [-]
1	1	-0.1895	-2220.1352	-464.3983	2140.6352	-432.7277
	2	-0.0589	10000.0000	1955.4042	5793.1818	-2210.9064
2	1	-0.1922	-2391.8218	-188.8911	2298.0134	-146.3361
	2	-0.0497	9828.5920	1775.2011	5133.8198	-2366.2391
3	1	-0.1847	-2474.6186	-422.0736	1956.8875	-438.6879
	2	-0.0543	10000.0000	1903.5074	5755.0460	-2123.9345
4	1	-0.2662	-3567.3017	-608.4431	2820.9600	-632.3952
	2	-0.0783	14415.5563	2744.0119	8296.2182	-3061.7660

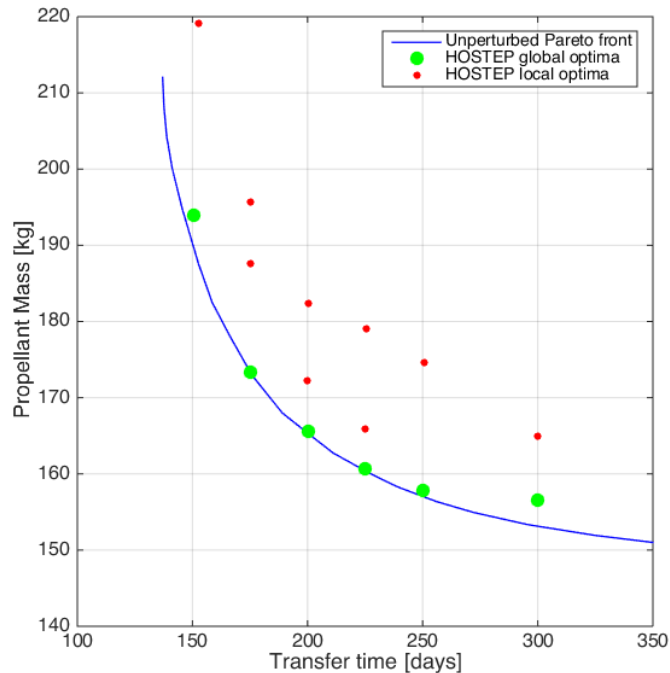## 3.2. CASE B: MINIMUM-PROPELLANT GTO-GEO TRAJECTORY

This section demonstrates the novel ability of the hybrid methodology, i.e. to optimize minimum-propellant trajectories with coasting arcs. The resulting optimal trajectories successfully reproduce the reference Pareto front computed with the indirect method in [Sanchez and Campa, 2014], revealing an exceptional competency in terms of solution accuracy. Additionally, this scenario shows the power of the OA technique, which is used in all sub-cases to lower the computational cost without dramatically hindering the accuracy.

Similarly to Case A, all orbital perturbations are neglected in this case as they are not incorporated in the reference results. The strategy employed to ease the automation of the different evaluations is to fix the TOF and optimize the trajectory for propellant-minimization using the inputs shown in Table 3.9. Additionally, OA is employed with the best settings identified during the validation tests in subsection 2.7.1. Figure 3.6 shows that the solutions found for a TOF of 150, 175, 200, 225, 250, and 300 days coincide nearly exactly with the Pareto front of analytical global optima.

Table 3.9: Inputs for the Case B executions.

Comp. mode	Optimization	DE mode	Random	a_t [km]	42165.0	$(\epsilon_a)_{ub}$ [km]	100.0
Var. thrust	On	DV source	n/a	e_t [-]	1.0×10^{-12}	$(\epsilon_e)_{ub}$ [-]	0.01
Long. target.	Off	DE_{rep} [-]	4	i_t [deg]	1.0×10^{-12}	$(\epsilon_i)_{ub}$ [deg]	0.1
m_0 [kg]	2000.0	N_P [-]	10D	Ω_t [deg]	1.0×10^{-12}	$(\epsilon_\Omega)_{ub}$ [deg]	1.0
N_{arcs} [-]	1	N_{iter} [-]	1000	ω_t [deg]	1.0×10^{-12}	$(\epsilon_\omega)_{ub}$ [deg]	1.0
T [mN]	350.0	C_F [-]	0.6	Λ_t [deg]	n/a	$(\epsilon_\Lambda)_{ub}$ [deg]	n/a
I_{sp} [s]	2000.0	C_R [-]	0.8			W_t [-]	0.0
n_k [-]	40	$(t_f)_{ub}$ [day]	150.01 *	a_0 [km]	24505.9	W_a [-]	1.0
Propag. scheme	OA	$(t_f)_{lb}$ [day]	149.99 *	e_0 [-]	0.725	W_e [-]	1.0
OA_{step} [day]	4.0	λ_{ub} [-]	1.0×10^6	i_0 [deg]	7.0	W_i [-]	1.0
Avg. scheme	Trapez.	λ_{lb} [-]	-1.0×10^6	Ω_0 [deg]	1.0×10^{-12}	W_Ω [-]	0.0
Avg. variable	Time			ω_0 [deg]	1.0×10^{-12}	W_ω [-]	0.0
Eclipse thr. [%]	Off			θ_0 [deg]	1.0×10^{-12}	W_m [-]	1000.0
J$_2$ perturb. [-]	Off	Launch date [UTC]	n/a			W_Λ [-]	n/a

* The TOF upper and lower bounds were adjusted accordingly for the 175-, 200-, 225-, 250-, 300-day trajectories.

Figure 3.6: HOSTEP's propellant-optimal solutions for the Case B trajectory relative to the Pareto front presented in [Sanchez and Campa, 2014].

The high accuracy with which HOSTEP's global optima resemble the analytical global solutions is relatively astonishing. Despite employing a single co-state arc, the deviation between the linearized co-state dynamics and the corresponding optimal EOM does not considerably influence the resulting trajectories. This is an exceptional result because it shows that the hybrid method does not necessarily jeopardize the solution accuracy, in comparison to the analytical global optimum of indirect methods, while being able to harness the enhanced convergence and flexibility of the direct method. Figure 3.6 also illustrates the random nature of the DE optimizer because some of the four executions for each TOF are not visible, i.e. they yielded a mass expenditure that exceeds 220 kg. This signifies the importance of executing several DE repetitions for any problem and the fact that there is room for improvement in the DE algorithm employed.
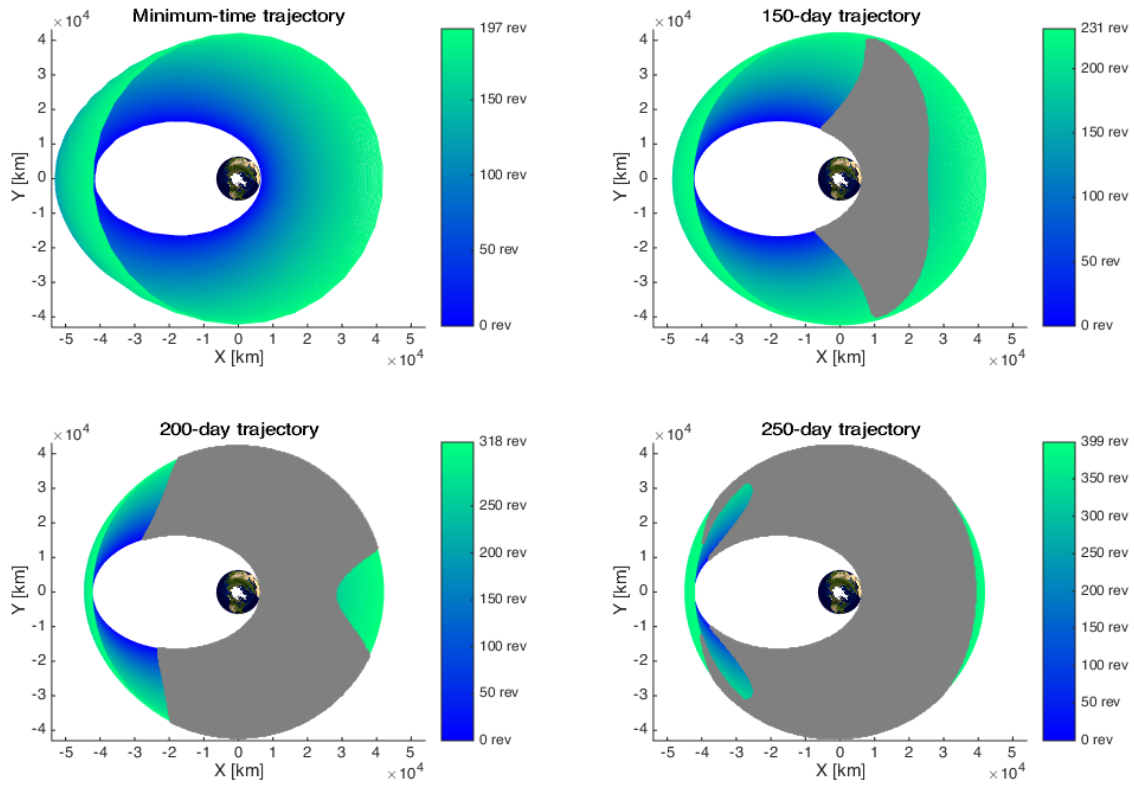
Figure 3.7: Illustration of HOSTEP's optimal Case B trajectories and coasting regions (depicted in grey) for a TOF of (a) 137, (b) 150, (c) 200, and (d) 250 days.

Figure 3.7 illustrates the 2D projection of the optimal 150-, 200-, and 250-day trajectories, as well as the optimal minimum-time trajectory from Case A1, with the coasting regions depicted in grey. The coasting behaviour is as expected, with the engine switched off near perigee because the apogee altitude is already close to the target radius. In particular, the 150-day trajectory exhibits a very similar coasting pattern to that of the propellant-optimal trajectory calculated in [Montealegre-Avila, 2015] for the same TOF.

Moreover, the comparison of the terminal element values computed with CI and OA for the 250-day optimal trajectory are shown in Table 3.10. It clarifies that the OA accuracy satisfies the requirement, with the most significant error occurring in eccentricity. It also shows a 1 kg error in the computed mass consumption, which is caused by the averaging of the coasting arcs and remains acceptable for a priori optimization.

Table 3.10: Comparison of the final CI and OA values for the 250-day minimum-propellant GTO-GEO trajectory computed with HOSTEP.

State variable	CI result	OA result	OA error
Semi-major axis a [km]	42062.214	42043.576	-18.638
Eccentricity e [-]	0.002	0.012	0.010
Inclination i [deg]	0.104	0.029	-0.075
Total mass m [kg]	1842.187	1843.146	0.959
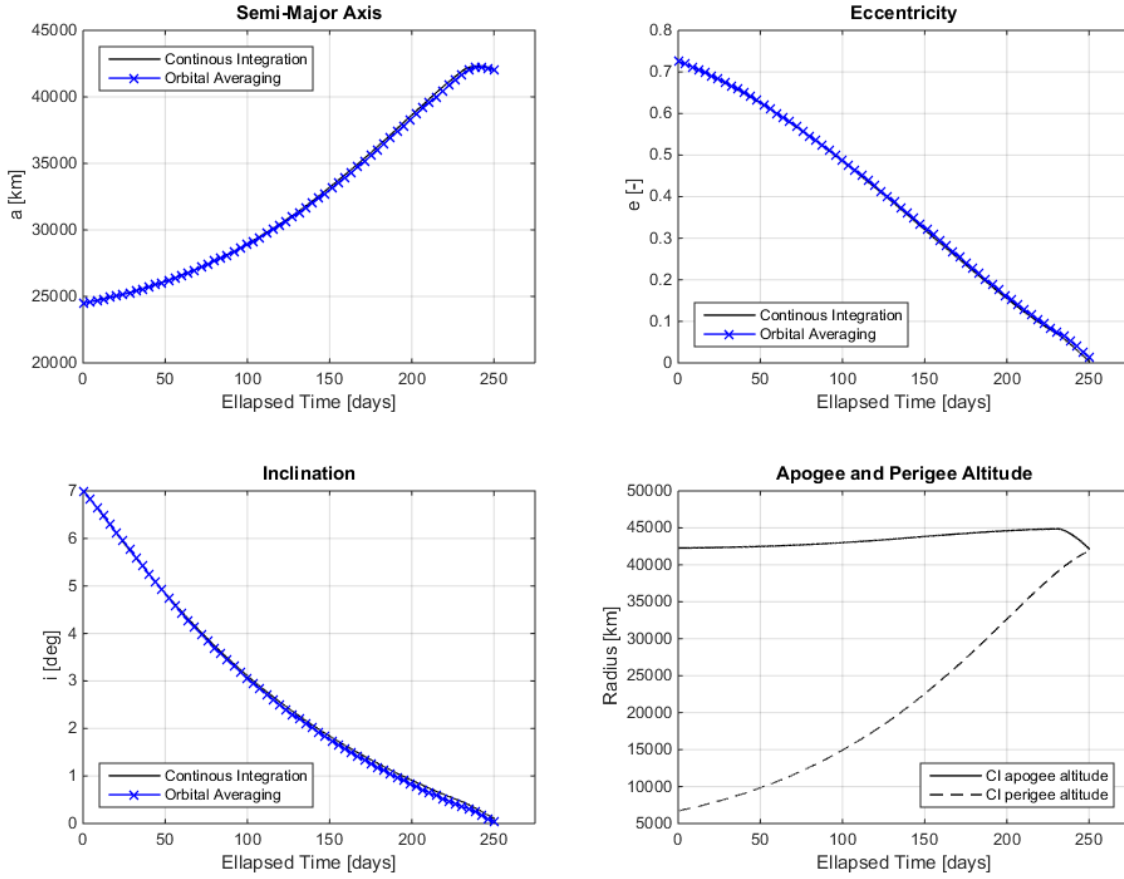
Figure 3.8: Evolution of the main Keplerian elements for the 250-days propellant-optimal GTO-GEO trajectory computed with HOSTEP.

Furthermore, the CI and OA evolution of the orbital elements for the 250-day trajectory is shown in Figure 3.8. The evolution of the elements is as expected, with the eccentricity and inclination exhibiting a regular behaviour for a GTO-GEO transfer and the semi-major axis experiencing a rapid circularization near the end, which is also visible in the trajectory 2D projection in Figure 3.7. The evolution of these elements for the optimal 150- and 200- day trajectories, as well as the comparison of the terminal values, may be found in Appendix D and are consistent with the previous analysis. The OA technique enabled a faster generation of optimal trajectories, with an average DE execution time of 30 min, 43 min, and 62 min for the 150-, 200-, and 250-day trajectories respectively. Compared to the 57 min from the Case A1 solutions that were also limited to 1000 iterations per DE execution, this shows again that OA is a tempting alternative for the study of GTO-GEO trajectories since the error with respect to CI remains acceptable.

3.3. CASE C: GTO-GEO TRAJECTORY WITH LONGITUDE TARGETING

The purpose of this case is to evaluate HOSTEP's ability to target the final geodetic longitude. As explained in section 2.4, this is accomplished by extending the Aggregate Objective Function (AOF) to further incorporate the difference between the achieved final geodetic longitude and the target value. The GTO-GEO longitude targeting is first demonstrated for minimum-time trajectories with arbitrary geodetic longitude targets. Afterwards, a real trajectory from one of GMV's customer is first optimized for TOF minimization with longitude targeting using HOSTEP and subsequently with EPTOS. Lastly, the former GTO-GEO transfer is optimized for longitude targeting in combination with propellant minimization.

3.3.1. CASE C1: TIME-OPTIMAL SOLUTIONS

Firstly, the minimum-TOF GTO-GEO trajectory from Case A2 is optimized for the arbitrary target values of Λ_t =0.0, 90.0, 180.0, 200.0, 240.0 deg. Note that Case A2 was focused on the minimum-time GTO-GEO J_2-

perturbed trajectory without longitude targeting, and that the final geodetic longitude from was -64 deg. The inputs for this case, which are shown in Table 3.11, are very similarly to those of Case A2. The J$_2$ perturbation is considered but not the Earth shadow regions. OA is not employed in this case, neither for the optimization nor for the post-processing propagation, because it is unable to accurately propagate rapidly changing variables and is therefore unsuitable for longitude targeting.

Table 3.11: Inputs for the Case C1 minimum-time executions.

Comp. mode	Optimization	DE mode	Random	a_t [km]	42165.0	$(\epsilon_a)_{ub}$ [km]	100.0
Var. thrust	Off	DV source	n/a	e_t [-]	1.0×10^{-12}	$(\epsilon_e)_{ub}$ [-]	0.01
Long. target.	On	DE_{rep} [-]	4	i_t [deg]	1.0×10^{-12}	$(\epsilon_i)_{ub}$ [deg]	0.1
m_0 [kg]	2000.0	N_P [-]	$10D$	Ω_t [deg]	1.0×10^{-12}	$(\epsilon_\Omega)_{ub}$ [deg]	1.0
N_{arcs} [-]	1	N_{iter} [-]	1000	ω_t [deg]	1.0×10^{-12}	$(\epsilon_\omega)_{ub}$ [deg]	1.0
T [mN]	350.0	C_F [-]	0.6	Λ_t [deg]	0.0 *	$(\epsilon_\Lambda)_{ub}$ [deg]	1.0
I_{sp} [s]	2000.0	C_R [-]	0.8			W_t [-]	0.1
n_k [-]	30	$(t_f)_{ub}$ [day]	139.0	a_0 [km]	24505.9	W_a [-]	1.0
Propag. scheme	CI	$(t_f)_{lb}$ [day]	135.0	e_0 [-]	0.725	W_e [-]	1.0
OA_{step} [day]	n/a	λ_{ub} [-]	1.0×10^4	i_0 [deg]	7.0	W_i [-]	1.0
Avg. scheme	n/a	λ_{lb} [-]	-1.0×10^4	Ω_0 [deg]	1.0×10^{-12}	W_Ω [-]	0.0
Avg. variable	n/a			ω_0 [deg]	1.0×10^{-12}	W_ω [-]	0.0
Eclipse thr. [%]	Off	Launch		θ_0 [deg]	1.0×10^{-12}	W_m [-]	n/a
J$_2$ perturb. [-]	On	date [UTC]	n/a			W_Λ [-]	0.1

* This value was modified to 90.0, 180.0, 200.0, 240.0 deg for the consecutive executions presented in Table 3.12.

Table 3.12: Outputs results from HOSTEP for Case C1.

Time-of-flight t_f [days]	Revolutions N_{rev} [-]	Propellant mass m_{prop} [kg]	Geodetic Longitude Λ_f [deg]
138.22	197	213.10	0.07
138.08	197	212.89	90.01
138.94	197	214.22	180.00
138.80	195	214.01	200.01
138.21	194	213.10	240.11

The results presented in Table 3.12 demonstrate that longitude targeting with an accuracy of 1.0 deg is possible with an expense of less than one day in TOF. The average computational time was 116 min per single DE repetition for all simulations, under the same conditions and using the hardware and software described in Appendix E. This constitutes a percentage increase of 49% relative to the 72 and 84 min that were required for solutions #1 and #2 of the Case A1 unperturbed GTO-GEO minimum-TOF trajectory, both of which also employed 1000 DE iterations. Nonetheless, this is to be expected due to the additional computational cost of optimizing the final geodetic longitude.

Furthermore, the previous results demonstrate the robust convergence of HOSTEP to a varied range of target geodetic longitudes. Is it known that the indirect method implemented in IGEOR has convergence difficulties to target values that are π rad away from the nominal final geodetic longitude. Additionally, it is also unable to converge to a feasible solution for a range of longitudes Westwards of the nominal final value. The previous results show that, conversely to IGEOR, HOSTEP can optimize in both West- and Eastwards directions without noticeable convergence difficulties.

3.3.2. CASE C2: TIME-MINIMIZATION FOR REAL MISSION

Based on the previous promising results, a real mission with electric orbit raising was evaluated. The inputs for this simulation are shown in Table 3.13. The launch date is omitted for confidentially reasons and eclipses are thus neglected. This is a very interesting case because the indirect method implemented in IGEOR does not converge to a feasible solution when targeting the final geodetic longitude. The trajectory is first optimized with HOSTEP for minimum-time alone and, after narrowing down the TOF design space, it is optimized for

minimum-time in combination with longitude targeting. The resulting optimized trajectory is then input into GMV's high fidelity EPTOS optimizer and the results are compared in Table 3.14.

Table 3.13: Inputs for the Case C2 minimum-time GTO-GEO trajectory with longitude targeting.

Comp. mode	Optimization	DE mode	Random	a_t [km]	42165.0	$(\epsilon_a)_{ub}$ [km]	100.0
Var. thrust	Off	DV source	n/a	e_t [-]	1.0×10^{-12}	$(\epsilon_e)_{ub}$ [-]	0.01
Long. target.	Off *	DE_{rep} [-]	4	i_t [deg]	1.0×10^{-12}	$(\epsilon_i)_{ub}$ [deg]	0.1
m_0 [kg]	3521.0	N_P [-]	10D	Ω_t [deg]	1.0×10^{-12}	$(\epsilon_\Omega)_{ub}$ [deg]	1.0
N_{arcs} [-]	1	N_{iter} [-]	500	ω_t [deg]	1.0×10^{-12}	$(\epsilon_\omega)_{ub}$ [deg]	1.0
T [mN]	688.0	C_F [-]	0.6	Λ_t [deg]	176.0	$(\epsilon_\Lambda)_{ub}$ [deg]	1.0
I_{sp} [s]	1736.0	C_R [-]	0.8			W_t [-]	0.1
n_k [-]	30	$(t_f)_{ub}$ [day]	130.0	a_0 [km]	24468.54	W_a [-]	1.0
Propag. scheme	CI	$(t_f)_{lb}$ [day]	120.0	e_0 [-]	0.7230	W_e [-]	1.0
OA_{step} [day]	n/a	λ_{ub} [-]	1.0×10^4	i_0 [deg]	5.9996	W_i [-]	1.0
Avg. scheme	n/a	λ_{lb} [-]	-1.0×10^4	Ω_0 [deg]	335.4239	W_Ω [-]	0.0
Avg. variable	n/a			ω_0 [deg]	182.0293	W_ω [-]	0.0
Eclipse thr. [%]	Off	Launch		θ_0 [deg]	14.6127	W_m [-]	n/a
J_2 perturb. [-]	On	date [UTC]	n/a			W_Λ [-]	0.1

* The trajectory was first optimized without targeting the final geodetic longitude to narrow down $(t_f)_{ub}$ and afterwards, the presented Λ_t was targeted.

Table 3.14: Comparison of the Case C2 results from HOSTEP and EPTOS.

	Time-of-flight t_f [days]	Propellant mass m_{prop} [kg]	Geodetic Longitude Λ_f [deg]
HOSTEP	123.29	430.48	176.3
EPTOS	123.31	430.52	176.0

The previous results demonstrate that HOSTEP is capable of solving a trajectory for which IGEOR is unable to converge to a feasible solution. It should be clarified that thanks to the fact that HOSTEP is fully integrated in GMV's ***focussuite*** ®, EPTOS can easily intake and refine the trajectory from HOSTEP within just a few clicks.

3.3.3. CASE C3: PROPELLANT-MINIMIZATION

To pursue a more realistic scenario, the author decided to optimize for a final geodetic longitude and simultaneously minimize the propellant expenditure. To be able to compare the results, this case evaluates the former GTO-GEO transfer from Case B and variable thrust is employed to generate a Pareto front with respect to TOF and propellant expenditure. The final geodetic longitude value is fixed at 28.5 deg East as this corresponds to a highly desired orbital position for GEO communication satellites broadcasting over Europe [EUTELSAT, 2014]. The modified inputs when compared to Table 3.11 are namely: variable thrust "On", $\Lambda_t = 28.5$ deg, and $W_m = 1000.0$. Additionally, the TOF is fixed at certain values to enhance the convergence rate of the DE optimization process. In Figure 3.9, the resulting solutions are compared with the Pareto front of the analytical global optima for the unperturbed trajectory without longitude targeting produced using the indirect method in [Sanchez and Campa, 2014]. The 2D projections of these trajectories are shown in Figure 3.10.

Table 3.15: Inputs for the Case C3 minimum-propellant executions.

| Comp. mode	Optimization	DE mode	Random	a_t [km]	42165.0	$(\epsilon_a)_{ub}$ [km]	100.0
Var. thrust	On	DV source	n/a	e_t [-]	1.0×10^{-12}	$(\epsilon_e)_{ub}$ [-]	0.01
Long. target.	On	DE_{rep} [-]	3	i_t [deg]	1.0×10^{-12}	$(\epsilon_i)_{ub}$ [deg]	0.1
m_0 [kg]	2000.0	N_P [-]	10D	Ω_t [deg]	1.0×10^{-12}	$(\epsilon_\Omega)_{ub}$ [deg]	1.0
N_{arcs} [-]	1	N_{iter} [-]	1000	ω_t [deg]	1.0×10^{-12}	$(\epsilon_\omega)_{ub}$ [deg]	1.0
T [mN]	350.0	C_F [-]	0.6	Λ_t [deg]	28.5	$(\epsilon_\Lambda)_{ub}$ [deg]	1.0
I_{sp} [s]	2000.0	C_R [-]	0.8			W_t [-]	0.0
n_k [-]	30	$(t_f)_{ub}$ [day]	150.01 *	a_0 [km]	24505.9	W_a [-]	1.0
Propag. scheme	CI	$(t_f)_{lb}$ [day]	149.99 *	e_0 [-]	0.725	W_e [-]	1.0
OA_{step} [day]	n/a	λ_{ub} [-]	1.0×10^4	i_0 [deg]	7.0	W_i [-]	1.0
Avg. scheme	n/a	λ_{lb} [-]	-1.0×10^4	Ω_0 [deg]	1.0×10^{-12}	W_Ω [-]	0.0
Avg. variable	n/a			ω_0 [deg]	1.0×10^{-12}	W_ω [-]	0.0
Eclipse thr. [%]	Off	Launch		θ_0 [deg]	1.0×10^{-12}	W_m [-]	1000.0
J_2 perturb. [-]	On	date [UTC]	n/a			W_Λ [-]	0.1

* The TOF upper and lower bounds were adjusted accordingly for the 175-, 200-, 225-, 250-, 300-day trajectories.
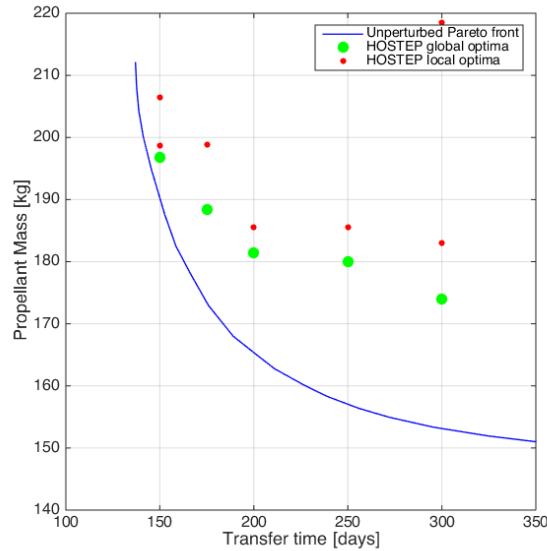
Figure 3.9: HOSTEP's propellant-optimal solutions for the GTO-GEO J_2-perturbed transfer to the 28.5 deg East orbital position relative to the Pareto front for the unperturbed GTO-GEO trajectory without longitude targeting from [Sanchez and Campa, 2014].

The results presented in Figure 3.9 demonstrate that the novel hybrid methodology is capable of simultaneously optimizing for a target geodetic longitude and minimizing the propellant expenditure. The performance of the DE algorithm is worse that that observed in Case B, as one of the three executions for some of the TOF evaluated yields a propellant mass that exceeds 220 kg. Moreover, the results show a propellant difference of up to about 20 kg relative to the unperturbed results without longitude targeting. One possibility is that the physical phenomena involved in this trajectory act against the optimization objective. However, the previous tests for longitude targeting in combination with TOF-minimization did not exhibit large differences with the untargeted case. Additionally, the 2D projections of the 150- and 175- day solutions are very similar to the behaviour observed in Case B. Therefore, this may indicate there is a deficiency in the current optimization process and HOSTEP cannot converge to a better trajectory within the allowed number of iterations. Another possibility is that the lack of scaling in the co-state vector is hindering the convergence of the the DE algorithm. However, since this was not a problem for the minimum-propellant optimization in Case B, the author first recommends upgrading the DE algorithm to a more sophisticated algorithm and then re-evaluating this case. Nonetheless, the results demonstrate that the hybrid methodology is capable of targeting the final geodetic longitude while simultaneously minimizing the mass, and therefore it is superior to the indirect method in IGEOR.
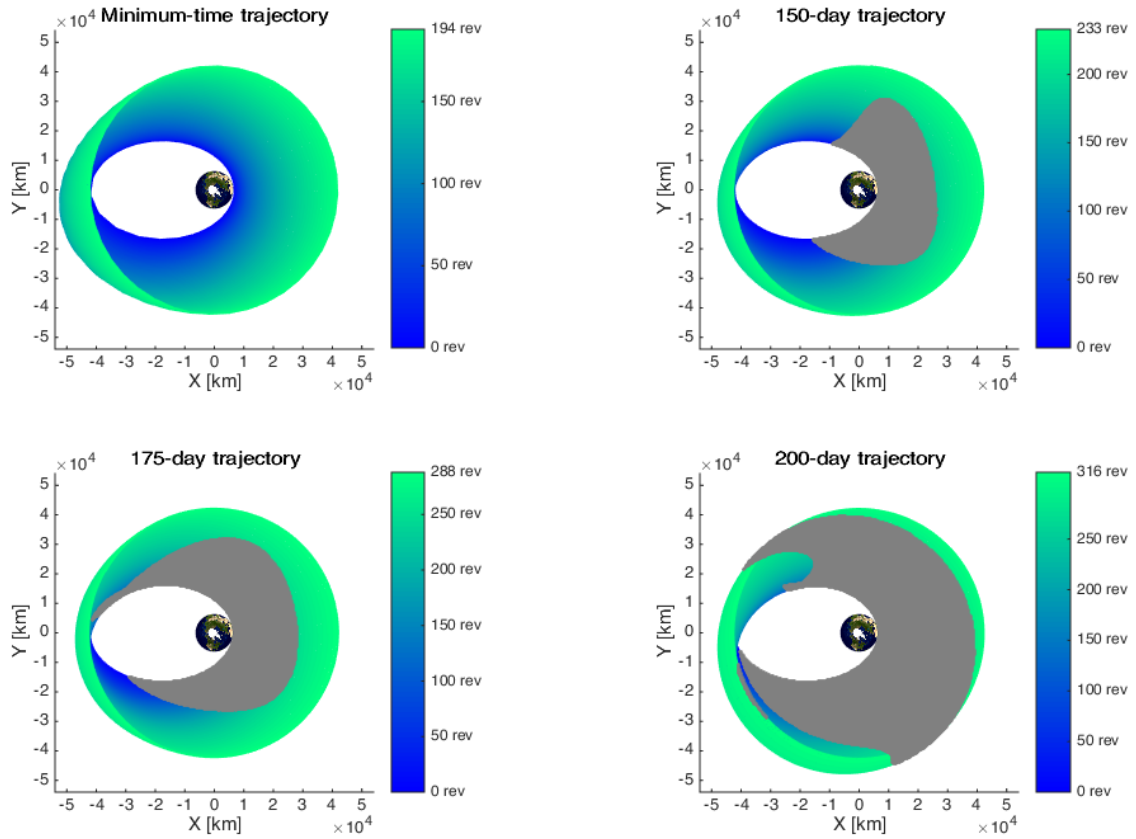
Figure 3.10: Illustration of HOSTEP's optimal (a) Case A2 trajectory and optimal Case C3 trajectories and coasting regions (depicted in grey) for a TOF of (b) 150, (c) 175, and (d) 200 days.

3.4. CASE D: MINIMUM-TIME LEO-GEO TRAJECTORY

This case is aimed at testing the capabilities of HOSTEP in a LEO-GEO transfer and to compare the results with those of the previous hybrid methodology presented in [Kluever, 2010; Boudestijn, 2014]. To resemble the reference data as much as possible, his trajectory does not incorporate the J_2 perturbation but it does includes eclipses. The engine switch-off threshold is set to 80.0% of nominal sunlight and the launch date is set to 2000/01/01 12:00:00.000. However, it should be clarified that the reference data do not reveal the sunlight threshold when the engine is switched off and, more importantly, the launch hour was not specified in [Kluever, 2010]. Continuous thrust is assumed outside of Earth shadow regions and the optimization is performed using CI. The TOF upper boundary was gradually increased until the optimization converged to a final orbit that satisfied the requirements. The list of input parameters is shown in Table 3.17, the illustration of the optimal trajectory over time is illustrated in Figure 3.11, and the main results are presented in Table 3.16.

Table 3.16: Comparison of the Case D results for HOSTEP and reference indirect methodologies.

	Time-of-flight t_f [days]	Revolutions N_{rev} [-]	Propellant mass m_{prop} [kg]
HOSTEP	218.0	1410	193.38
[Boudestijn, 2014]	209.49	n/a	224.67
[Kluever, 2010]	199.0	n/a	192.96

Table 3.16 shows a large TOF discrepancy with the solution from [Kluever, 2010], which may be caused by the lack precise launch hour information. This is because the Earth shadow regions may dramatically increase the required TOF if the eclipses take place near apogee. Given the large required computational effort, the author deemed inefficient to iteratively vary the launch hour. Therefore, the author claims that the comparison with this reference results is inconclusive.

Table 3.17: Inputs for the Case D executions.

| Comp. mode	Optimization	DE mode	Random	a_t [km]	42165.0	$(\epsilon_a)_{ub}$ [km]	100.0
Var. thrust	Off	DV source	n/a	e_t [-]	1.0×10^{-12}	$(\epsilon_e)_{ub}$ [-]	0.01
Long. target.	Off	DE_{rep} [-]	5	i_t [deg]	1.0×10^{-12}	$(\epsilon_i)_{ub}$ [deg]	0.1
m_0 [kg]	1200.0	N_P [-]	$10D$	Ω_t [deg]	1.0×10^{-12}	$(\epsilon_\Omega)_{ub}$ [deg]	1.0
N_{arcs} [-]	1	N_{iter} [-]	1000	ω_t [deg]	1.0×10^{-12}	$(\epsilon_\omega)_{ub}$ [deg]	1.0
T [mN]	401.706	C_F [-]	0.6	Λ_t [deg]	n/a	$(\epsilon_\Lambda)_{ub}$ [deg]	n/a
I_{sp} [s]	3300.0	C_R [-]	0.8			W_t [-]	0.1
n_k [-]	30	$(t_f)_{ub}$ [day]	218.0	a_0 [km]	6927.0	W_a [-]	1.0
Propag. scheme	CI	$(t_f)_{lb}$ [day]	199.0	e_0 [-]	0.0	W_e [-]	1.0
OA_{step} [day]	4.0	λ_{ub} [-]	500.0	i_0 [deg]	28.5	W_i [-]	1.0
Avg. scheme	Trapez.	λ_{lb} [-]	-500.0	Ω_0 [deg]	1.0×10^{-12}	W_Ω [-]	0.0
Avg. variable	Time			ω_0 [deg]	1.0×10^{-12}	W_ω [-]	0.0
Eclipse thr. [%]	80.0	Launch	2000/01/01	θ_0 [deg]	1.0×10^{-12}	W_m [-]	n/a
J_2 perturb. [-]	Off	date [UTC]	12:00:00.000			W_Λ [-]	n/a
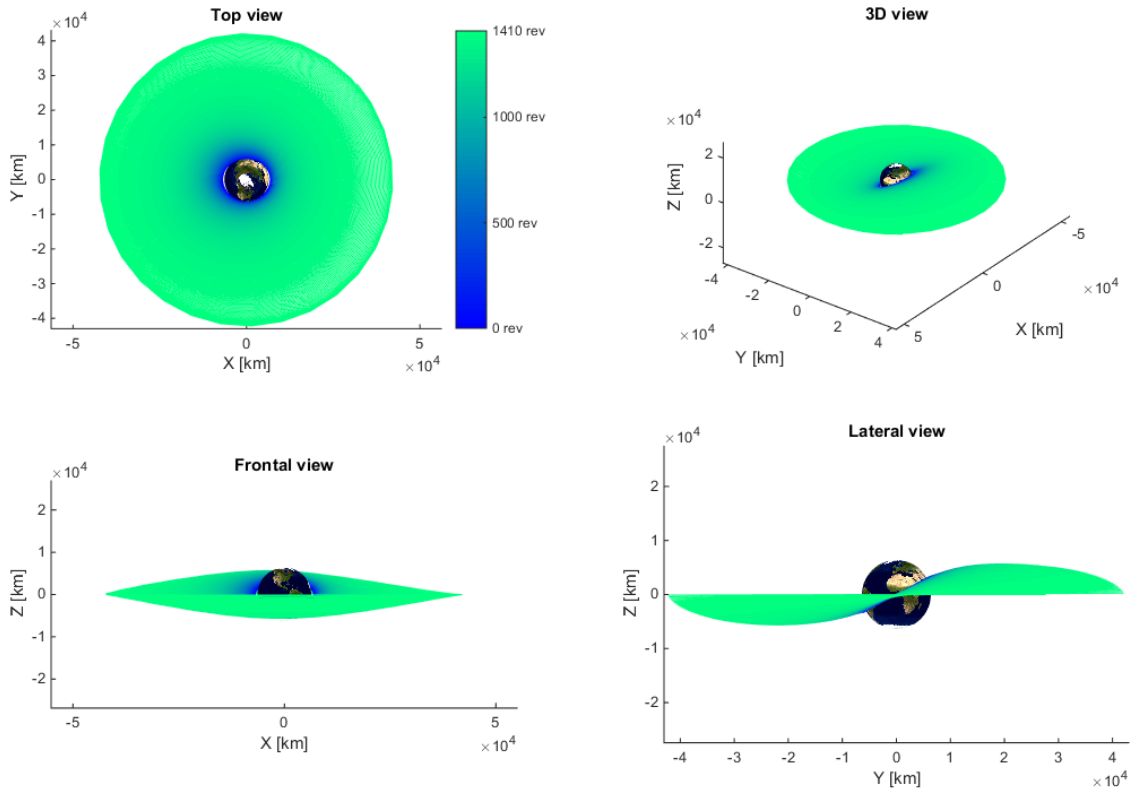
Figure 3.11: Illustration of the optimized Case D trajectory.

Although the optimal trajectory from HOSTEP also deviates considerably from the result of [Boudestijn, 2014], the trajectory projections show a large resemblance with the reference results. The trajectory behaves as expected, with a gradual combination of orbit raising and decreasing inclination. In Figure 3.12, the evolution of the main orbital elements is illustrated with greater detail and shows a similar pattern to the optimal solution from [Boudestijn, 2014]. The author believes HOSTEP's results are superior because the elements' evolution in the reference data exhibit a small difficulty in circularizing the orbit in the last few days. The fact that the later research by Gomez [2015] identified several rooms for improvement in the implementation of Boudestijn [2014] leads the author to believe this reference result may be flawed.

Another potential reason for the TOF discrepancy with both reference results may be a difference in the employment of the Earth shadow model. HOSTEP's simulations switched off the engine when the received sunlight was below 80% below nominal, and this could be different in the reference solutions since this detail is not clarified. If the threshold employed in [Kluever, 2010; Boudestijn, 2014] was smaller, this would lead to a longer

TOF without necessarily an increment in mass expenditure, because thrust is continuous outside shadow regions. Nonetheless, the author acknowledges that this may only partially account for the discrepancy and the previous arguments likely have a stronger impact.
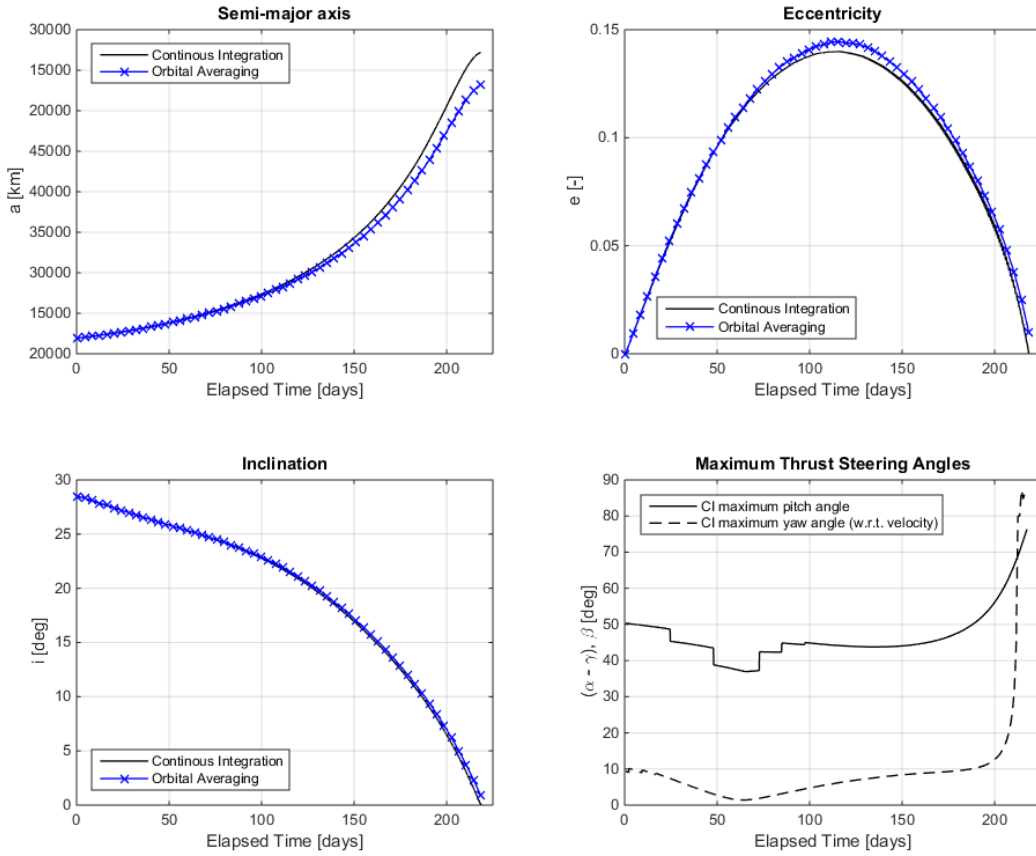
Figure 3.12: Evolution of the main Keplerian elements for the Case D optimal trajectory.

Figure 3.12 also shows the thrust steering angle evolution from HOSTEP's solution, which exhibits a very similar pattern to that obtained by Boudestijn [2014]. This also includes the dip in both steering angles at around $t = 60$ days. The reason why it exhibits step increments is due to the discretization of every revolution with a certain number of integration steps. This was verified through visual inspection for a large number of integration steps, $n_k = 1000$, and the dip pattern was indeed more continuous.

Lastly, Figure 3.12 also shows that the OA approximation is prone to large errors in this type of trajectory. A closer inspection at Table 3.18 confirms that the OA errors are well above the requirements previously specified in Table 2.1. This is not entirely surprising because, the orbital period in LEO is much shorter than that of GTO, for which the OA error was already large. Together with longer exposure to continuous thrusting in the LEO-GEO transfer, this leads to an OA error in a and i which is unacceptable even for a priori optimization. It is possible that an OA_{step} of 2 days would significantly reduce this error, but it would also mitigate the gain in computational cost and therefore the incentive to employ OA. It is therefore recommended to implement a variable step propagator in future versions of HOSTEP, see section 5.2, as it would allow for using a small step at lower altitudes and increase it as the orbital period becomes longer.

Table 3.18: Comparison of the final CI and OA values for the optimal Case D trajectory.

State variable	CI result	OA result	OA error
Semi-major axis a [km]	42166.803	38259.854	-3906.948
Eccentricity e [-]	0.00033	0.0098	0.0095
Inclination i [deg]	0.0057	0.8932	0.8875
Total mass m [kg]	1006.615	1008.094	1.479

4

Discussion

"Life is 10 percent what happens and 90 percent of how one reacts to it." – Charles Swindoll.

Whereas the previous chapter presents the optimization results and the corresponding factual observations, this chapter provides the author's interpretations and own opinion about the novel hybrid methodology. The discussion is divided between the scientific aspects of the research presented in this thesis and the practical aspects of the HOSTEP software tool. The former aims to answer the research questions from chapter 1 and evaluates the effectiveness of the coasting mechanism and longitude targeting, as well as the suitability of the methodology for a priori optimization and its performance relative to that of analytical indirect methods. The latter focuses on the performance of the DE algorithm, the objective function, the Orbital Averaging (OA) technique, the versatility of HOSTEP and its practical suitability.

4.1. Performance of the Coasting Mechanism

The research presented in this thesis has demonstrated that the hybrid method employed in [Kluever, 2010; Boudestijn, 2014; Gomez, 2015] can be successfully modified to incorporate a mechanism for coasting (non-thrusting) arcs. The most suitable means to achieve this was originally deemed to be through the use of a thrust switching function adapted from the research presented in Gao and Kluever [2004]. The results from HOSTEP confirm that this implementation can successfully model non-thrusting arcs and thus dramatically improve the flexibility of former hybrid methodologies, which were ill-conditioned for propellant-minimization problems due to the constant thrust assumption.

The switching function strategy has proven to be a very efficient technique to simulate non-thrusting arcs because it only requires the addition of two optimization variables for any trajectory discretized with a single co-state arc, $N_{arc} = 1$. Additionally, its performance is very effective and yields a highly reliable accuracy, because the minimum-propellant GTO-GEO optimal trajectories hereby presented coincide with high fidelity with the analytical Pareto front developed in [Sanchez and Campa, 2014] with an indirect method. The performance of this mechanism has exceeded the author's expectations as a single co-state arc is already sufficient to reach a high accuracy relative to the analytical global optima.

Moreover, the hybrid method did not experience greater convergence difficulties compared to the minimum-propellant problem, beyond the two additional design variables and the fact that the design space had to be increased to allow λ_m to be significantly larger than the other co-states – this is further elaborated in the DE discussion, see subsection 4.4.1. This constitutes strong evidence in favour of the hybrid methodology because the indirect method from [Sanchez and Campa, 2014] that is implemented in IGEOR [Montealegre-Avila, 2015] has been identified to suffer considerable difficulties in approaching propellant-minimization. Whereas the indirect method requires a computationally expensive homotopy process to gradually proceed from a fixed-time minimum-TOF solution to the minimum propellant trajectory, which does not always converge to a feasible solution, HOSTEP is capable of finding a feasible solution in all cases tested with only the convergence rate being affected. To enhance the convergence rate, the TOF was fixed at certain values in HOSTEP's executions, which was also deemed to be more insightful and immediate than varying the weights. However, the author strongly believes that the TOF needs not be fixed and the reason why HOSTEP otherwise required longer computational times is largely due to the limitations of the DE implemented and the lack of co-state scaling, which

can be overcome in future HOSTEP versions. Furthermore, the hybrid method is fundamentally better suited for complex optimization cases because the convergence of direct methods is know to be more robust than indirect methods [Betts, 1998], which is particularly of interest for varied combinations of optimization objectives, orbital perturbations, and operational constraints.

4.2. PERFORMANCE OF LONGITUDE TARGETING

The results of HOSTEP demonstrate that targeting the final geodetic longitude is possible with the hybrid method and, in fact, superior to the indirect implementation of IGEOR [Montealegre-Avila, 2015] in terms of the convergence radius. The targeting of the final geodetic longitude is accomplished through the numerical optimization process by incorporating an additional weighted term in the optimization objective function. This strategy was deemed superior to the alteration of the Hamiltonian because that would require the addition of new co-states to be optimized, hence increasing the optimization cost. This constitutes yet a further leap for the hybrid methodology as it enables the solving of rendez-vous problems, which is a critical functionality for the positioning of GEO satellites. It worth clarifying that this is only possible thanks to HOSTEP's versatility as it allows for employing either CI or OA in the optimization process, of which the latter is unable to accurately propagate the rapidly-changing variable. The previous hybrid studies employed OA throughout the optimization process and only made use of CI for the precise final propagation of the optimized trajectory [Kluever and Pierson, 1995; Boudestijn, 2014; Gomez, 2015], rendering the methodology unable to optimize for a target geodetic longitude due to the unacceptable OA error for the true anomaly.

For the case of longitude targeting, the hybrid methodology is superior to the indirect method implemented in IGEOR [Montealegre-Avila, 2015] because only the convergence rate is affected by the additional optimization objective, while the convergence radius remains stable even for large geodetic longitude changes. Conversely, the complex analytical nature of the indirect method renders IGEOR ill-conditioned for certain target longitude ranges, for which it is not able to converge to a solution that satisfies the Two-Point-Boundary-Value-Problem (TPBVP). Nonetheless, this is not surprising because it is widely known that direct methods exhibit a greater convergence radius in comparison to analytical indirect approaches [Betts, 1998]. The heritage from IGEOR showed that the indirect method adapted from [Sanchez and Campa, 2014] experiences considerable convergence difficulties for out-of-phase longitude changes and finds no feasible solution at all for a certain range of longitudes Westwards from the unconstrained solution. Even when disregarding eclipses and altitude constraints, the relatively simple combination of J_2-perturbations and the objectives of minimizing t_f and targeting Λ_f proved to be too challenging. Conversely, the direct nature of the hybrid method allowed it to excel at this task and solve a diverse range of longitude targeting scenarios, including those that IGEOR is incapable of converging for. Moreover, the author is strongly confident that it can incorporate broader orbital perturbations, more operational constraints, and further optimization objectives with only the computational time being affected. Therefore, the author claims that the hybrid methodology is superior to the current indirect method implementation in IGEOR for this type of optimization problem.

The results of the hybrid method for the combination of longitude targeting and propellant minimization performed worse than expected. When compared with the Pareto front of the unperturbed GTO-GEO trajectory without longitude target, the results of HOSTEP show more propellant expensive solutions for all TOF values evaluated. The fact that the propellant increases by up to 20 kg for the J_2-perturbed trajectory with longitude targeting leads the author to believe there is room for improvement in the formulation. It is possible that the J_2 acceleration opposes the motion of the spacecraft through the trajectory for this particular combination of inputs. Nonetheless, the author recommends reevaluating this case after implementing a more advanced DE algorithm and enhanced scaling for the co-state vector. Nonetheless, HOSTEP's performance for this objective combination exceeds by far the capabilities of IGEOR. This is because either propellant minimization or longitude targeting on its own is challenging for the indirect method in IGEOR and the combination does not lead to any feasible solution.

4.3. RELATIVE PERFORMANCE FOR A PRIORI OPTIMIZATION

The question whether the hybrid method in HOSTEP or the indirect method in IGEOR is better suited for a priori optimization remains highly debatable and depends on the problem type under consideration. As usual, both the hybrid and indirect method have their corresponding strengths and weaknesses, and the following discussion is thus divided into the different problem types.

For the task of **TOF-minimization**, HOSTEP shows room for improvement because it required excessive com-

putational times. The upper and lower TOF boundaries used for HOSTEP's Case A executions results were set very close to the TOF-optimal solution from IGEOR because HOSTEP's DE process had difficulties, in terms of convergence rate, reaching the optimal solution when the allowed TOF range was too large. Nonetheless, this may not a flaw of the hybrid methodology because the previous studies presented in [Kluever, 2010; Boudestijn, 2014; Gomez, 2015] did not exhibit this behaviour. Instead, the author believes this weakness stems from the limitations of the DE algorithm employed, which is further elaborated in subsection 4.4.1. For the quick generation of minimum-TOF a priori trajectories, IGEOR is superior to the current version of HOSTEP because the latter undergoes a much longer computational time and sometimes exhibits difficulties reaching the global optimum for very large design spaces. Nonetheless, this is to be expected for simple minimum-TOF problems because IGEOR features less optimization variables. In terms of accuracy, however, the direct nature of HOSTEP allows it simulate a broader combination of orbital perturbations and operational constraints, which are not included in the analytical indirect formulation of IGEOR and may perhaps be not possible to capture at all with an indirect method due to the analytical nature. Any change to the formulation of the TPBVP analytically derived for IGEOR, such as the inclusion of third-body perturbations, requires re-deriving the complete TPVBP – i.e. the Hamiltonian first and second derivatives with respect to all controls and all state variables, the co-state EOM, as well as the transversality conditions – which is a very labour intensive task that cannot be succeeded without a profound knowledge of the subject. Therefore, IGEOR is a wiser choice for minimum-time problems with limited perturbations inclusion – only eclipses or J2 perturbation – and limited operational constraints – only minimum perigee height and maximum apogee height – because any further addition cannot be modelled without developing a new IGEOR. Conversely, for minimum-TOF applications that require a full near-Earth perturbation model or additional operational constraints, HOSTEP is more suitable because these implementations can be easily incorporated in the hybrid method without altering the optimal control laws. Nonetheless, the author recommends first calculating an a priori optimal TOF with IGEOR and then refine the solution through HOSTEP, at least until HOSTEP's DE algorithm is further improved. Additionally, for the specific application of GTO-GEO trajectories, the OA technique proved to be efficient and as accurate as required for a priori optimization and is therefore the recommended choice for HOSTEP, unless longitude targeting is required, because it significantly reduces the computational load.

In **propellant-minimization** problems, the novel hybrid optimization method proved to be very effective thanks to the coasting mechanism. Moreover, the OA technique enabled a faster generation of solutions for fixed-time GTO-GEO transfers with different TOF. The resulting accuracy is comparable with that of the indirect method implemented in IGEOR and it only experienced difficulties in reaching the global optima for large TOF solutions. It is known that IGEOR requires an excessive computational time as compared to TOF-minimization because the homotopy process gradually optimizes for propellant-minimization from a specified minimum-time solution. The fact that a minimum-time solution is required to begin with, that the optimization process is significantly elongated, and that IGEOR has difficulties converging to a feasible solution for some trajectories [Montealegre-Avila, personal communication], renders it inferior to HOSTEP. Furthermore, it is a certainty that the direct nature of HOSTEP allows it to incorporate more perturbations or constraints, making it a more suitable choice also for complex problems, and the author is confident that it can cope with these without its convergence radius being significantly affected.

For the task of **longitude targeting**, the hybrid method is noticeably superior to the indirect formulation in IGEOR. First of all, this application requires a high level of accuracy with respect to orbital perturbations, which cannot be modelled in IGEOR and are generally not included in indirect methods [Geffroy and Epenoy, 1997; Jiang et al., 2012; Sanchez and Campa, 2014]. Therefore, the hybrid method is fundamentally better suited since the indirect formulation would otherwise need to be analytically re-derived to incorporate these further perturbations. Regarding the convergence performance, HOSTEP is also better suited, because there was no convergence difficulties encountered for a varied set problems with different final geodetic longitudes. Conversely, IGEOR exhibits limited convergence when targeting the final geodetic longitude and cannot find feasible solutions for a range of final longitude values Westwards of the nominal final longitude. Nonetheless, the current version of HOSTEP has difficulties in locating the global optimum for a large design space in TOF. Therefore, the author recommends first solving the minimum-time problem in IGEOR without longitude targeting and then solving for a certain final geodetic longitude with HOSTEP, with the computed TOF from IGEOR as an indication to establish the TOF bounds. For the combination of longitude targeting and propellant minimization, HOSTEP is undoubtedly better suited because the indirect method implemented in IGEOR cannot converge to feasible solutions for this problem type. Furthermore, the author believes HOSTEP's performance may be improved through enhancing the DE algorithm and scaling the co-states of the mass and the semi-latus rectum.

4.4. The HOSTEP Software Tool

This section provides the author's discussion on topics that do not constitute a scientific question but are rather related to the practical performance of the developed hybrid methodology. The discussion first evaluates the DE algorithm, followed by the propagation technique and the practical suitability of HOSTEP.

4.4.1. Performance of the DE Algorithm

The author believes that the that the reason why HOSTEP sometimes required extensive computational times is due to the combination of inefficiencies in the DE algorithm extracted from [Wang, 2010] and the rigidity of the objective function. Nonetheless, the objective function shows great resemblance with that employed in the indirect method from [Sanchez and Campa, 2014] so the author believes the weakness lies in the DE algorithm. Additionally, the objective function was specifically engineered towards the requirement of lowering the fine-tuning effort required for the user, which remains a goal of interest for future developments. It should be clarified, nonetheless, that the DE algorithm currently implemented was a good choice for this thesis thanks to its simplicity, its readily availability in *Fortran90* and, more importantly, because the computational time was not a primary requirement. In future work, however, the author recommends investigating superior DE implementations such as the self-adaptive DE algorithm available in ESA's PaGMO toolbox [Biscani et al., 2010]. The PaGMO toolbox may be a great choice to lower the computational optimization load because it employs parallel computing, and it is free for both personal and commercial use. Moreover, the PaGMO optimization algorithms incorporate many recent developments and state-of-the-art findings in the field of optimization that are not incorporated in HOSTEP's DE algorithm since it is based on the original publication from [Storn and Price, 1997]. Additionally, the self-adaptive DE algorithm available in PaGMO would allows the user to input a range of C_F and C_R values instead of specific values, and this would further diminish the fine-tuning effort by the end user.

Another limitation of the current DE algorithm is its stopping criteria, namely a maximum iteration boundary and a minimum residual value. For practical purposes it would be desirable to have more sophisticated stopping criteria that take into account the convergence rate of the solutions. For example, the DE optimization sometimes converges prematurely to a local optimum far from the global solution and it would be desirable to re-initiate the optimization process if such behaviour is detected. Additionally, the minimum residual value condition currently implemented is an interesting option when information about the global optimum is available, because the user can calculate the residual value of the desired solution and set the stopping condition accordingly. This is not the case in practical applications, however, because the user may not previously know the global optimum, meaning that HOSTEP's DE process may only terminate upon the maximum number of iterations. Ideally, the DE algorithm should terminate the optimization process if the solution has converged to a plateau with minute improvements to the objective function. These functionalities are available in PaGMO [Biscani et al., 2010] and support the recommendation in favour of its use for future HOSTEP developments.

4.4.2. Performance of the Propagation Technique

The OA technique adapted from [Boudestijn, 2014] has yielded great performance for the GTO-GEO transfers and enabled a quicker generation of the Pareto front in section 3.2. Nonetheless, the OA error observed during the validation tests A1-A3, as well as the OA error exhibited for the LEO-GEO trajectory, are too large even for a priori optimization. The author believes there may be room for improvement in the current OA implementation of HOSTEP because the results presented in [Boudestijn, 2014] may have achieved a higher level of accuracy, though it is not clearly documented. This was acceptable for this thesis because OA was not a critical functionality for the feasibility study of coasting arcs and the error remained close to the requirement imposed for a priori optimization. Nonetheless, the author recommends further investigating the OA implementation for future HOSTEP versions because it proved to be very effective for practical applications and it may be improved.

Additionally, the author recommends upgrading the underlying fixed-step RK4 propagation method to a variable-step propagator. The RK4 was a good choice for this thesis thanks to its simple implementation, because its accuracy was identified to be acceptable for a priori optimization [Jimenez-Lluva, 2016], and because the computational time was not a primary requirement. Although not necessarily more accurate, a variable-step propagation scheme would reduce the propagation computational cost and is therefore recommended for future HOSTEP developments. The literature study preceding this thesis concluded that the RKF7(8) is the most suit-

able variable-step integration scheme. Implementing a variable-step scheme is particularly interesting in combination with OA, because it would decrease the OA error. The reason for this that a fixed OA_{step} yields larger discrepancies at lower orbit altitudes, because as the orbital period grows, the number of revolutions decreases with OA_{step} and the OA error accumulation thus decreases. In fact, the hybrid method with OA presented in Gomez [2015] showed that the required OA_{step} grows gradually over time when using an RK4(5) integration scheme.

4.4.3. PRACTICAL SUITABILITY OF HOSTEP

HOSTEP constitutes an early commercial prototype whose future versions are envisioned to yield a new commercial software solution. The architecture of HOSTEP was designed towards this long term vision and offers a flexible platform for the future versions of the HOSTEP commercial prototype. The modular architecture described in Appendix B significantly eases the maintenance and enhancement of the software tool. Thanks to this design and the GUI, the future HOSTEP improvements can be completed rather easily, potentially within short internships, as the developer needs not understand the complexity of the complete project in detail but rather only the work-flow within the certain modules. For example, further orbital perturbations – such as luni-solar third-body attractions, third-order Earth oblateness perturbations, or atmospheric drag – can be incorporated through adjustments only in the "Force Model" and "Auxiliary Operations" modules. Similarly, the multi-objective optimization can be expanded to incorporate the experienced radiation fluence by solely modifying the objective function within the "Evaluator" module and including the radiation model in the "Auxiliary Operations" module.

Additionally, HOSTEP's GUI is fully integrated in ***focussuite*** ® to enable the automatic interaction with other GMV tools within the flight dynamics software product. This enabled a very fast validation throughout the code development process because the outputs of HOSTEP can be directly read by tools such as EVENTS, PROPAG, and EPTOS. This was also designed towards commercial long terms to enable not only a priori optimization during the mission planning phase, but also real-time monitoring and correction of the low-thrust trajectory with HOSTEP. In fact, the author believes that HOSTEP's ability to model a full near-Earth perturbations model together with operational constraints handling and multi-objective optimization makes HOSTEP also a potential future replacement of GMV's high-fidelity, EPTOS, because it allows for a priori optimization through OA as well as precise calculations with CI.

5

CONCLUSIONS AND RECOMMENDATIONS

"Whatever the mind of man can conceive and believe, it can achieve." – Napoleon Hill.

A novel hybrid methodology has been developed to answer the research question,

"To what extent can a hybrid combination of indirect and direct optimization methods using a multi-objective technique and a mechanism for coasting arcs yield superior optimal solutions than the analytical indirect method implemented in [Montealegre-Avila, 2015], specifically for minimum-propellant optimization problems of low-thrust many-revolution trajectories, while simultaneously allowing for targeting of the final geodetic longitude?"

The indirect nature of the method efficiently reduces the number of optimization variables and its direct counterpart provides an unmatchable flexibility to handle different problems without the need to re-derive the analytical control laws. The method is demonstrated through a high-level software prototype, enabling a configurable force and perturbations model as well as operational constraints handling and multi-objective optimization. The system's versatility is exploited through a modular software architecture, a flexible work-flow logic, and an intuitive interface, allowing the user to evaluate the optimization and simulation of minimum-time and minimum-propellant trajectories as well as targeting of the final geodetic longitude.

5.1. CONCLUSIONS

The purpose of this thesis was to bridge the weakness of former hybrid methodologies through the inclusion of a coasting mechanism to improve its performance relative to indirect approaches. The results presented in this thesis constitute a quantum leap for the hybrid optimization methodology in low-thrust many-revolution trajectory optimization. The original approach was already shown in [Kluever, 2010; Boudestijn, 2014] to be competitive with indirect methods for minimum-time trajectories, and its potential for multi-objective optimization was demonstrated in [Gomez, 2015]. Additionally, Gomez [2015] revealed the unmatchable flexibility of the hybrid methodology, as he incorporated a full near-Earth perturbations model in the software previously developed by Boudestijn [2014] without the need to adjust the mathematical foundation of the approach nor the optimal control laws, which is far from possible using analytical indirect methods. This thesis has reproduced the former hybrid methodology, with the exception of some orbital perturbations, and dramatically extended its functionality to address the last shortcomings that rendered it inferior to indirect approaches.

The first enhancement is the implementation of the coasting mechanism, which allows the optimizer to evaluate the efficiency of switching the engine off at every integration step and thus optimize for non-thrusting arcs as well. This constitutes a major advancement because all previous hybrid studies assumed constant-thrust outside of the Earth shadow regions and, consequently, all results were far from the analytical global optima for propellant-minimization trajectories. The coasting mechanism employed is based on a thrust switching function similar to that employed in [Gao and Kluever, 2004] for interplanetary trajectories. This strategy proved to be very efficient because it only requires two additional optimization variables to accurately model the coasting arcs over the entire trajectory, for any problem type. Moreover, it is also shown to be very effective because, even with a single co-state arc, the results for the minimum-propellant GTO-GEO trajectories are very close to the Pareto front produced with the indirect method in [Sanchez and Campa, 2014]. Therefore, this demonstrates

that, despite the simplified co-state dynamics, the hybrid methodology can successfully optimize trajectories with non-continuous thrust and match the accuracy of indirect methods for propellant-minimization problems.

The other weakness of the former hybrid methodologies was the inability to solve rendez-vous problems. This is because the Orbital Averaging (OA) embedded in the optimization process sacrificed the accuracy of the rapidly changing variable for a significantly lower computational load. Whereas most applications do not impose a requirement on the satellite's position within the final orbit, the success of some other applications rely critically on the satellite achieving not only an accurate final orbit but also a specific final geodetic longitude. This has been addressed by implementing both OA and Continuous Integration (CI) in the optimization process, allowing for an accurate monitoring of all state parameters when employing CI, though at an increased computational expense. Moreover, the deviation from the desired final geodetic longitude is included in the objective function to allow for a precise targeting without modifying the mathematical formulation nor the optimal control laws. This development breaches through the last weakness of the original hybrid method. The resulting hybrid method is able to optimize for longitude-targeting without jeopardizing the convergence radius, which was shown to be the major limitation of the indirect method developed in [Montealegre-Avila, 2015] and is a well-known drawback of indirect approaches in general [Betts, 1998]. Based on an optimal J2-perturbed GTO-GEO transfer, the hybrid method is employed to target a varied range of geodetic longitude in both East- and Westwards directions. The results show that longitude targeting can be accomplished through TOF increments within a day and reveal the robust convergence of the hybrid method. More importantly, it is shown that accurate longitude targeting can be accomplished while simultaneously minimizing the propellant expenditure, thus demonstrating the superiority of the novel hybrid methodology over the former hybrid approaches [Gomez, 2015; Boudestijn, 2014; Kluever, 2010] and the indirect methods [Montealegre-Avila, 2015; Sanchez and Campa, 2014; Geffroy and Epenoy, 1997] hereby evaluated.

The new implementation of the hybrid methodology from scratch enabled several other adjustments to the original approach that also enhanced its performance for practical applications. The most prominent is the new objective function, which was engineered to ease the fine-tuning effort required for the user. Whereas the former hybrid methods required an iterative tuning of the multi-objective optimization weights, the new objective function successfully scales the target orbit constraint such that the weights of the state elements can simply be set to unity, or zero for the elements that need not be targeted. Furthermore, the methodology is implemented in a high-level commercial prototype referred to as Hybrid Optimization Software for Trajectories with Electric Propulsion (HOSTEP). This prototype is integrated in GMV's toolbox for the launch and early operations phase, *focusleop* ®, which is available in GMV's commercial flight dynamics software solution *focussuite* ®. HOSTEP not only presents an efficient approach to optimize for propellant-minimization but also an effective method to target the final geodetic longitude. Both features are critical capabilities to enable affordable scientific renvez-vous missions as well as outstanding market opportunities for all-electric GEO communication satellites. Particularly in the latter case, it is important to enable longitude targeting throughout the electric orbit raising phase because it prevents the detrimental need for reallocation and the significant operation costs involved when the satellite is not in view of the operator's own stations.

This thesis shows that the novel hybrid methodology can match the accuracy of the analytical global optima computed with indirect methods. This is demonstrated both for minimum-time and minimum-propellant trajectories. Its direct nature makes it significantly more flexible than the indirect approach because the orbital perturbations and operational constraints can be easily modified without the need to analytically re-derive the Two-Point-Boundary-Value-Problem. Moreover, it is particularly superior to indirect methods for the complex optimization problem of low-thrust many-revolution trajectories because its convergence radius is not affected by the number of simultaneous optimization objectives, orbital perturbations considered or imposed constraints. The indirect method presented in [Montealegre-Avila, 2015] exhibited convergence difficulties in optimizing minimum-time GTO-GEO transfers with longitude-targeting along with eclipse and J2 perturbations. The results hereby presented show that the hybrid method excels at this task and can simultaneously optimize for propellant-minimization as well as incorporate further orbital perturbations and operational constraints without its convergence radius being affected.

5.2. Recommendations

Now that the true potential of the hybrid methodology has been demonstrated for the GTO(7.0°)-GEO transfer, the author recommends to test a wider scope of applications. To begin with, it is advised to demonstrate the optimization of orbital transfers to GEO from Super-Synchronous-Transfer-Orbits (SSTO) as well as from

GTO(28.5°), which is becoming an increasingly employed transfer since the Falcon9 may launch from Florida [SpaceX, 2015]. Additionally, the author recommends to evaluate some of the proposed low-thrust transfers to Medium-Earth-Orbit (MEO) for the all-electric Galileo Second Generation (GSG) mission, of which GMV is the prime contractor for the ground segment and may vastly benefit from this capability. Additionally, it is recommended to perform a shadowing campaign of one of the all-electric satellites recently launched by GMV's customers. The latter would allow to further enhance HOSTEP's commercial suitability by studying the deviation of the actual trajectory over time and may help identify further room for improvement. The demonstration of complex trajectories, such as Molniya eccentric orbits, is also recommended because HOSTEP could also be a useful resource to GMV's scientific projects which generally feature non-conventional scenarios.

To enhance the computational effort, improve the stopping criteria of the optimization process, and decrease the fine-tuning user effort even further, the author recommends upgrading the DE algorithm to the self-adaptive DE available in PaGMO. This open source multi-optimization software is freely available for both personal and commercial use, and offers a variety of global heuristic optimization methods. This alternative allows the user to input a range of C_F and C_R values which are also optimized, and to select more sophisticated stopping criteria than waiting for the maximum number of iterations [Biscani et al., 2010]. In particular, the Generalized Island Model (GIM) setup of the DE algorithm is recommended mainly because: it allows for parallel computing using different optimization algorithms and would significantly lower the computational load; the interaction of parallel populations would further prevent premature convergence to local optima; and the underlying formulation is beneficial to metaheuristic processes due to the vast amount of function evaluations involved [Izzo et al., 2012]. Furthermore, this toolbox was employed by Gomez [2015] for low-thrust optimization, and he further recommends employing the homogeneous DE settings, allowing migration and an archipelago of four islands. Lastly, the author also recommends to scale the Hamiltonian co-states of the element p and the mass m to create a co-state vector that varies homogeneously. Thus, it is advised to employ $\lambda_p p$ instead of λ_p and $\lambda_m m^{-1}$ instead of λ_m. Having implemented these enhancements to the methodology, it is recommended to re-evaluate the J_2-perturbed GTO-GEO transfer with longitude targeting from Case C3 and demonstrate whether the observed 20 kg increment relative to the unperturbed case without longitude targeting has been caused by deficiencies in the current optimization process or by the physical phenomena involved.

To decrease the computational load required by HOSTEP during the trajectory simulation process, the implementation of a variable-step propagator is advised, namely the RKF7(8) integration scheme. This is particularly interesting in combination with OA because the constant OA_{step} proved to be relatively inefficient. Particularly in the LEO-GTO hereby evaluated, the OA error led to unacceptable approximation errors because a constant step of 4.0 days was too large for the early revolutions. As the orbital period increases, the OA_{step} may be increased to maintain a similar number of revolutions, hence decreasing the propagation effort without jeopardizing the approximation accuracy. Another alternative would be to modify the work-flow of the OA algorithm so that it automatically adjusts the OA_{step} depending on the instantaneous orbital period.

To further enhance the applicability of HOSTEP, the author recommends extending the forces model to incorporate a configurable full near-Earth perturbation model. It should be clarified that this was not needed for the a priori optimization prototype hereby developed but it is interesting for HOSTEP to become a commercial product. In particular, the author's advice is to include: luni-solar third-body attractions, because they significantly affect the inclination of GEO satellites; a solar radiation pressure model, because it creates an important perturbation force on GEO satellites with such large solar panels required for EP; a model of atmospheric perturbations, because a satellite in GTO may experience a considerable deceleration due to drag near perigee, and third-order Earth oblateness perturbations, because Gomez [2015] demonstrated that their effect is significant for high-precision optimization of Earth-based low-thrust trajectories. Moreover, the author recommends implementing NASA's AP9 radiation model to quantify the experienced radiation fluence by the spacecraft. Nonetheless, the experience with GMV's customers is that operators of all-electric satellites are generally not interested in minimizing the exposure to radiation because the improvements are too small and not worth the computational effort and the platform should be designed to withstand it in any case.

To increase HOSTEP's suitability for commercial applications, the author recommends implementing further operational constraints as a function of the platform specifications. For example, a maximum slew rate constraint can be implemented to limit the direction rate of change of the thrust vector. This may be based on the specification of the thruster assembly if it features a steering mechanism or on the maximum achievable slew rate of the Attitude Determination and Control System (ADCS) subsystem. Moreover, it is advised to limit the thrust capacity over time based on the depth of discharge of the batteries and the solar cell degradation over time, which could be based on empirical data or a radiation fluence model.

BIBLIOGRAPHY

Autrán-Cerqueira, J. (2016). Introduction to software engineering. Course AE4874 reader, GMV. Lecture notes.

Benson, D. A., Huntington, G. T., Thorvaldsen, T. P., and Rao, A. V. (2006). Direct trajectory optimization and costate estimation via an orthogonal collocation method. *Journal of Guidance, Control, and Dynamics*, 29(6):1435–1440.

Betts, J. T. (1994). Optimal interplanetary orbit transfers by direct transcription. *The Journal of the Astronautical Sciences*, 42(3):247–268.

Betts, J. T. (1998). Survey of numerical methods for trajectory optimization. *Journal of Guidance, Control, and Dynamics*, 21(2):193–207.

Betts, J. T. (2000). Very low-thrust trajectory optimization using a direct SQP method. *Journal of Computational and Applied Mathematics*, 120(1):27–40.

Betts, J. T. (2010). *Practical Methods for Optimal Control and Estimation Using Nonlinear Programming*. Society for Industrial and Applied Mathematics, 2nd edition.

Betts, J. T. (2015). Optimal low-thrust orbit transfers with eclipsing. *Optimal Control Applications and Methods*, 36(2):218–240.

Biscani, F., Izzo, D., and Yam, C. H. (2010). A global optimisation toolbox for massively parallel engineering optimisation. Available online <http://arxiv.org/abs/1004.3824>. Accessed on Feb 20th, 2017.

Boudestijn, E. (2014). Low-thrust Earth transfer optimizer. Master's thesis, Delft University of Technology.

Bryson, A. E. and Ho, Y.-C. (1975). *Applied Optimal Control*. CRC Press, 1st edition.

Byers, D. C. and Dankanich, J. W. (2008). Geosynchronous-Earth-Orbit communication satellite deliveries with integrated electric propulsion. *Journal of Propulsion and Power*, 24(6):1369–1375.

Corneliu, C., Stefanescu, R. M., Prioroc, C., Gil, J., and Lozano, A. (2015). Electric propulsion transfer optimization. In *25th International Symposium on Space Flight Dynamics*, pages 1–9.

Deb, K., Thiele, L., Laumanns, M., and Zitzler, E. (2002). Scalable multi-objective optimization test problems. In *2002 Congress on Evolutionary Computation*, volume 1, pages 825–830. IEEE.

Drinkwater, M. R., Haagmans, R., Muzi, D., Popescu, A., Floberghagen, R., Kern, M., and Fehringer, M. (2006). The GOCE gravity mission: ESA's first core Earth explorer. In *3rd International GOCE User Workshop*.

Duchemin, O. B., Caratge, A., Cornu, N., Sannino, J.-M., Lassoudière, F., , and Lorand, A. (2011). Ariane 5-ME and electric propulsion: GEO insertion options. *47th AIAA/ASME/SAE/ASEE Joint Propulsion Conference and Exhibit*.

Dunphy, R. (2014). Development of a robust trajectory optimisation tool. Master's thesis, Delft University of Technology.

Edelbaum, T. N. (1961). Propulsion requirements for controllable satellites. *ARS Journal*, 31(8):1079–1089.

EUTELSAT (2014). Eutelsat and SES settle their dispute and conclude a series of agreements concerning the 28.5 degrees East orbital position. Available online: http://http://www.eutelsat.com. Press release. Accessed on 25 June, 2017.

Falck, R. D. and Dankanich, J. (2012). Optimization of low-thrust spiral trajectories by collocation. In *AIAA/AAS Astrodynamics Specialist Conference*.

Feuerborn, S. A., Perkins, J., and Neary, D. A. (2013). Finding a way: Boeing's all electric propulsion satellite. In *49th AIAA/ASME/SAE/ASEE Joint Propulsion Conference and Exhibit*, page 4126.

Fox, L. P. et al. (1968). Chebyshev polynomials in numerical analysis. Technical report, Oxford University Press.

Gao, Y. and Kluever, C. A. (2004). Low-thrust interplanetary orbit transfers using hybrid trajectory optimization method with multiple shooting. In *AIAA/AAS Astrodynamics Specialist Conference*, pages 2004–5088.

Gao, Y. and Kluever, C. A. (2005). Analytical orbital averaging technique for computing tangential- thrust trajectories. *Journal of Guidance, Control, and Dynamics*, 28(6):1320–1323.

Gebbett, W. (2014). Multi-revolution, low-thrust trajectory design using Lyapunov feedback control. Master's thesis, Delft University of Technology.

Geffroy, S. and Epenoy, R. (1997). Optimal low-thrust transfers with constraints—generalization of averaging techniques. *Acta Astronautica*, 41(3):133–149.

Gil-Fernandez, J. and Gomez-Tierno, M. A. (2010). Practical method for optimization of low-thrust transfers. *Journal of Guidance, Control, and Dynamics*, 33(6):1927–1931.

Gill, E. and Montenbruck, O. (2000). *Satellite Orbits Models, Methods, and Applications*. Springer, 1st edition.

GMV (2006). FocusSuite - A Unique Product Line for All Flight Dynamics Needs. Available online <`www.gmv.com/DocumentosPDF/focusSuite/ficha_focus_suite.pdf`>. Accessed on May 10th, 2017.

Gomez, M. (2015). Optimization of low-thrust trajectories in Earth-centered orbit. Master's thesis, Delft University of Technology.

Gondelach, D. and Noomen, R. (2015). Hodographic-shaping method for low-thrust interplanetary trajectory design. *Journal of Spacecraft and Rockets*, 52(3):728–738.

Hintz, G. R. (2008). Survey of orbit element sets. *Journal of Guidance, Control, and Dynamics*, 31(3):785–789.

Holland, J. H. (1975). Adaption in natural and artificial systems: an introductory analysis with applications to biology, control, and artificial intelligence. *The MIT Press*.

Hoving, L. (2015). Optimisation strategies for Galilean moon tours. Master's thesis, Delft University of Technology.

Hudson, J. S. and Scheeres, D. J. (2009). Reduction of low-thrust continuous controls for trajectory dynamics. *Journal of Guidance, Control, and Dynamics*, 32(3):780–787.

Hudson, J. S. and Scheeres, D. J. (2011). Orbital targeting using reduced eccentric anomaly low-thrust coefficients. *Journal of Guidance, Control, and Dynamics*, 34(3):820–831.

Izzo, D., Ruciński, M., and Biscani, F. (2012). The generalized island model. *Parallel Architectures and Bioinspired Algorithms*, pages 151–169.

Jiang, F., Baoyin, H., and Li, J. (2012). Practical techniques for low-thrust trajectory optimization with homotopic approach. *Journal of Guidance, Control, and Dynamics*, 35(1):245–258.

Jimenez-Lluva, D. (2016). Improving the a priori solution in low-thrust trajectory optimization. Literature study, Delft University of Technology.

Kechichian, J. A. (2000). Minimum-time constant acceleration orbit transfer with first-order oblateness effect. *Journal of Guidance Control and Dynamics*, 23(4):595–603.

Kluever, C. A. (2004). Geostationary orbit transfers using solar electric propulsion with specific impulse modulation. *Journal of Spacecraft and Rockets*, 41(3):461–466.

Kluever, C. A. (2010). Low-thrust trajectory optimization using orbital averaging and control parameterization. In *Spacecraft Trajectory Optimization*. Cambridge University Press, 1st edition.

Kluever, C. A. and Pierson, B. L. (1995). Optimal low-thrust three-dimensional earth-moon trajectories. *Journal of Guidance, Control, and Dynamics*, 18(4):830–837.

Klukas, S. (2015). Investigation of the influence of different space propulsion systems on the propulsion requirements of satellite missions. Bachelor thesis, RWTH Aachen University.

Ko, H. C. and Scheeres, D. J. (2014). Essential thrust-fourier-coefficient set of averaged gauss equations for orbital mechanics. *Journal of Guidance, Control, and Dynamics*, 37(4):1236–1249.

Koppel, C. and Estublier, D. (2003). The Smart-1 electric propulsion subsystem. In *39th AIAA/ASME/SAE/ASEE Joint Propulsion Conference and Exhibit*.

Kuhn, H. W. and Tucker, A. W. (2013). Nonlinear programming. In *2nd Berkeley Symposium*, pages 481–492.

L. S. Pontryagin et al (1964). *The Mathematical Theory of Optimal Processes.* Pergamon Press Ltd.

Mason, J. C. and Handscomb, D. C. (2002). *Chebyshev polynomials.* CRC Press.

McConnell, S. (1996). Software quality at top speed. *Journal of Software Development*, 4(8):38–42.

Montealegre-Avila, P. J. (2015). Algorithm analysis for operational implementation of GEO transfer orbits using EP. Master's thesis, Universidad Politecnica de Madrid.

NASA (2015). Dawn spacecraft and instruments. Available online <http://www.nasa.gov/mission_pages/dawn/spacecraft/index.html>. Accessed on 12 June, 2016.

Nishiyama, K. and Kuninaka, H. (2012). Discussion on performance history and operations of Hayabusa ion engines. *Transactions of the Japan Society for Aeronautical and Space Sciences, Aerospace Technology Japan*, 10(28):1–8.

Pontryagin, L. S. (1986). *Mathematical Theory of Optimal Processes.* CRC Press.

Rayman, M. D., Chadbourne, P. A., Culwell, J. S., and Williams, S. N. (1999). Mission design for Deep Space 1: A low-thrust technology validation mission. *Acta Astronautica*, 45(4-9):381–388.

Roegiers, T. (2014). Application of the spherical shaping method to a low-thrust multiple asteroid rendezvous mission. Master's thesis, Delft University of Technology.

Sabbadini, M., Saccoccia, G., and Buoso, M. (2002). Electric propulsion technology programmes. Brochure by ESA.

Sackett, L. L., Malchow, H. L., and Edelbaum, T. N. (1975). Solar electric geocentric transfer with attitude constraints: Analysis. Technical report, National Aeronautics and Space Administration.

Sanchez, J. M. and Campa, A. (2014). Automation of multi-revolution low-thrust transfer optimization via differential evolution. *American Astronautical Society*, 14(311):1–20.

SpaceX (2015). Falcon 9 Launch Vehicle – Payload User's Guide, Rev. 2.

Steward, J. (2003). *Calculus: Early Transcendentals.* Thomson/Brooks/Cole, 5th edition.

Storn, R. and Price, K. (1997). Differential evolution – a simple and efficient heuristic for global optimization over continuous spaces. *Journal of Global Optimization*, 11(4):341–359.

Taheri, E. and Abdelkhalik, O. (2016). Initial three-dimensional low-thrust trajectory design. *Advances in Space Research*, 57(3):889–903.

Vallado, D. A. (1997). *Fundamentals of Astrodynamics and Applications.* McGraw Hill, 1st edition.

Wahde, M. (2008). *Biologically Inspired Optimization Methods: An Introduction.* WIT Press, 1st edition.

Wakker, K. (2010). Fundamentals of astrodynamics. Course AE4874 reader, Delft University of Technology.

Walker, M. J. H. (1986). Erratum - a set of modified equinoctial orbit elements. *Celestial Mechanics*, 38(4):391–392.

Walker, M. J. H., Ireland, B., and Owens, J. (1985). A set of modified equinoctial orbit elements. *Celestial Mechanics*, 36(1):409–419.

Wang, F. S. (2010). Differential Evolution implementation in Fortran 90, National Chung Cheng University. http://www1.icsi.berkeley.edu/ storn/DE_FORTRAN90.f90>. Accessed on Feb 27th, 2017.

Wei, P. and Changhou, L. (2011). Direct optimization of low-thrust transfers using averaging techniques based on Fourier series expansion. In *4th International Joint Conference on Computational Sciences and Optimization*, pages 46–50.

Wertz, J. R. (2009). *Mission Geometry: Orbit and Constellation Design and Management: Spacecraft Orbit and Attitude Systems.* Space technology library. Springer, 2nd edition.

Zhu, J. (1994). Conversion of Earth-centered Earth-fixed coordinates to geodetic coordinates. *IEEE Transactions on Aerospace and Electronic Systems*, 30(3):957–961.

A

ANALYTICAL OCP DERIVATION

This Appendix provides a thorough explanation of how the optimal control laws were derived from the Hamiltonian equation. These derivations follow from optimal control theory, which is described in the literature study report that precedes this thesis [Jimenez-Lluva, 2016] and more thoroughly explained in well established books such as [Bryson and Ho, 1975; Pontryagin, 1986]. As explained in subsection 2.4.1, the Hamiltonian of the OCP is as follows:

$$\mathcal{H} = \lambda_p \frac{dp}{dt} + \lambda_f \frac{df}{dt} + \lambda_g \frac{dg}{dt} + \lambda_j \frac{dj}{dt} + \lambda_k \frac{dk}{dt} + \lambda_m \frac{dm}{dt} \tag{A.1}$$

which can be expanded by substituting the EOM, Equation 2.17 to Equation 2.21, from section 2.2:

$$
\begin{aligned}
\mathcal{H} = {} & \lambda_p \frac{2p}{w} \sqrt{\frac{p}{\mu}} \cos\alpha \cos\beta \frac{T}{m} \\
& + \lambda_f \sqrt{\frac{p}{\mu}} \left[\sin L \sin\alpha \cos\beta + \frac{1}{w} \left[(w+1)\cos L + f \right] \cos\alpha \cos\beta - \frac{g}{w} \left(j \sin L - k \cos L \right] \sin\beta \right) \frac{T}{m} \\
& + \lambda_g \sqrt{\frac{p}{\mu}} \left[-\cos L \sin\alpha \cos\beta + \frac{1}{w} \left[(w+1)\sin L + g \right] \cos\alpha \cos\beta + \frac{f}{w} \left(j \sin L - k \cos L \right] \sin\beta \right) \frac{T}{m} \\
& + \lambda_j \sqrt{\frac{p}{\mu}} \frac{s^2 \cos L}{2w} \sin\beta \frac{T}{m} + \lambda_k \sqrt{\frac{p}{\mu}} \frac{s^2 \sin L}{2w} \sin\beta \frac{T}{m} - \lambda_m \frac{T}{g_0 I_{sp}}
\end{aligned}
\tag{A.2}
$$

It should be noted that the EOM substituted above only feature the contribution of the thrust force. Should one desire to include orbital perturbation terms in the EOM, the result of the upcoming derivations would remain unaffected. This is because these additional terms are not a function of the control parameters and would disappear in the differentiation process.

The first order optimality conditions, also known as the Karush-Kuhn-Tucher (KKT) conditions, state that the first derivative of the Hamiltonian with respect to the control variables – T, α, and β – must be zero at a singular point [Kuhn and Tucker, 2013]. Additionally, the Legendre-Clebsch (LC) condition states that the second derivative must be positive for an minimum solution [Bryson and Ho, 1975]. The optimal control law thus entails three derivations: the optimal yaw and pitch steering angles, as well as the optimal thrust magnitude.

A.1. OPTIMAL THRUST YAW STEERING ANGLE

To begin with, the KKT condition is applied to the first order Hamiltonian derivative with respect to α:

$$
\begin{aligned}
\frac{\partial \mathcal{H}}{\partial \alpha} = {} & -\lambda_p \frac{2p}{w} \sqrt{\frac{\not{p}}{\mu}} \sin\alpha \cancel{\cos\beta} \frac{\cancel{T}}{\cancel{m}} + \lambda_f \sqrt{\frac{\not{p}}{\mu}} \left[\sin L \cos\alpha \cancel{\cos\beta} - \frac{1}{w} \left[(w+1)\cos L + f \right] \sin\alpha \cancel{\cos\beta} \right] \frac{\cancel{T}}{\cancel{m}} \\
& + \lambda_g \sqrt{\frac{\not{p}}{\mu}} \left[-\cos L \cos\alpha \cancel{\cos\beta} - \frac{1}{w} \left[(w+1)\sin L + g \right] \sin\alpha \cancel{\cos\beta} \right] \frac{\cancel{T}}{\cancel{m}} = 0
\end{aligned}
\tag{A.3}
$$

63

where the constant terms may be replaced by the following auxiliary variables:

$$\Lambda_p^\alpha = \lambda_p \frac{2p}{w} \tag{A.4}$$

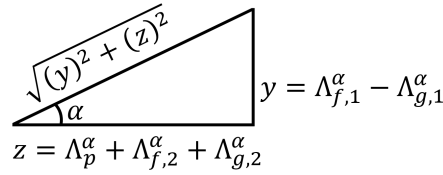$$\Lambda_{f,1}^\alpha = \lambda_f \sin L \qquad\qquad \Lambda_{g,1}^\alpha = \lambda_g \cos L \tag{A.5}$$

$$\Lambda_{f,2}^\alpha = \lambda_f \frac{\left[(w+1)\cos L + f\right]}{w} \qquad\qquad \Lambda_{g,2}^\alpha = \lambda_g \frac{\left[(w+1)\sin L + g\right]}{w} \tag{A.6}$$

Dividing both sides of Equation A.3 by $\cos\alpha$ and rearranging yields:

$$\tan\alpha = \frac{\lambda_f \sin L - \lambda_g \cos L}{\lambda_p \frac{2p}{w} + \lambda_f \frac{1}{w}\left[(w+1)\cos L + f\right] + \lambda_g \frac{1}{w}\left[(w+1)\sin L + g\right]} = \frac{\Lambda_{f,1}^\alpha - \Lambda_{g,1}^\alpha}{\Lambda_p^\alpha + \Lambda_{f,2}^\alpha + \Lambda_{g,2}^\alpha} \tag{A.7}$$

From the trigonometric definition of the tangent in a triangle, the following may be concluded:

Figure A.1: Trigonometric relationship.

$$\sin\alpha = \pm \frac{\Lambda_{f,1}^\alpha - \Lambda_{g,1}^\alpha}{\sqrt{\left[\Lambda_{f,1}^\alpha - \Lambda_{g,1}^\alpha\right]^2 + \left[\Lambda_p^\alpha + \Lambda_{f,2}^\alpha + \Lambda_{g,2}^\alpha\right]^2}} \tag{A.8}$$

$$\cos\alpha = \pm \frac{\Lambda_p^\alpha + \Lambda_{f,2}^\alpha + \Lambda_{g,2}^\alpha}{\sqrt{\left[\Lambda_{f,1}^\alpha - \Lambda_{g,1}^\alpha\right]^2 + \left[\Lambda_p^\alpha + \Lambda_{f,2}^\alpha + \Lambda_{g,2}^\alpha\right]^2}} \tag{A.9}$$

Additionally, the Legendre-Clebsch condition states that the second order derivative of the Hamiltonian must be positive [Pontryagin, 1986] to guarantee that the solution is a minimum point:

$$\frac{\partial^2\mathcal{H}}{\partial\alpha^2} = -\Lambda_p^\alpha \cos\alpha - \Lambda_{f,1}^\alpha \sin\alpha - \Lambda_{f,2}^\alpha \cos\alpha + \Lambda_{g,1}^\alpha \sin\alpha - \Lambda_{g,2}^\alpha \cos\alpha > 0 \tag{A.10}$$

First, the positive alternative of Equation A.9 is substituted in Equation A.10:

$$\frac{\partial^2\mathcal{H}}{\partial\alpha^2} = -\Lambda_p^\alpha \frac{\Lambda_p^\alpha + \Lambda_{f,2}^\alpha + \Lambda_{g,2}^\alpha}{\sqrt{\left[\Lambda_{f,1}^\alpha - \Lambda_{g,1}^\alpha\right]^2 + \left[\Lambda_p^\alpha + \Lambda_{f,2}^\alpha + \Lambda_{g,2}^\alpha\right]^2}} - \Lambda_{f,1}^\alpha \frac{\Lambda_{f,1}^\alpha - \Lambda_{g,1}^\alpha}{\sqrt{\left[\Lambda_{f,1}^\alpha - \Lambda_{g,1}^\alpha\right]^2 + \left[\Lambda_p^\alpha + \Lambda_{f,2}^\alpha + \Lambda_{g,2}^\alpha\right]^2}}$$

$$- \Lambda_{f,2}^\alpha \frac{\Lambda_p^\alpha + \Lambda_{f,2}^\alpha + \Lambda_{g,2}^\alpha}{\sqrt{\left[\Lambda_{f,1}^\alpha - \Lambda_{g,1}^\alpha\right]^2 + \left[\Lambda_p^\alpha + \Lambda_{f,2}^\alpha + \Lambda_{g,2}^\alpha\right]^2}} + \Lambda_{g,1}^\alpha \frac{\Lambda_{f,1}^\alpha - \Lambda_{g,1}^\alpha}{\sqrt{\left[\Lambda_{f,1}^\alpha - \Lambda_{g,1}^\alpha\right]^2 + \left[\Lambda_p^\alpha + \Lambda_{f,2}^\alpha + \Lambda_{g,2}^\alpha\right]^2}}$$

$$- \Lambda_{g,2}^\alpha \frac{\Lambda_p^\alpha + \Lambda_{f,2}^\alpha + \Lambda_{g,2}^\alpha}{\sqrt{\left[\Lambda_{f,1}^\alpha - \Lambda_{g,1}^\alpha\right]^2 + \left[\Lambda_p^\alpha + \Lambda_{f,2}^\alpha + \Lambda_{g,2}^\alpha\right]^2}} > 0 \tag{A.11}$$

$$\frac{\partial^2\mathcal{H}}{\partial\alpha^2} = -\left(\left(\Lambda_p^\alpha\right)^2 + \Lambda_p^\alpha \Lambda_{f,2}^\alpha + \Lambda_p^\alpha \Lambda_{g,2}^\alpha\right) - \left(\left(\Lambda_{f,1}^\alpha\right)^2 - \Lambda_{f,1}^\alpha \Lambda_{g,1}^\alpha\right) - \left(\Lambda_p^\alpha \Lambda_{f,2}^\alpha + \left(\Lambda_{f,2}^\alpha\right)^2 + \Lambda_{f,2}^\alpha \Lambda_{g,2}^\alpha\right)$$

$$+ \left(\Lambda_{f,1}^\alpha \Lambda_{g,1}^\alpha - \left(\Lambda_{g,1}^\alpha\right)^2\right) - \left(\Lambda_p^\alpha \Lambda_{g,2}^\alpha + \Lambda_{f,2}^\alpha \Lambda_{g,2}^\alpha + \left(\Lambda_{g,2}^\alpha\right)^2\right) > 0 \tag{A.12}$$

$$\frac{\partial^2\mathcal{H}}{\partial\alpha^2} = -\left(\Lambda_p^\alpha + \Lambda_p^\alpha \Lambda_{f,2}^\alpha + \Lambda_p^\alpha \Lambda_{g,2}^\alpha\right)^2 - \left(\Lambda_{f,1}^\alpha - \Lambda_{f,1}^\alpha \Lambda_{g,1}^\alpha\right)^2 > 0 \tag{A.13}$$

which cannot be true since the square of any sum of numbers is always positive. Conversely, substituting the

negative alternative of Equation A.9 in Equation A.10 and following the same steps yields the following:

$$\left(\Lambda_p^\alpha + \Lambda_p^\alpha \Lambda_{f,2}^\alpha + \Lambda_p^\alpha \Lambda_{g,2}^\alpha\right)^2 + \left(\Lambda_{f,1}^\alpha - \Lambda_{f,1}^\alpha \Lambda_{g,1}^\alpha\right)^2 > 0 \tag{A.14}$$

which always satisfies the Legendre-Clebsch condition. Therefore, the optimal yaw steering is defined by:

$$\sin\alpha = -\frac{\Lambda_{f,1}^\alpha - \Lambda_{g,1}^\alpha}{\sqrt{\left[\Lambda_{f,1}^\alpha - \Lambda_{g,1}^\alpha\right]^2 + \left[\Lambda_p^\alpha + \Lambda_{f,2}^\alpha + \Lambda_{g,2}^\alpha\right]^2}} \tag{A.15}$$

$$\cos\alpha = -\frac{\Lambda_p^\alpha + \Lambda_{f,2}^\alpha + \Lambda_{g,2}^\alpha}{\sqrt{\left[\Lambda_{f,1}^\alpha - \Lambda_{g,1}^\alpha\right]^2 + \left[\Lambda_p^\alpha + \Lambda_{f,2}^\alpha + \Lambda_{g,2}^\alpha\right]^2}} \tag{A.16}$$

Although unnecessary, the yaw steering angle can be calculated using the relationship $\alpha = \text{atan2}\left(\sin\alpha, \cos\alpha\right)$, because the steering angles range from $-90°$ to $90°$. It is worth recalling that the thrust vector is defined as $\boldsymbol{u}_{RSW} = a_T \left[\sin\alpha\cos\beta \quad \cos\alpha\cos\beta \quad \sin\beta\right]^T$, rendering this additional step inefficient.

A.2. Optimal Thrust Pitch Steering Angle

The KKT optimality conditions are now applied to calculate the optimal pitch steering angle β. The first derivative of the Hamiltonian with respect to beta is equated to zero and yields:

$$\frac{\partial\mathcal{H}}{\partial\beta} = 0 = -\lambda_p \frac{2p}{w}\sqrt{\frac{\cancel{p}}{\mu}}\cos\alpha\sin\beta^* \frac{\cancel{T}}{\cancel{m}}$$

$$+ \lambda_f \sqrt{\frac{\cancel{p}}{\mu}}\left[-\sin L\sin\alpha\sin\beta^* - \frac{1}{w}\left[(w+1)\cos L + f\right]\cos\alpha\sin\beta^* - \frac{g}{w}\left(j\sin L - k\cos L\right)\cos\beta^*\right]\frac{\cancel{T}}{\cancel{m}}$$

$$+ \lambda_g \sqrt{\frac{\cancel{p}}{\mu}}\left[\cos L\sin\alpha\sin\beta^* - \frac{1}{w}\left[(w+1)\sin L + g\right]\cos\alpha\sin\beta^* + \frac{f}{w}\left(j\sin L - k\cos L\right)\cos\beta^*\right]\frac{\cancel{T}}{\cancel{m}} \tag{A.17}$$

$$+ \lambda_j \sqrt{\frac{\cancel{p}}{\mu}}\frac{s^2\cos L}{2w}\cos\beta^* \frac{\cancel{T}}{\cancel{m}}$$

$$+ \lambda_k \sqrt{\frac{\cancel{p}}{\mu}}\frac{s^2\sin L}{2w}\cos\beta^* \frac{\cancel{T}}{\cancel{m}}$$

where $\alpha = \alpha^*$ is assumed and the constant terms may be replaced by the following auxiliary variables:

$$\Lambda_p^\beta = \lambda_p \sqrt{\frac{p}{\mu}}\frac{2p}{w}\cos\alpha^* \tag{A.18}$$

$$\Lambda_{f,1}^\beta = \lambda_f \sqrt{\frac{p}{\mu}}\sin L\sin\alpha^* \qquad\qquad \Lambda_{g,1}^\beta = \lambda_g \sqrt{\frac{p}{\mu}}\cos L\sin\alpha^* \tag{A.19}$$

$$\Lambda_{f,2}^\beta = \lambda_f \sqrt{\frac{p}{\mu}}\frac{1}{w}\left[(w+1)\cos L + f\right]\cos\alpha^* \qquad \Lambda_{g,2}^\beta = \lambda_g \sqrt{\frac{p}{\mu}}\frac{1}{w}\left[(w+1)\sin L + g\right]\cos\alpha^* \tag{A.20}$$

$$\Lambda_{f,3}^\beta = \lambda_f \sqrt{\frac{p}{\mu}}\frac{g}{w}\left(j\sin L - k\cos L\right) \qquad\qquad \Lambda_{g,3}^\beta = \lambda_g \sqrt{\frac{p}{\mu}}\frac{f}{w}\left(j\sin L - k\cos L\right) \tag{A.21}$$

$$\Lambda_j^\beta = \lambda_j \sqrt{\frac{p}{\mu}}\frac{s^2\cos L}{2w} \qquad\qquad \Lambda_k^\beta = \lambda_k \sqrt{\frac{p}{\mu}}\frac{s^2\sin L}{2w} \tag{A.22}$$

It should be clarified that the square root terms have not been removed here because these constant terms will be re-used later in the optimal thrust magnitude derivation, where the square root terms do not cancel out. Substituting these constants in Equation A.17, dividing by $\cos\beta$, and rearranging leads to:

$$\tan\beta^* = \frac{-\Lambda_{f,3}^{\beta} + \Lambda_{g,3}^{\beta} + \Lambda_{j}^{\beta} + \Lambda_{k}^{\beta}}{\Lambda_{p}^{\beta} + \Lambda_{f,1}^{\beta} + \Lambda_{f,2}^{\beta} - \Lambda_{g,1}^{\beta} + \Lambda_{g,2}^{\beta}} \tag{A.23}$$

Using the trigonometric relationship in Figure A.1, this implies the following potential solutions:

$$\sin\beta^* = \frac{\pm\left(-\Lambda_{f,3}^{\beta} + \Lambda_{g,3}^{\beta} + \Lambda_{j}^{\beta} + \Lambda_{k}^{\beta}\right)}{\sqrt{\left(-\Lambda_{f,3}^{\beta} + \Lambda_{g,3}^{\beta} + \Lambda_{j}^{\beta} + \Lambda_{k}^{\beta}\right)^2 + \left(\Lambda_{p}^{\beta} + \Lambda_{f,1}^{\beta} + \Lambda_{f,2}^{\beta} - \Lambda_{g,1}^{\beta} + \Lambda_{g,2}^{\beta}\right)^2}} \tag{A.24}$$

$$\cos\beta^* = \frac{\pm\left(\Lambda_{p}^{\beta} + \Lambda_{f,1}^{\beta} + \Lambda_{f,2}^{\beta} - \Lambda_{g,1}^{\beta} + \Lambda_{g,2}^{\beta}\right)}{\sqrt{\left(-\Lambda_{f,3}^{\beta} + \Lambda_{g,3}^{\beta} + \Lambda_{j}^{\beta} + \Lambda_{k}^{\beta}\right)^2 + \left(\Lambda_{p}^{\beta} + \Lambda_{f,1}^{\beta} + \Lambda_{f,2}^{\beta} - \Lambda_{g,1}^{\beta} + \Lambda_{g,2}^{\beta}\right)^2}} \tag{A.25}$$

To ensure a minimum solution, the second derivative must be positive:

$$\frac{\partial^2 \mathcal{H}}{\partial \beta^2} = -\Lambda_{p}^{\beta}\cos\beta^* - \Lambda_{f,1}^{\beta}\cos\beta^* - \Lambda_{f,2}^{\beta}\cos\beta^* + \Lambda_{f,3}^{\beta}\sin\beta^*$$
$$+ \Lambda_{g,1}^{\beta}\cos\beta^* - \Lambda_{g,2}^{\beta}\cos\beta^* - \Lambda_{g,3}^{\beta}\sin\beta^* - \Lambda_{j}^{\beta}\sin\beta^* - \Lambda_{k}^{\beta}\sin\beta^* > 0 \tag{A.26}$$

Substituting the positive variant of Equation A.24 and Equation A.25 in Equation A.26 and removing the common denominators yields:

$$\frac{\partial^2 \mathcal{H}}{\partial \beta^2} = -\Lambda_{p}^{\beta}\left(\Lambda_{p}^{\beta} + \Lambda_{f,1}^{\beta} + \Lambda_{f,2}^{\beta} - \Lambda_{g,1}^{\beta} + \Lambda_{g,2}^{\beta}\right) - \Lambda_{f,1}^{\beta}\left(\Lambda_{p}^{\beta} + \Lambda_{f,1}^{\beta} + \Lambda_{f,2}^{\beta} - \Lambda_{g,1}^{\beta} + \Lambda_{g,2}^{\beta}\right)$$
$$- \Lambda_{f,2}^{\beta}\left(\Lambda_{p}^{\beta} + \Lambda_{f,1}^{\beta} + \Lambda_{f,2}^{\beta} - \Lambda_{g,1}^{\beta} + \Lambda_{g,2}^{\beta}\right) + \Lambda_{f,3}^{\beta}\left(-\Lambda_{f,3}^{\beta} + \Lambda_{g,3}^{\beta} + \Lambda_{j}^{\beta} + \Lambda_{k}^{\beta}\right)$$
$$+ \Lambda_{g,1}^{\beta}\left(\Lambda_{p}^{\beta} + \Lambda_{f,1}^{\beta} + \Lambda_{f,2}^{\beta} - \Lambda_{g,1}^{\beta} + \Lambda_{g,2}^{\beta}\right) - \Lambda_{g,2}^{\beta}\left(\Lambda_{p}^{\beta} + \Lambda_{f,1}^{\beta} + \Lambda_{f,2}^{\beta} - \Lambda_{g,1}^{\beta} + \Lambda_{g,2}^{\beta}\right)$$
$$- \Lambda_{g,3}^{\beta}\left(-\Lambda_{f,3}^{\beta} + \Lambda_{g,3}^{\beta} + \Lambda_{j}^{\beta} + \Lambda_{k}^{\beta}\right) - \Lambda_{j}^{\beta}\left(-\Lambda_{f,3}^{\beta} + \Lambda_{g,3}^{\beta} + \Lambda_{j}^{\beta} + \Lambda_{k}^{\beta}\right)$$
$$- \Lambda_{k}^{\beta}\left(-\Lambda_{f,3}^{\beta} + \Lambda_{g,3}^{\beta} + \Lambda_{j}^{\beta} + \Lambda_{k}^{\beta}\right) > 0 \tag{A.27}$$

$$\frac{\partial^2 H}{\partial \beta^2} = -\left(\Lambda_{p}^{\beta} + \Lambda_{f,1}^{\beta} + \Lambda_{f,2}^{\beta} - \Lambda_{g,1}^{\beta} + \Lambda_{g,2}^{\beta}\right)^2 - \left(-\Lambda_{f,3}^{\beta} + \Lambda_{g,3}^{\beta} + \Lambda_{j}^{\beta} + \Lambda_{k}^{\beta}\right)^2 > 0 \tag{A.28}$$

which can never be satisfied because the sum of two squares is always positive. On the other hand, substituting the negative variant of Equation A.24 and Equation A.25 in Equation A.26 and simplifying yields:

$$\frac{\partial^2 \mathcal{H}}{\partial \beta^2} = \left(\Lambda_{p}^{\beta} + \Lambda_{f,1}^{\beta} + \Lambda_{f,2}^{\beta} - \Lambda_{g,1}^{\beta} + \Lambda_{g,2}^{\beta}\right)^2 + \left(-\Lambda_{f,3}^{\beta} + \Lambda_{g,3}^{\beta} + \Lambda_{j}^{\beta} + \Lambda_{k}^{\beta}\right)^2 > 0 \tag{A.29}$$

which always satisfies the KKT optimality condition. Therefore, the optimal thrust pitch steering is:

$$\sin\beta^* = \frac{\left(\Lambda_{f,3}^{\beta} - \Lambda_{g,3}^{\beta} - \Lambda_{j}^{\beta} - \Lambda_{k}^{\beta}\right)}{\sqrt{\left(-\Lambda_{f,3}^{\beta} + \Lambda_{g,3}^{\beta} + \Lambda_{j}^{\beta} + \Lambda_{k}^{\beta}\right)^2 + \left(\Lambda_{p}^{\beta} + \Lambda_{f,1}^{\beta} + \Lambda_{f,2}^{\beta} - \Lambda_{g,1}^{\beta} + \Lambda_{g,2}^{\beta}\right)^2}} \tag{A.30}$$

$$\cos\beta^* = \frac{\left(-\Lambda_{p}^{\beta} - \Lambda_{f,1}^{\beta} - \Lambda_{f,2}^{\beta} + \Lambda_{g,1}^{\beta} - \Lambda_{g,2}^{\beta}\right)}{\sqrt{\left(-\Lambda_{f,3}^{\beta} + \Lambda_{g,3}^{\beta} + \Lambda_{j}^{\beta} + \Lambda_{k}^{\beta}\right)^2 + \left(\Lambda_{p}^{\beta} + \Lambda_{f,1}^{\beta} + \Lambda_{f,2}^{\beta} - \Lambda_{g,1}^{\beta} + \Lambda_{g,2}^{\beta}\right)^2}} \tag{A.31}$$

A.3. OPTIMAL THRUST MAGNITUDE

The most promising strategy to accomplish this was identified in [Gao and Kluever, 2004] and the corresponding control law is derived below, using MEE instead of Keplerian elements.

$$\frac{\partial \mathcal{H}}{\partial T} = \lambda_p \sqrt{\frac{p}{\mu}} \frac{2p}{w} \cos\alpha \cos\beta \frac{1}{m}$$

$$+ \lambda_f \sqrt{\frac{p}{\mu}} \left[\sin L \sin\alpha \cos\beta + \frac{1}{w} \left[(w+1)\cos L + f \right] \cos\alpha \cos\beta - \frac{g}{w} \left(j\sin L - k\cos L \right) \sin\beta \right] \frac{1}{m} \qquad \text{(A.32)}$$

$$+ \lambda_g \sqrt{\frac{p}{\mu}} \left[-\cos L \sin\alpha \cos\beta + \frac{1}{w} \left[(w+1)\sin L + g \right] \cos\alpha \cos\beta + \frac{f}{w} \left(j\sin L - k\cos L \right) \sin\beta \right] \frac{1}{m}$$

$$+ \Lambda_j \sqrt{\frac{p}{\mu}} \frac{s^2 \cos L}{2w} \sin\beta \frac{1}{m} + \lambda_k \sqrt{\frac{p}{\mu}} \frac{s^2 \sin L}{2w} \sin\beta \frac{1}{m} - \lambda_m \frac{1}{g_0 I_{sp}}$$

$$\frac{\partial \mathcal{H}}{\partial T} = \Lambda_p^\beta \cos\beta \frac{1}{m} + \left[\Lambda_{f,1}^\beta \cos\beta + \Lambda_{f,2}^\beta \cos\beta - \Lambda_{f,3}^\beta \sin\beta \right] \frac{1}{m} \qquad \text{(A.33)}$$

$$+ \left[-\Lambda_{g,1}^\beta \cos\beta + \Lambda_{g,2}^\beta \cos\beta + \Lambda_{g,3}^\beta \sin\beta \right] \frac{1}{m} + \Lambda_j^\beta \sin\beta \frac{1}{m} + \Lambda_k^\beta \sin\beta \frac{1}{m} - \lambda_m \frac{1}{g_0 I_{sp}}$$

Since the Hamiltonian is linearly dependent on T, a switching function is defined by $S_t = \frac{\partial \mathcal{H}}{\partial T}$ is introduced to determine the optimal conditions. The problem may yield a bang-bang control with respect to control parameter T or it may yield a singular control problem if T can exhibit a value between the upper and lower bounds [Pontryagin, 1986]:

$$T = \begin{cases} T_{max}, & \text{if } S_t < 0 \\ 0, & \text{if } S_t > 0 \\ 0 < T < T_{max}, & \text{if } S_t = 0 \text{ and } \dot{S}_t = 0 \end{cases} \qquad \text{(A.34)}$$

The necessary conditions for a singular arc to exist are $S_t = 0$ and $\dot{S}_t = 0$ [Pontryagin, 1986], which is deemed infeasible due to the numeric nature of the simulation. Moreover, singular arcs show a very limited duration in practical application. Therefore, the author assumed a bang-bang control and neglected the potential third condition.

B

HOSTEP SOFTWARE TOOL

This chapter describes the software tool developed in this thesis project. First, the main program files are briefly described and the complete list of user options and input parameters is presented. Afterwards, the architecture of the program is elaborated, followed with the work-flow logic analysis.

B.1. ALGORITHM ARCHITECTURE

In accordance with software engineering policies of GMV, the HOSTEP software tool was programmed following a modular flow-down architecture. This architecture is show in Figure B.1. The reader should notice that this diagram does not portray the flow of operations but rather aims to illustrate the dependencies of each module. The operations flow and logic are illustrated in the next subsection through the work-flow diagram.
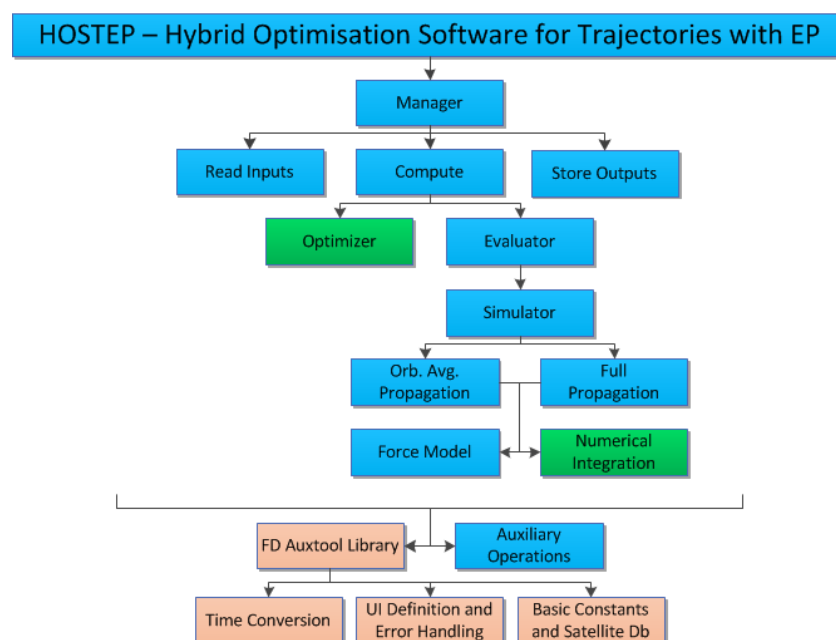
Figure B.1: HOSTEP algorithm architecture diagram.

The square boxes in Figure B.1 represent individual algorithm modules. Blue modules were developed from scratch by the author. Green modules were readily available and validated by GMV, with only moderate modifications being required from the author. Lastly, peach-coloured modules were GMV libraries that the author directly incorporated with almost no adjustments. Moreover, the two auxiliary libraries at the bottom that may appear detached from the rest of the diagram represent the lowest hierarchical level modules, which are used by almost all other modules of HOSTEP.

The main characteristic of such flow-down architecture is that the information of the intermediate parameter

values throughout the computations shall flow only in the downward direction, thus ensuring only downwards dependencies and no circular dependencies.

Moreover, the modular nature of the architecture is aimed at easing the potential adjustments throughout the development process as well as the complexity of debugging campaigns. For example, incorporating an additional orbital perturbation would require adjusting only the Force Model module.

B.2. ALGORITHM WORK-FLOW

Whereas the previous section described the modular software architecture and its corresponding dependencies, this section aims to provide an insight into the work-flow of the operations in HOSTEP. In Figure B.2 and Figure B.3, the square boxes describe an action, the rhombuses indicate the name of the module, and the arrow labels specify the name of the subroutine employed.
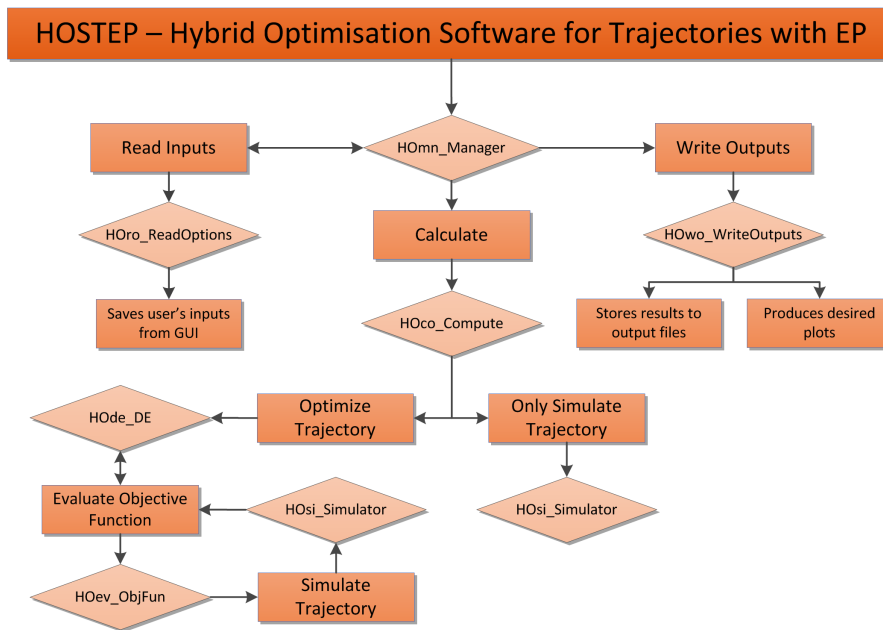

Figure B.2: HOSTEP algorithm overall work-flow diagram.

B.3. MAIN FILES

Upon every program execution there are several types of files that can be stored and later imported to reproduce a test case. These are the following:

- *tkf* and *nif* files: they define the GUI as well as the name, type, and description of all input parameters and options. Every panel of the GUI is described by a *nif* file, that generates the corresponding *dat* file.

- *dat* files: these files contain the information of the input parameters and options of the GUI. They serve as a means of storing the specifications of a certain test case, but are also necessary to feed the GUI inputs to the *HOro_ReadOptions* module of the program.

- *stdout* file: this constitutes the standard output of the program. It is the file where the program write the vital information such as execution messages, warnings, and errors. It may also contain information belonging to the individual sub-processes, the extent of which can be adjusted in the "Developer Options". For example, the user may desire to print the main inputs and outputs of the Orbital Averaging process and/or the intermediate information within the process. The latter may be resourceful for analyzing an ill-conditioned test case.

- *data* files: these contain propagation data stored upon each program execution. The specification of the data storage and its format is commanded by the *HOro_WriteOutput* module of the program.

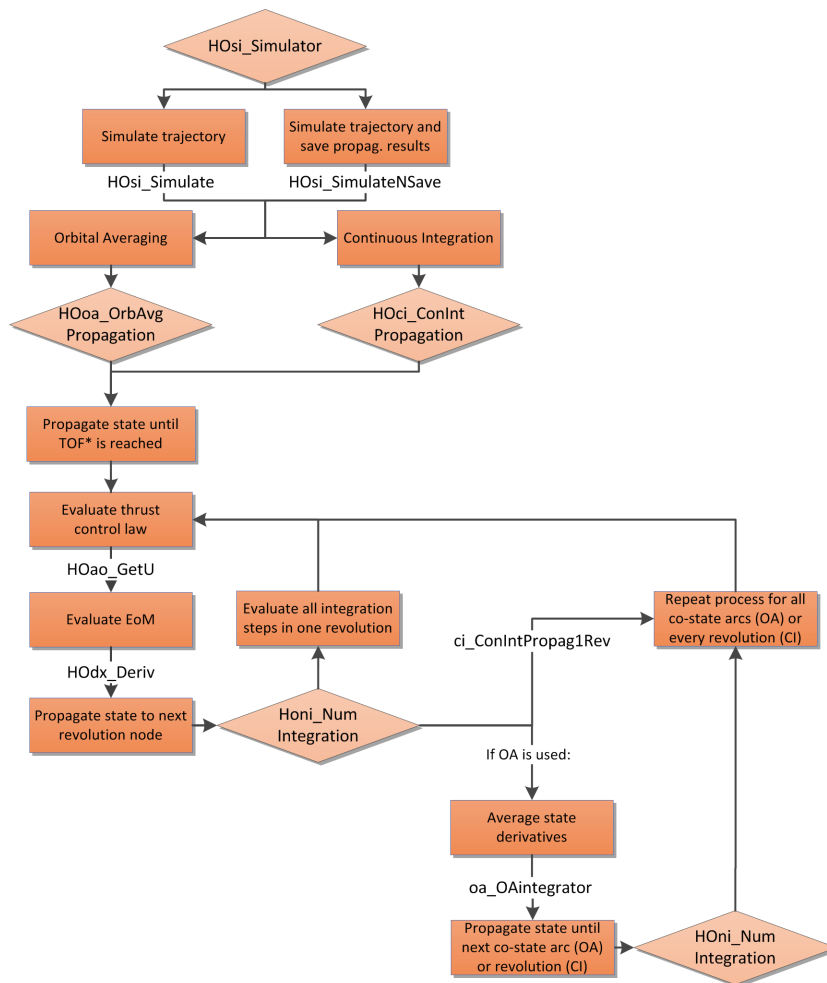- *plt* file: defines the data to be plotted in the graphs output tab, its formatting, and labels.

Figure B.3: HOSTEP algorithm simulation work-flow diagram.

- *cof* file: defines the GUI and commands the execution. Identifies the *nif* files that are to appear in the different tabs of the GUI, specifies the the *dat* files that store the corresponding information, and links the computational outputs to the *data* files where they are stored.

B.4. INPUT PARAMETERS, COMPUTATIONAL MODES, AND POST-PROCESSING OPTIONS

The GUI of HOSTEP features a broad range of input items such as parameters, computational modes, printing options, and post-processing options. These are all described in Table B.1 and Table B.1.

Table B.1: Explanation of HOSTEP input parameters and options.

Spacecraft Parameters	
Maximum thrust T [mN]	Specification of the spacecraft electric engine. Typically in the order $\mathcal{O}(10^2)$ mN for GEO satellites with full-EP.
Specific impulse I_{sp} [s]	Specification of the spacecraft electric engine. Typically in the order $\mathcal{O}(10^3)$ s for GEO satellites with full-EP.
Initial spacecraft mass m [kg]	Total mass of the spacecraft at the start of the trajectory. Typically in the order $\mathcal{O}(10^3)$ kg for GEO satellites.
Initial SV	Keplerian elements at the initial boundary condition of the OCP (Semi-major axis a [km], eccentricity e [-], inclination i [deg], arg. of perigee ω [deg], RAAN Ω [deg], true anomaly θ [deg])
Main Computational Options	
Computational mode	**Optimization** (optimizes a specified orbital transfer) / **Simulation** (simulates the orbital transfer of a specified design vector).
Input design vector source	**Manual input parameters** specified by the user / **Previous optimal results** from last stored optimization.
Variable thrust	**Off** (assumes continuous thrust outside of eclipse regions) / **On** (enables on/off switching of the engine).
Longitude targeting	**Off** (Disregards the terminal constraint of the geodetic longitude) / **On** (Takes into account the terminal constraint of the geodetic longitude in the objective function).
Number of co-state arcs	Number of equal-duration segments of trajectory. Each arc is defined by two boundary nodes where the system co-states (i.e. lambdas) are re-defined. Within the arc, these lambdas are linearly interpolated. Every additional node introduces a new set of co-states (i.e. 5 or 6 new optimization parameters for a minimum time-of-flight or minimum propellant mass problem).
Differential Evolution Options	
Initialization mode	**From random values** (evaluates random values within the user-specified boundaries) / **From previous optimized solution** (limits the search space based on previous design variables).
Number of DE repetitions	Number of times that the complete DE optimization process is repeated in a single execution.
Maximum number of iterations	Maximum allowed number of iterations per DE optimization. When reached, the optimization process automatically stops.
Print best results every X iterations	Every X iterations, the GUI shows the current residual and best solution so far, with its corresponding TOF, final SV, and co-states.
Max residual [-]	Maximum residual desired for the optimal solution. When the residual is below this value, the optimization automatically stops.
Population size N_P [D]	The population size is determined by an integer multiple of D, the number of optimization design parameters. A value of 10 is suggested in [Sanchez and Campa, 2014].
Scaling factor C_F [-]	Factor employed in the mutation stage. A value of 0.6 is suggested in [Sanchez and Campa, 2014].
Cross-over factor C_R [-]	Factor employed in the cross-over stage. A value of 0.8 is suggested in [Sanchez and Campa, 2014].
Upper-bound TOF $(t_f)_{ub}$ [days]	Maximum TOF value to be evaluated upon a random DE initialization.
Lower-bound TOF $(t_f)_{lb}$ [days]	Minimum TOF value to be evaluated upon a random DE initialization.
Upper-bound co-states λ_{ub} [-]	Maximum co-state value randomly to be evaluated upon a random DE initialization.
Lower-bound co-states λ_{lb} [-]	Minimum co-state value randomly to be evaluated upon a random DE initialization.
Multi-Objective Optimization Options	
Objective function weights [-]	Values that give relative priority to the optimization of the individual constituents of the objective function, see subsection 2.4.3.

Target orbit

Parameter	Description
Target SV	Desired Keplerian elements to be achieved by the orbital transfer, including the target geodetic longitude.
Maximum SV deviation	Maximum desired error between the target and final achieved Keplerian elements. The residual of the objective function increases quadratically when the error exceeds these values.

Propagation Options

Parameter	Description
N° integration steps per revolution	
OA averaging method	**Trapezoidal scheme / Simpson's scheme**. There is barely any noticeable change between them.
OA averaging variable	**True anomaly / Time**. The latter one is recommended due to slightly lower errors.
OA step-size [days]	Time interval after which the state derivative is re-evaluated. **A maximum value of 5.0 is suggested in [Kluever, 2010]**.
Integration scheme	Runge-Kutta-4 (RK4) is the only currently validated alternative.
Earth shadow simulation	**On** (overwrites thrust components equal to zero during eclipse) / **Off** (eclipses are disregarded).
Minimum solar flux threshold	Percentage of the solar flux in the fully illuminated conditions below which the Earth shadow simulation turns off the engine.
J_2 perturbation	**On** (adds the J_2 acceleration to the total disturbing acceleration in the RSW frame) / **Off** (J_2 accelerations are disregarded).
Altitude constraints	**On** (The propagator checks at every step that the constraint is not violated) / **Off** (The propagator does not check this constraint).
Minimum perigee altitude [km]	Specific value of the constraint.
Maximum apogee altitude [km]	Specific value of the constraint.

Developer Options

Parameter	Description
Execute unitary tests	**On** (prints the output of unitary tests in the GUI) / **Off**.
Propagate a single revolution	**On** (computes the orbital period of the starting semi-major axis and overwrites the TOF to this value) / **Off**.
Propagate for a specific TOF	**On** (overwrites the TOF to the following value) / **Off**.
Specific TOF [days]	Specific value to overwrite TOF.
Customized thrust profile	**Deactivated / tangential** (overwrites the thrust steering angles to $\sin\alpha^* = \sin\gamma$, $\cos\alpha^* = \cos\gamma$, $\sin\beta^* = 0.0$, $\cos\beta^* = 1.0$) / **out-of-plane** (overwrites the thrust steering angles to $\sin\alpha^* = \sin\gamma$, $\cos\alpha^* = \cos\gamma$, $\sin\beta^* = \sin\pm\pi$, $\cos\beta^* = \cos\pm\pi$) / **radial** (overwrites the thrust steering angles to $\sin\alpha^* = 1.0$, $\cos\alpha^* = 0.0$, $\sin\beta^* = 0.0$, $\cos\beta^* = 1.0$) / **zero thrust** (overwrites the thrust to zero).
Print intermediate information	Allows the user to print **main OA data, main CI data, inter-revolution OA data, or inter-revolution CI data.**

Post-Processing Options

Parameter	Description
Save propagation data	**On** (generates data files needed for plot generation) / **Off**.
Compare OA and CI propagation	**On** (applies both OA and CI to the optimized DV; evaluates the percentage error per orbital element; and creates two propagation data files to compare both methods in the plots) / **Off**.
Display coasting on graphs	**On** (creates a new CI propagation data file with data points corresponding to coasting arcs, including eclipses) / **Off**.
Display eclipse on graphs	**On** (creates a new CI propagation data file to display the entry and exit dates corresponding to Earth shadow regions) / **Off**.
Create eclipse summary file	**On** (creates a summary file displaying the entry and exit dates corresponding to Earth shadow regions) / **Off**.
Create LEOP manoeuvre file	**On** (creates a manoeuvre file that can be read by PROPAG, for validation or other purposes) / **Off**.
LEOP manoeuvre file step-size [s]	Increment in epoch when a new entry is added to the manoeuvre file. A value of 100.0 is suggested.
Create orbit file	**On** (creates an orbit file displaying the orbital elements at a given step-size that can be read by EVENTS) / **Off**.
Orbit file step-size [s]	Increment in epoch when a new entry is added to the orbit file. A value of 100.0 is suggested.

C

INPUTS AND OUTPUTS OF THE VALIDATION TESTS

The main inputs for Tests A1-A3 are shown below in Table C.1. Moreover, in the "Developer's options" tab of the GUI, the option to propagate for a user-specified TOF was ticked and the corresponding value was set to 20.0 days. Additionally, the thrust debugging option was set to tangential, out-of-plane, and radial thrusting for Tests A1, A2, and A3 respectively. The input vector of co-states is redundant because the algorithm overwrites the optimal steering angles. To produce the different OA approximations, the values of n_k and OA_{step} are manually adjusted upon every execution.

Table C.1: Inputs for the Test A1 trajectory.

Comp. mode	Simulation	DE mode	n/a	a_t [km]	n/a	$(\epsilon_a)_{ub}$ [km]	n/a
Var. thrust	Off	DV source	n/a	e_t [-]	n/a	$(\epsilon_e)_{ub}$ [-]	n/a
Long. target.	Off	DE_{rep} [-]	n/a	i_t [deg]	n/a	$(\epsilon_i)_{ub}$ [deg]	n/a
N_{arcs} [-]	1	N_{iter} [-]	n/a	ω_t [deg]	n/a	$(\epsilon_\omega)_{ub}$ [deg]	n/a
m_0 [kg]	2000.0	N_P [-]	n/a	Ω_t [deg]	n/a	$(\epsilon_\Omega)_{ub}$ [deg]	n/a
T [mN]	350.0	C_F [-]	n/a	Λ [deg]	n/a	$(\epsilon_\Lambda)_{ub}$ [deg]	n/a
I_{sp} [s]	2000.0	C_R [-]	n/a		n/a	W_t [-]	n/a
n_k [-]	40	$(t_f)_{ub}$ [day]	n/a	a_0 [km]	24505.9	W_a [-]	n/a
Propag. scheme	CI	$(t_f)_{lb}$ [day]	n/a	e_0 [-]	0.725	W_e [-]	n/a
OA_{step} [day]	4.0	λ_{ub} [-]	n/a	i_0 [deg]	7.0	W_i [-]	n/a
Avg. scheme	Trapez.	λ_{lb} [-]	n/a	ω_0 [deg]	1.0×10^{-12}	W_ω [-]	n/a
Avg. variable	Time			Ω_0 [deg]	1.0×10^{-12}	W_Ω [-]	n/a
Eclipse thr. [%]	Off	Launch		θ_0 [deg]	1.0×10^{-12}	W_m [-]	n/a
J_2 perturb. [-]	Off	date [UTC]	n/a			W_Λ [-]	n/a

The main inputs and options employed for Test B are shown below in Table C.3, and the design vector for this simulation is shown in Table C.2.

Table C.2: Design vector employed for the simulation in Test B.

t_f [days]	Node #	λ_p [-]	λ_f [-]	λ_g [-]	λ_j [-]	λ_k [-]
218.000	1	-0.021195	-38.677447	42.482983	499.322515	-67.364508
	2	-0.000078	24.905070	2.186083	499.380629	43.545684

Table C.3: Inputs for the Test B trajectory.

Comp. mode	Simulation	DE mode	n/a	a_t [km]	n/a	$(\epsilon_a)_{ub}$ [km]	n/a
Var. thrust	Off	DV source	n/a	e_t [-]	n/a	$(\epsilon_e)_{ub}$ [-]	n/a
Long. target.	Off	DE_{rep} [-]	n/a	i_t [deg]	n/a	$(\epsilon_i)_{ub}$ [deg]	n/a
N_{arcs} [-]	1	N_{iter} [-]	n/a	ω_t [deg]	n/a	$(\epsilon_\omega)_{ub}$ [deg]	n/a
m_0 [kg]	1200.0	N_P [-]	n/a	Ω_t [deg]	n/a	$(\epsilon_\Omega)_{ub}$ [deg]	n/a
T [mN]	401.706	C_F [-]	n/a	Λ [deg]	n/a	$(\epsilon_\Lambda)_{ub}$ [deg]	n/a
I_{sp} [s]	3300.0	C_R [-]	n/a		n/a	W_t [-]	n/a
n_k [-]	30	$(t_f)_{ub}$ [day]	n/a	a_0 [km]	6927.0	W_a [-]	n/a
Propag. scheme	CI	$(t_f)_{lb}$ [day]	n/a	e_0 [-]	1.0×10^{-12}	W_e [-]	n/a
OA_{step} [day]	4.0	λ_{ub} [-]	n/a	i_0 [deg]	28.5	W_i [-]	n/a
Avg. scheme	Trapez.	λ_{lb} [-]	n/a	ω_0 [deg]	1.0×10^{-12}	W_ω [-]	n/a
Avg. variable	Time			Ω_0 [deg]	1.0×10^{-12}	W_Ω [-]	n/a
Eclipse thr. [%]	Off	Launch		θ_0 [deg]	1.0×10^{-12}	W_m [-]	n/a
J_2 perturb. [-]	Off	date [UTC]	n/a			W_Λ [-]	n/a

Figure C.1 shows the evolution of the Keplerian elements, propagated using CI for the J_2-perturbed trajectory in Test D. Note that, as expected, the J_2 effect has no secular effect on the elements a, e, i, and θ.
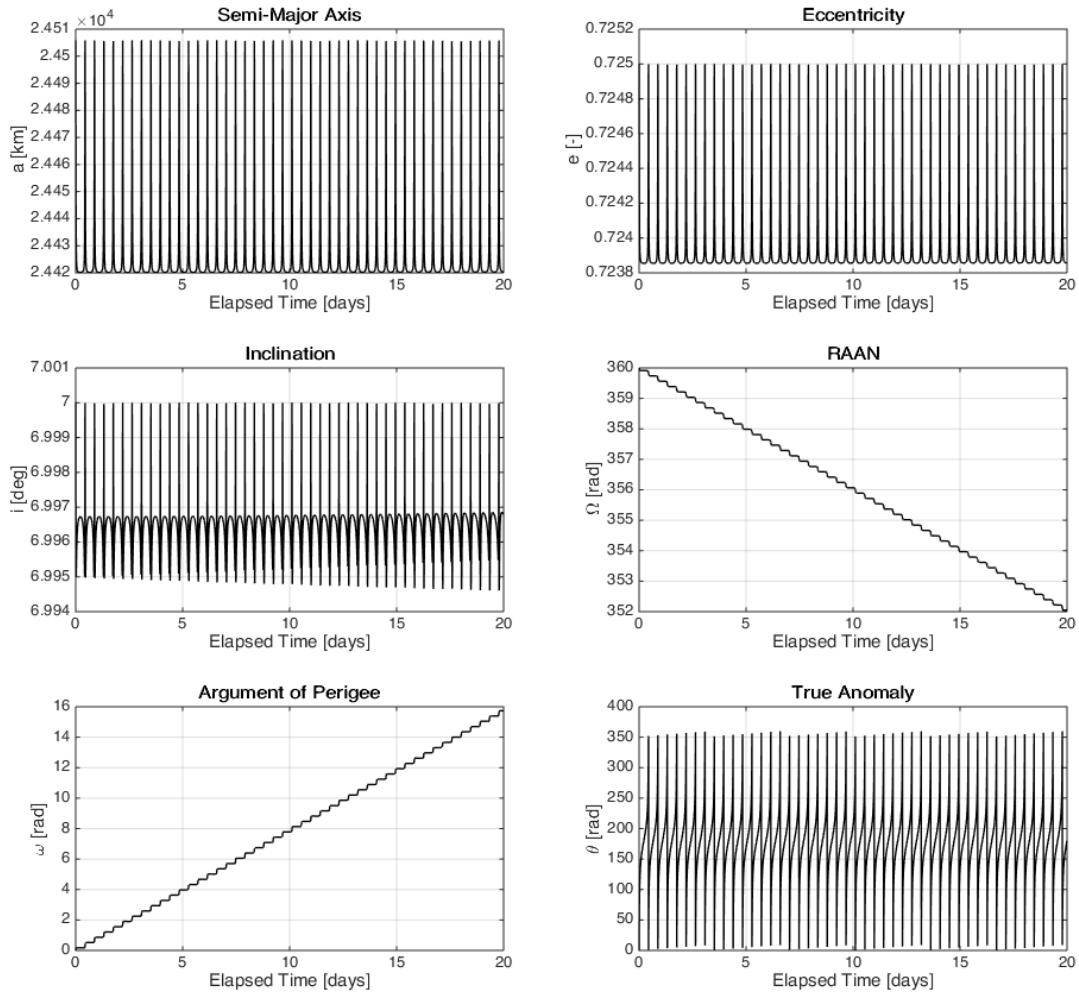
Figure C.1: Variation of the orbital elements due to the J_2 perturbing acceleration over a period of 20 days.

D

INPUTS AND OUTPUTS OF THE RESULT CASES

This appendix provides additional data about the results cases. For Case A1, the comparison between the CI and OA propagation of the four optimal trajectories is shown below in Table D.1 and Table D.2. Note that the large errors for the Ω and ω are to be expected due to the singularities of Keplerian elements when e and i approach zero values in the vicinity of GEO.

Table D.1: Comparison of the final CI and OA values for the Case A1 optimal trajectory.

State variable	Solution #1			Solution #2		
	CI result	OA result	OA error	CI result	OA result	OA error
Semi-major axis a [km]	42165.923	42067.391	-98.533	42164.580	42195.336	30.756
Eccentricity e [-]	2.309E-5	0.011	0.011	1.453E-5	0.011	0.011
Inclination i [deg]	1.263E-3	0.244	0.229	1.685E-3	0.208	0.229
RAAN Ω [deg]	308.022	184.321	-123.702	190.050	183.232	-6.818
Argument of perigee ω [deg]	6.131	177.674	171.544	314.267	176.242	-138.026
Total mass m [kg]	1786.186	1786.186	0.000	1787.301	1787.301	0.000

**Table D.2:** Comparison of the final CI and OA values for the Case A1 optimal trajectory.

State variable	Solution #3			Solution #4		
	CI result	OA result	OA error	CI result	OA result	OA error
Semi-major axis a [km]	42164.877	42140.375	-24.502	42164.684	42132.457	-32.227
Eccentricity e [-]	1.129E-4	0.011	0.011	5.278E-4	0.012	0.012
Inclination i [deg]	2.928E-3	0.134	0.115	2.590E-4	0.161	0.172
RAAN Ω [deg]	243.163	176.356	-66.807	359.932	179.221	-180.711
Argument of perigee ω [deg]	132.697	179.107	46.467	0.11459	180.081	179.966
Total mass m [kg]	1787.632	1787.632	0.000	1788.086	1788.086	0.000

Furthermore, the convergence of the four solutions from HOSTEP for Case A1 is illustrated below in Figure D.1, where the residual range is zoomed in for three different ranges of iteration numbers.
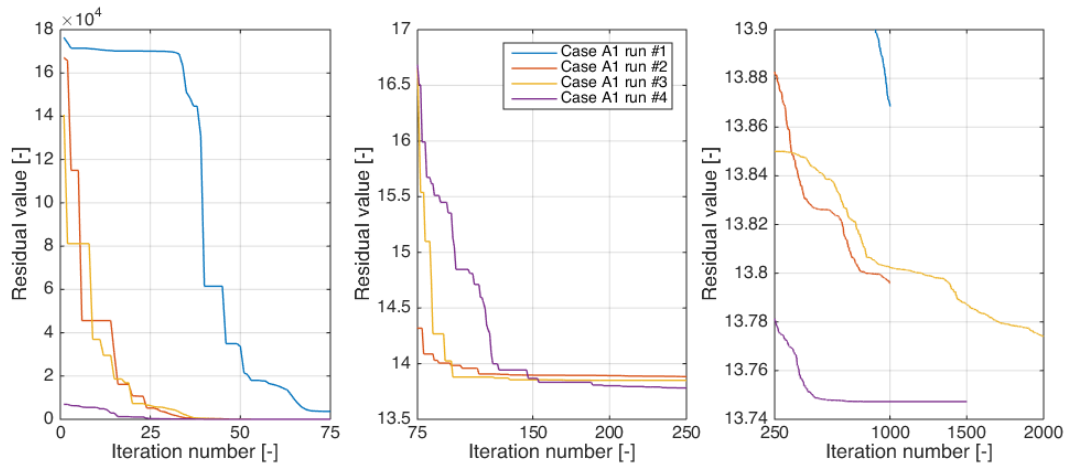
Figure D.1: Convergence of the 4 DE executions for Case A1, zoomed-in for three different ranges of iteration numbers.

Figure D.2 shows the comparison of HOSTEP's optimal solution for the unperturbed and J_2-perturbed GTO-GEO trajectories from Case A1 and Case A2 respectively. Note that the only difference is a slight variation in the evolution of the inclination.
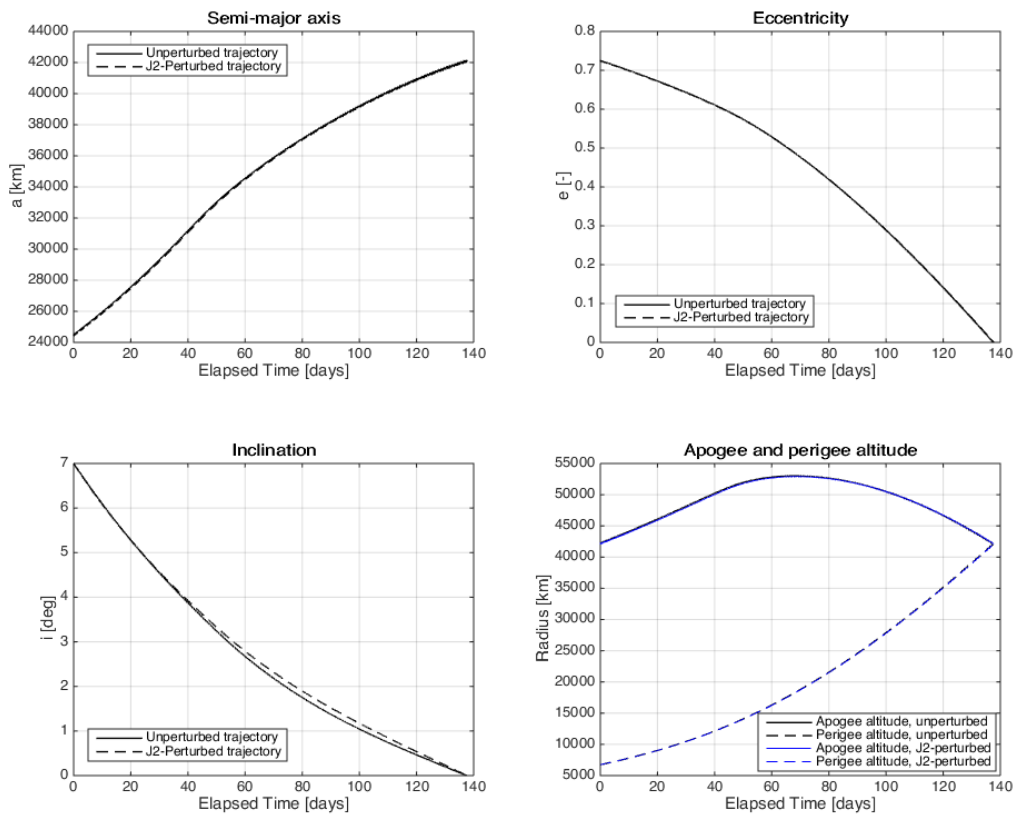
Figure D.2: Comparison evolution of the main Keplerian elements – (a) semi-major axis, (b) eccentricity, (c) inclination, and (d) apogee and perigee altitude – for the optimal Case A1, i.e. unperturbed, and Case A2, i.e. J_2-perturbed, trajectories computed with HOSTEP.
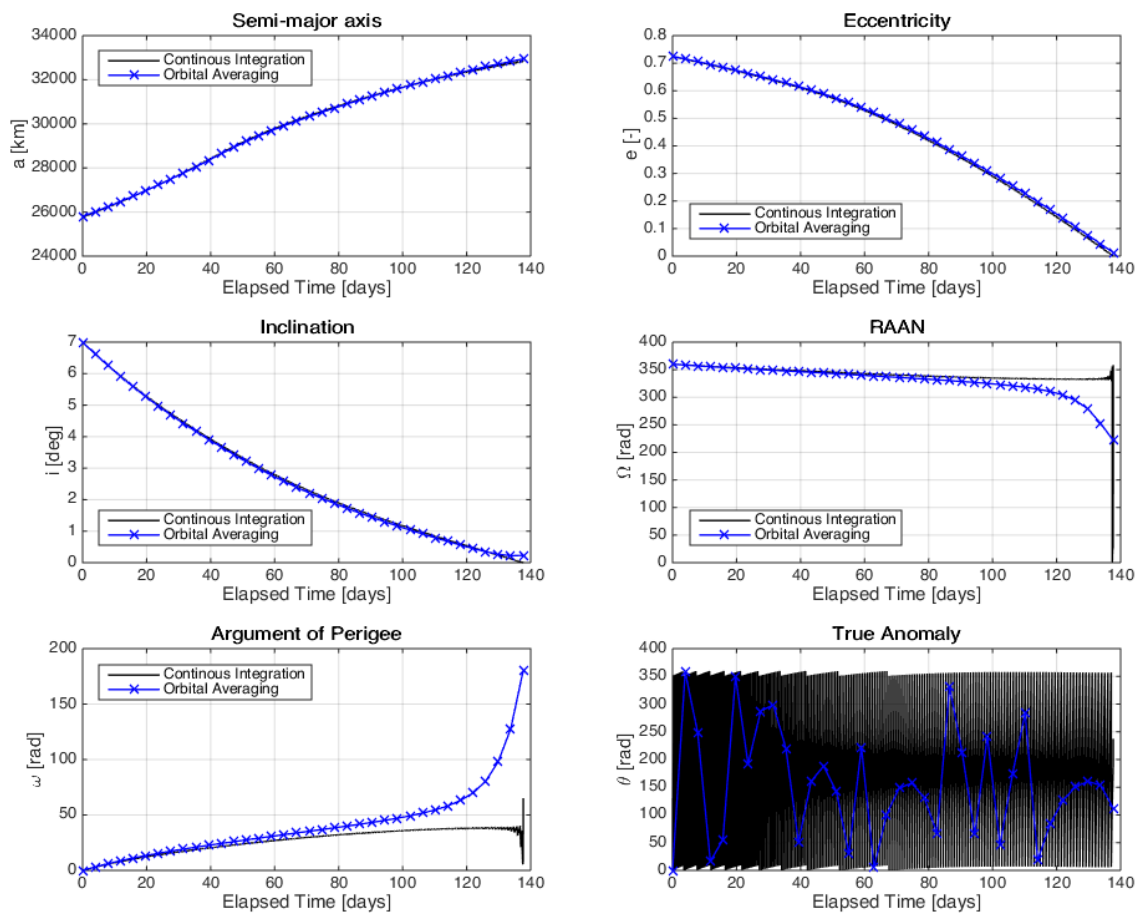
Table D.3 shows the comparison between the CI and OA propagation of the HOSTEP's optimal trajectory for Case A2.

Table D.3: CI and OA results for the simulation of the optimal Case A2 trajectory computed with HOSTEP.
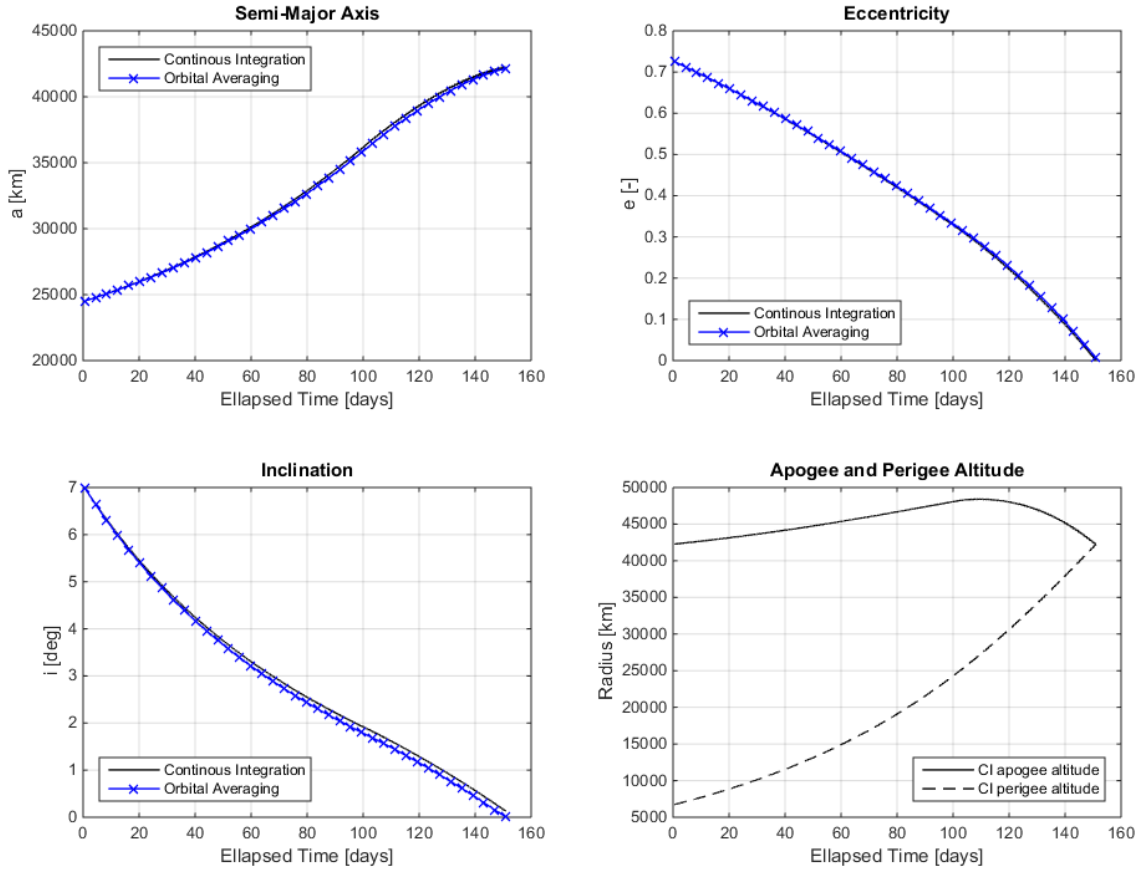
Keplerian element	CI	OA	OA error
Semi-major axis a [km]	42161.18	42159.36	-1.823
Eccentricity e [-]	2.54E-4	7.07E-3	0.007
Inclination i [deg]	0.129	0.005	-0.124
RAAN Ω [deg]	359.681	132.682	-226.998
Argument of perigee ω [deg]	345.010	227.899	-117.112
True anomaly θ [deg]	122.264	110.440	-11.825
Total mass m [kg]	1806.02	1805.71	-0.312

Figure D.4 shows the evolution of all Keplerian elements, propagated using CI and OA for the J_2-perturbed GTO-GEO trajectory calculated with HOSTEP for Case A2. Note that the RAAN remains close to 2π rad. Additionally, it is important to notice that the divergence in Ω and ω is caused by the singularities of Keplerian elements near GEO.

Figure D.3: Evolution of the main Keplerian elements for the J_2-perturbed GTO-GEO trajectory computed with HOSTEP for Case A2.

Figure D.4 shows the evolution of the Keplerian elements, propagated using CI and OA for the 150-days minimum-propellant trajectory calculated with HOSTEP for Case B. Additionally, Table D.4 shows the comparison between the CI and OA terminal propagation values.
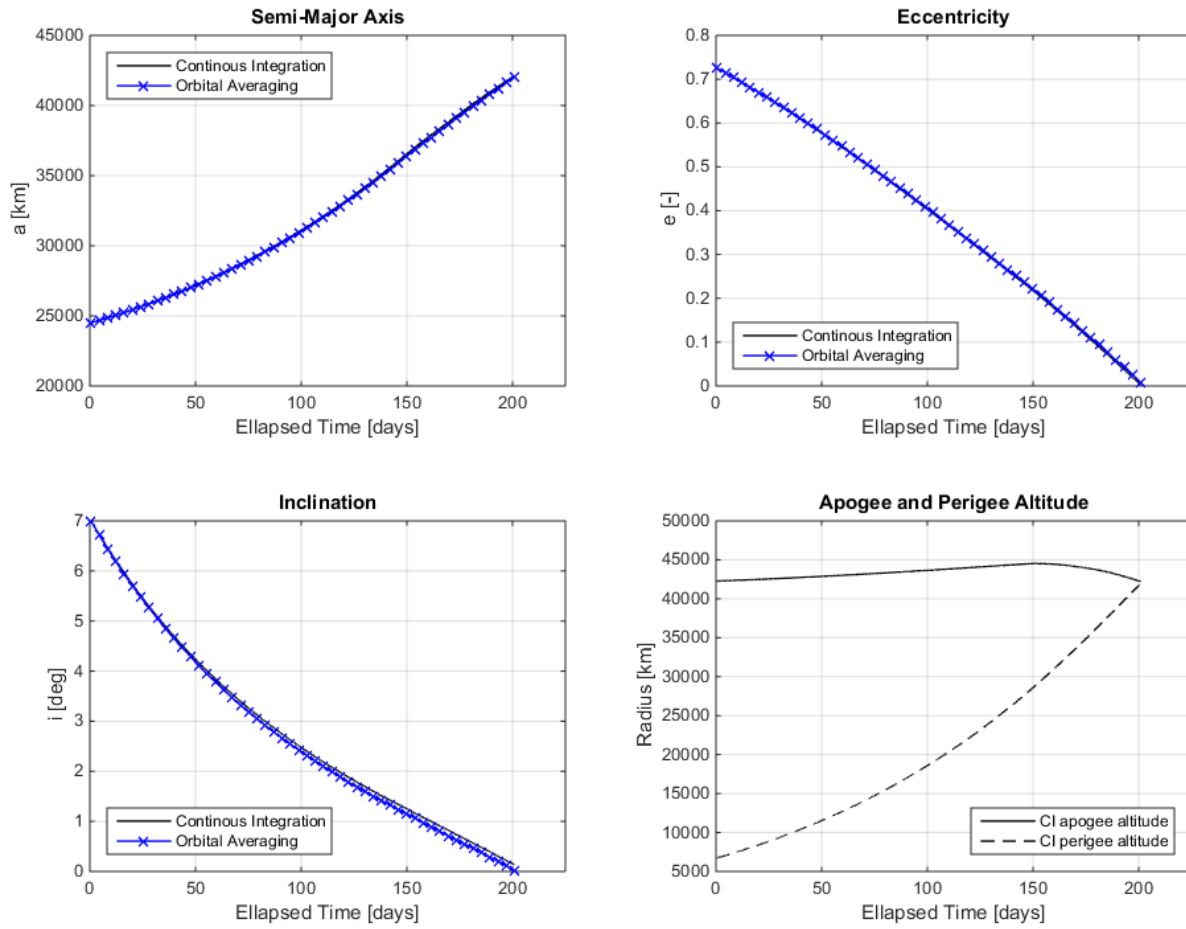

Figure D.4: Evolution of the main Keplerian elements for the 150-day minimum-propellant GTO-GEO trajectory computed with HOSTEP.

Table D.4: CI and OA results for the simulation of the optimal trajectory the 150-day minimum-propellant GTO-GEO trajectory computed with HOSTEP.

Keplerian element	CI result	OA result	OA error
Semi-major axis a [km]	42161.18	42159.36	-1.823
Eccentricity e [-]	2.54E-4	7.07E-3	0.007
Inclination i [deg]	0.129	0.005	-0.124
RAAN Ω [deg]	359.681	132.682	-226.998
Argument of perigee ω [deg]	345.010	227.899	-117.112
True anomaly θ [deg]	122.264	110.440	-11.825
Total mass m [kg]	1806.02	1805.71	-0.312

Figure D.5 shows the evolution of the Keplerian elements, propagated using CI and OA for the 200-days minimum-propellant trajectory calculated with HOSTEP for Case B. Moreover, Table D.5 shows the comparison between the CI and OA terminal propagation values.

Figure D.5: Evolution of the main Keplerian elements for the 200-day minimum-propellant GTO-GEO trajectory computed with HOSTEP.

Table D.5: CI and OA results for the simulation of the optimal trajectory the 200-day minimum-propellant GTO-GEO trajectory computed with HOSTEP.

Keplerian element	CI	OA	OA error
Semi-major axis a [km]	42064.756	42029.072	-35.684
Eccentricity e [-]	3.607E-3	7.511E-3	0.004
Inclination i [deg]	0.136	0.012	-0.124
RAAN Ω [deg]	8.511	327.564	319.052
Argument of perigee ω [deg]	305.372	9.386	-295.986
True anomaly θ [deg]	113.328	57.959	-55.368
Total mass m [kg]	1834.385	1834.106	-0.279

E

SOFTWARE ENVIRONMENT

HOSTEP has been developed in this thesis from scratch using *Fortran 90 ®* as programming language. Compared to newer programming languages, it remains highly robust and reliable, and is therefore still commonly used in the aerospace industry such as the Flight Dynamics and Operations (FDO) division of GMV. All of the results presented in this thesis have been obtained using the same computer, Intel Core i5-4590 CPU 3300 MHz and 8.00 Gb RAM, under the same conditions with respect to processor load, etc.

HOSTEP is fully integrated in ***focusleop*** ® , which is the Launch and Early Operations Phase product available in GMV's FDO software solution ***focussuite*** ®. Hence, HOSTEP's outputs can be directly input to the other tools within ***focusleop*** ® , such as PROPAG and EVENTS which were employed for validation purposes. More importantly, the low-thrust optimization tools EPTOS and IGEOR have been employed. Thorough details about these tools may be found in [Corneliu et al., 2015] and [Montealegre-Avila, 2015]. Further information about ***focussuite*** ® is available in the GMV website [GMV, 2006].

This report has been written using LaTeX, along with the packages. Unless otherwise referenced, block diagrams and flowcharts were composed through *Visio 2010 ®*, whereas plots and graphs were created using *MATLAB 2014b ®*. Figures that have not been referenced were created by the author using *Microsoft Office 2013 ®*.